Distributed nonlinear optical response

Nikola Ivanov Nikolov

Kongens Lyngby 2004
IMM-PHD-2004-

Technical University of Denmark
Informatics and Mathematical Modelling
Building 321, DK-2800 Kongens Lyngby, Denmark
Phone +45 45253351, Fax +45 45882673
reception@imm.dtu.dk
www.imm.dtu.dk

IMM-PHD: ISSN 0909-3192

Preface

This disertation is written in partial fulfillment of the requirements for the degree of *Doctor of Phylosophy*, Ph.D., from the *Technical University of Denmark*. The work has been supported financially by the Danish Research Agency through the Graduate Scool in Nonlinear Science, The Technical University of Denmark and the Risø National Laboratory.

The main part of the work presented here has been published in the four appended papers. Naturally the research in this Ph.D. project has developed in two main directions. One of the projects is on the soliton propagation and interaction in nonlocal nonlinear optical media and has been done mainly during the second and the third years. The other project, is on the supercontinuum generation in photonic crystal fibers. Chapter 2 is a brief review of the general nonlinear optics and the nonlinear optical media. Chapter 3 contains mainly results presented in papers B and C. The research on the supercontinuum generation is presented in Chapter 4 and includes the results published in papers D and E and a thorough introduction to the field. Finally Chapter 5 is meant to summarized and conclude on the work and give directions for future research in the fields.

Summary

The purpose of the research presented here is to investigate basic physical properties in nonlinear optical materials with delayed or nonlocal nonlinearity. Soliton propagation, spectral broadening and the influence of the nonlocality or delay of the nonlinearity are the main focusses in the work.

The research presented in Chapter 3 and papers B and C is concerned with the properties and the stable dark soliton propagation and their bound states in nonlocal nonlinear optical media. It is shown that nonlocality of the nonlinearity induces attractive forces between solitons, that leads to the formation of bound states of out of phase bright solitons and dark solitons. Also, the newly introduced analogy between the nonlocal cubic nonlinear and the quadratic nonlinear media, presented in paper B and Chapter 3 is discussed. In particular it supplies intuitive physical meaning of the formation of solitons in quadratic nonlinear media.

In the second part of the report (Chapter 4), the possibility to obtain light with ultrabroad spectrum due to the interplay of many nonlinear effects based on cubic nonlinearity is investigated thoroughly. The contribution of stimulated Raman scattering, a delayed nonlinear optical effect, to this process is shown to be fundamental. Further, the newly developed *nonlinear photonic crystal fibers*, is shown to be an extremely suitable tool for the process of obtaining light with an ultrabroad spectrum, the *supercontinuum generation* process. It is the high nonlinearities achievable in these fibers and the possibility to tailor the dispersion properties through precise structure control, that allow various parametric processes to take place. During the project, the process of *supercontinuum generation* has been studied "experimentally" via numerical simulations employing

a modified nonlinear Schrödinger model equation. Chapter 4 and papers D and E are dedicated to this part of the research.

Resumé

Formålet med den her præsenterede forskning er at undersøge grundlæggende fysiske egenskaber af optiske materialer med forsinket og ikke-lokal ikke-linearitet. Soliton egenskaber, spektral forbredning og indflydelsen af ikke-lokalisering og forsinkelse er hovedbrændpunkter i arbejdet.

Den forskning, der er præsenteret i Kapitel 3 og artiklerne B og C, omhandler egenskaber af mørke solitoners udbredelse og bundne tilstande i ikke-lokale ikke-lineære optiske medier. Det vises, at ikke-lokalisering af ikke-linearitetet inducerer tiltrækningskræfter mellem solitoner, som fører til dannelse af bundne tilstande af lyse og mørke solitoner, der er ude af fase. Den fornyligt indførte analogi mellem ikke-lokale kubisk ikke-lineære og kvadratisk ikke-lineære medier, som præsenteres i B og Kapitel 3, diskuteres. Specielt leverer den en intuitiv fysisk forståelse af solitondannelse i kvadratisk ikke-lineære medier.

I anden del af afhandlingen (Kapitel 4) undersøges muligheden for at opnå lys med ultrabredt spektrum, som følge af vekselvirkning af mange ikke-lineære effekter, grundigt. Bidraget fra stimuleret Raman-spredning, en ikke-lineær forsinkelseseffekt, til denne proces vises at være fundamental. Endvidere vises det, at de for nyligt udviklede *ikke-lineære fotoniske krystalfibre* udgør et ekstremt velegnet redskab for generering af lys med superbredt spektrum, dvs. for superkontinuumsgeneringsprocessen. I løbet af projektet er superkontinuumsgeneringsprocessen blevet undersøgt " eksperimentelt" ved hjælp af numeriske simuleringer under anvendelse af en modificeret ikke-lineær Schrödinger modelligning. Kapitel 4 og artiklerne D og E er helliget denne del af forskningen.

Acknowledgements

I want to thank my supervisors, Res. Associate Prof. Ole Bang (IMM/COM), Senior Research Specialist Jens Juul Rasmussen (Risø), Prof. Dr.Techn Peter Leth Christiansen (IMM), and Prof. Dr.Techn Anders Bjarklev (COM) for their professional advises and help in the scientific research, work organization, and nontrivial administrative problems. I also want to thank Prof. Wieslaw Krolikowski (ANU) for his valuable advises and encouragements.

List of appended papers

[B] Nikola I. Nikolov, Dragomir Neshev, Ole Bang, and Wieslaw Królikowski, Quadratic solitons as nonlocal solitons, Physical Review E, Volume 68, 036614 (September 2003).

[C] Nikola I. Nikolov, Dragomir Neshev, Wieslaw Królikowski, Ole Bang, Jens Juul Rasmussen, and Peter Leth Christiansen, Attraction of nonlocal dark optical solitons, Optics Letters, Volume 29, 286-288 (2004).

[D] Nikola I. Nikolov, Thorkild Sørensen, Ole Bang, Anders Bjarklev, and Jens Juul Rasmussen, Modelling of PCF Nonlinearities, in "Photonic Crystal Fibers: Science and Applications" to be published in the series "Optical and Fiber Communications Reports", Ed. Anders Bjarklev (Springer-Verlag New York).

[E] Nikola I. Nikolov, Thorkild Sørensen, Ole Bang, and Anders Bjarklev, Improving efficiency of supercontinuum generation in photonic crystal fibers, Journal of the Optical Society of America B, Volume 20, 2329 (2003).

List of all publications

Journal papers:

- Nikola I. Nikolov, Thorkild Sørensen, Ole Bang, and Anders Bjarklev, Improving efficiency of supercontinuum generation in photonic crystal fibers, Journal of the Optical Society of America B Volume 20, Issue 11, 2329-2337 (2003).
- Nikola I. Nikolov, Dragomir Neshev, Ole Bang, and Wieslaw Królikowski, Quadratic solitons as nonlocal solitons, Physical Review E, Volume **68**, 036614 (September 2003) (5 pages).
- Nikola I. Nikolov, Dragomir Neshev, Wieslaw Królikowski, Ole Bang, Jens Juul Rasmussen, and Peter Leth Christiansen, Attraction of dark nonlocal solitons, Optics Letters Volume **29**, No. 3, pp. 286-288 (Feb. 1, 2004).
- Nikola I. Nikolov, Thorkild Sørensen, Ole Bang, Anders Bjarklev, and Jens Juul Rasmussen, Modelling of PCF Nonlinearities, in "Photonic Crystal Fibers: Science and Applications" to be published in the series "Optical and Fiber Communications Reports, Ed. Anders Bjarklev (Springer-Verlag New York) (accepted).
- W. Z. Królikowski, O. Bang, N. I. Nikolov, D. Neshev, J. J. Rasmussen, and D. Edmundson, "Modulational instability, solitons and beam propagation in nonlocal nonlinear media" Journal of Optics B, Quantum Semiclass. Opt. **6** S288-S294 (2004).

Conferrence proceedings:

- Nonlinear Guided Waves and Their Applications Topical Meeting March 28-31, 2004, Westin Harbour Castle, Toronto, Canada. Nikola I. Nikolov, Dragomir Neshev, Ole Bang, Wieslaw Krolikowski, and John Wyller, "A nonlocal description of two-color parametric solitons" (poster presentation TuC4).

- Nonlinear Guided Waves and Their Applications Topical Meeting March 28-31, 2004, Westin Harbour Castle, Toronto, Canada. Thorkild Sørensen, Nikola I. Nikolov, Ole Bang, Anders Bjarklev, Kristian G. Hougaard, Kim P. Hansen, and Jens J. Rasmussen, "Cob-web microstructured fibers optimized for supercontinuum generation with picosecond pulses" (oral presentation WC4).

- CLEO/IQEC Conference on Lasers and Electro Optics / International Quantum Electronics Conference, May 16-21, 2004, Moscone Center West, San Francisco, California, USA. W. Krolikowski, N.I. Nikolov, O. Bang, D. Neshev, J. Wyller, J.J. Rasmussen, and D. Edmundson, "Optical beams and spatial solitons in nonlocal nonlinear media" (oral presentation ITuH).

- ACOLS 03 Australasian Conference on Optics, Lasers, and Spectroscopy 2003 December 1-4, 2003, University of Melbourne, Melbourne, Victoria, Australia. W. Krolikowski, O. Bang, N. Nikolov, D. Neshev, J.J. Rasmussen, P.L. Christiansen, J. Wyller and D. Edmundson, "Nonlocal solitons" (poster 80, page 295 in book of abstracts).

- ICOLS 03 16th International Conference on Laser Spectroscopy July 13-18, 2003, Novotel Palm Cove Resort, Palm Cove, Queensland, Australia. Nikola I. Nikolov, Dragomir Neshev, Ole Bang, and Wieslaw Krolikowski, "Quadratic solitons described as nonlocal solitons" (poster, Monday no. 71, page 127 in book of abstracts).

- CLEO/EQEC Europe 2003 June 23-27, 2003, International Conference Centre Munich, Munich, Germany. Wieslaw Krolikowski, Ole Bang, Dragomir Neshev, and Nikola I. Nikolov, "Quadratic solitons as nonlocal solitons" (contributed talk EE2-5-WED).

- 2003 Optical Fiber Communication Conference March 23-28, 2003, Atlanta, Georgia, USA. Nikola I. Nikolov, Ole Bang, and Anders Bjarklev, "Designing the dispersion for optimum supercontinuum bandwidth using picosecond pulses" (poster MF 16, pp. 17-18).

Contents

Chapter 1

Introduction

Nonlinear optics is a very active and attractive field of investigations. In its ultimate form it allows unlimited transformation and control of light by light.

The main application of nonlinear optics is the creation of all-optical circuits. Many optical materials exibiting different types of optical responses have been considered in this context. The possibility of soliton formation and propagation in various nonlinear optical media is an attractive way of creating light induced waveguides by laser beams with high intensity. The induced waveguides can in turn guide weak intensity beams and pulses with different carrier frequencies. Dynamically formed bound states of solitons can be used as junctions of two or more waveguides. Here it is demonstrated, that nonlocality of the nonlinearity is crucial for the formation of bound states of dark and out of phase bright solitons. It is shown that, the otherwise repelling optical objects as dark solitons and out of phase bright solitons in Kerr-like nonlinear media, can form bound states if the nonlocality of the material with cubic nonlinearity is strong enough, see paper B and [91]. Further, it is shown that these solitons and their bound states are stable in propagation, see C and [93].

The possibility to generate new optical frequencies is another attractive application of nonlinear optics. Many investigations have been carried out to obtain independently harmonics and parametrically mixed frequencies [1, 2]. A fastly developing new trend in nonlinear optics is supercontinuum generation [113].

This is a nonlinear optical process, that leads to spectral broadening, due to the simultaneous contribution of many predominently cubic nonlinear effects. Further, photonic crystal fibers (PCFs), a fastly developing field of fiber optics, reveal novel features of waveguiding technology, that allow the achievement of very high nonlinearities combined with proper dispersion control. This, makes PCFs the most suitable tools for generating a supercontinuum spectrum (SC) of light. PCFs are also promissing tools for further improvements of this process.

Chapter 2

Nonlinear optics and nonlinear optical materials

Since the invention of the laser in 1960, nonlinear optics has become a rapidly progressing branch of optical science. The nonlinear optical effect refers to any optical phenomena, modelled by a nonlinear equations, i.e. equations containing terms proportional to higher than the first order power of the optical field or its derivatives [1, 2]. Though, nonlinear optical effects are in principle acsessible in every optical material, these optical materials or media, whose properties are suitable for observation and investigation of the nonlinear optical phenomena are called nonlinear materials. Such a deffinition for a nonlinear optical material is quite broad, since provided the applied input optical intensity is high enough, any optical material can exhibit nonlinear properties. In the context of supercontinuum generation, in (Chapter 4) another way to access high optical nonlinearities, will be shown to be possible, by use of specially designed optical structures that allow more efficient interaction of light with matter.

The nonlinear dependence of the optical response on the light intensity is either caused by atomic-molecular polarization, or mediated by an additional physical process. When the nonlinear medium is centro-symmetric, the induced nonlinear polarization is of a third order. Third order nonlinear effects are the four-wave-mixing (FWM) and the self-phase modulation (SPM). If the induced nonlinear refractive index is proportional to the intensity of the optical wave,

this effect is called self-phase modulation or nonlinear Kerr effect. The intrinsic nonlinearity of many optical nonlinear media is of third order. However, nonlinear optical response is possible not only due to atomic-molecular polarization. Intensity induced nonlinear change of the refractive index can be mediated by other macroscopic effects as reorientation of molecules or heating and diffusion. The time scale of the atomic-molecular polarization is fast (of the order of attoseconds) compared to the time period of a light wave. When the nonlinearity is due to any other atom-macroscopic effects as reorientation of molecules or heating and diffusion, the characteristic time for acquiring a nonlinear index change is usually longer. Thus, the time delay of the nonlinearity generally can not be neglected when modelling light propagation in such materials with a power dependent nonlinear optical response.

Propagation of light in optical media with a third order nonlinearity, is governed by the nonlinear Schröedinger equation (NSE):

$$2ik\frac{\partial E}{\partial z} + \frac{\partial^2 E}{\partial x^2} + \frac{\partial^2 E}{\partial y^2} + s\frac{n_2}{\eta_0}k^2 E|E|^2 = 0, \tag{2.1}$$

where, $E(x, y; z)$ is the complex field amplitude, $\eta_0 = \sqrt{\mu_0/\varepsilon_0}$, k the wave vector, x, y transverse coordinates, and z the longitudinal propagation coordinate. Here, s=$\pm$1 for focusing and de-focusing media respectively. The one dimensional NSE can be obtained from 2.1 by simply omiting one of the transverse coordinates, i.e. assuming that $\frac{\partial^2 E}{\partial y^2} = 0$. This approximation is valid for beam propagation in slab waveguides and when a circular symmetry is assumed, since the two transverse x and y coordinates in this case can be modeled by one variable.

The NSE is a generic model describing the evolution of a slowly varying envelope of a wave train in conservative, dispersive systems. NSE describes nonlinear waves in plasma physics [3, 6] and gravity waves on deep water [7]. Further the NSE is used also in the description of a system of coupled anharmonic oscilators in the continuum limit [8]. Additionally, Bose-Einstein condensates of an ultracold dillute gases are described by a modified NSE with perriodic potential. This modified version of the NSE is called the Gross-Pitaevskii equation [9].

In this chapter, nonlinear optical materials with atom-macroscopic third-order nonlocal nonlinearities and their models, will be considered.

2.1 Nonlocal and time delayed nonlinear optical effects

Generally the response of any physical system to an external field or force is nonlocal. This means that the applied force on one object of the system (or point of the media), spreads its influence to the other objects (points) too. Nonlocality is a consequence of the variety of forces and fields by which the particles or objects composing a physical system, are interacting among themselves.

In nonlinear optics, a nonlocal distribution of the intensity induced refractive index is caused by additional physical mechanisms such as transport processes or inter-particle interaction. Transport processes can be either heat conduction [16] or diffusion of charges in photorefractive materials [18, 19] or atoms in vapours [23]. The nonlocal response of an external field can be due to a variety of physical mechanisms. Here, only third-order, intensity dependent nonlinear nonlocal effects are considered. Linear nonlocal effects as nonlocal dispersion [24] and others are out the scope of this work.

The propagation of light waves in a medium with a nonuniform distribution of the refractive index change is governed by the wave equation:

$$i\left[\frac{\partial}{\partial t}+v_g\frac{\partial}{\partial z}\right]E+\frac{\partial^2 E}{\partial t^2}+\nabla_\perp^2 E+\frac{2k^2}{n_0}\Delta n(x,y,z;t)E=-ik\alpha E \qquad (2.2)$$

Here E is the envelope of the light wave, k the wave number, z, the propagation coordinate, n_0 is the linear refractive index, Δn the change in the refractive index and v_g is the group velocity. When considering propagation of continous wave light beams, the second order time derivative describing the dispersion is omited. In a reference frame moving with the group velocity, [16, 17], Eq. 2.2 transforms to the general beam-propagation equation. When the change of the refractive index Δn is proportional to the light intensity $|E|^2$, Eq. 2.2 becomes the NSE 2.1. There are many physical systems in which the induced refractive index change is nonlinear. Here some examples of nonlinear systems in which the nonlocality of the nonlinear refractive index can not be neglected, are given. These are the heat conduction and diffusion in absorptive liquids, ponderomotive force in plasmas, reorientation of molecules in liquid crystals, diffusion of electrons in photorefractive crystals, and inter-particle interaction in BECs.

While propagating through an absorptive liquid media, a laser beam induces temperature and density gradients that change the refractive index profile. In this case, heat conduction and diffusion are the major processes that lead to nonlocality of the light-induced refractive index. The refractive index change is,

in general, a function of temperature and density changes inside the material [16]:

$$\Delta n(x,y,z;t) = \left(\frac{\partial n}{\partial \rho}\right)_T \Delta\rho(x,y,z;t) + \left(\frac{\partial n}{\partial T}\right)_\rho \Delta T(x,y,z;t), \tag{2.3}$$

For times much longer than the acoustic transit time, the change of the density $\Delta\rho$, becomes directly proportional to the change of the temperature, $\Delta\rho = (\partial\rho/\partial T)_p \Delta T$, where $\partial\rho/\partial T$ is a constant. For a laser heat source in liquids, the electrostriction can be neglected and the temperature change $\Delta T = T - T_0$ is determined by:

$$c_p\rho\frac{\partial T(x,y,z;t)}{\partial t} - k\nabla^2 T(x,y,z;t) = \alpha I(x,y,z;t) \tag{2.4}$$

In this way, the refractive index depends on the intensity of the light beam, thus the process is nonlinear. The nonlocality of the nonlinearity arises from the thermal diffusion, described by the spatial derivatives in Eq.2.4.

The ponderomotive force in plasma causes drift of electrons and ions from regions with higher intensity to regions with lower intensity of the propagating electromagnetic wave. Thus the induced spatial distribution of the plasma density leads to nonlinear response to the optical wave. Additional processes, such as heating or diffusion, lead to a nonlocal nonlinearity as well. For the case of nonlinear Landau damping in unmagnetized [5] as well as magnetized plasmas[6], the form of the nonlocal term is quite different, but still preserving the main features of the nonlocal nonlinearity.

The physical mechanism leading to nonlinear nonlocal response in liquid crystals is reorientation of molecules [25, 27]. As the angle of rotation of the nematic molecules is finite the nonlinearity is saturable. Due to the mutual molecular interaction, the induced nonlinear refractive index by the optical field is nonlocal. Here the nonlocality of the nonlinear refractive index can not be expressed simply as a convolution integral of the optical intensity and the distributed response function. The model for the nonlocal nonlinearity in liquid crystals includes an additional differential equation for the molecular angle of rotation according to the constant external electric filed. Thus, by use of the variational approach and the slowly varying envelope approximation the propagation of the optical beam in liquid crystals is described by a Schro´odinger-type nonlinear equation, Eq. 2.5, and the nonlocal nonlinearity is described by a seperate differential equation describing the nonuniform director distribution, Eq. 2.6 [26].

$$2ik\frac{\partial E}{\partial z} + \nabla_\perp^2 E + \frac{\omega^2}{c^2} e_a \left[sin^2\theta - sin^2\theta_0\right] E = 0 \tag{2.5}$$

$$4K\nabla_\perp^2\theta + e_a sin(2\theta)|E|^2 = 0 \tag{2.6}$$

Here, E is the slowly varying envelope of the propagation beam, θ_0 is the initial tilt of the molecules, $e_a = n_{\|}^2 - n_{\perp}^2$ is the optical anisotropy, K elastic constant. As reported in [27], it is mainly the spatial nonlocality that contributes to the observation of stable spatial solitons in liquid crystals.

The nonlinear optical response of photorefractive crystals is saturable in time, but nonlocal and anisotropic in space [18, 19, 20, 21, 22]. The model for optical beam propagation in a photorefractive material is described by two coupled equations for the envelope of the optical field and the electrostatic potential φ [19]. When the spatial scale of the optical field $E(\vec{r})$ is larger than the photorefractive Debye length and the diffusion field may be neglected, the steady state propagation of this beam along the z axes is described by the coupled equations[19, 20]:

$$\begin{aligned} \left[\frac{\partial}{\partial z} - \frac{i}{2}\nabla^2\right] E(\vec{r}) &= i\frac{\partial \varphi}{\partial x} E(\vec{r}) \\ \nabla^2\varphi + ln\left(1+|E|^2\right)\cdot\nabla\varphi &= \frac{\partial}{\partial x} ln\left(1+|E|^2\right). \end{aligned} \tag{2.7}$$

Here, $\nabla = \hat{x}(\partial/\partial x) + \hat{y}(\partial/\partial y)$, and the dimensionless coordinates (x, y, z) are connected to the physical (x', y', z') coordinates by the expressions $z = \alpha z'$ and $(x, y) = \sqrt{k\alpha}(x', y')$, where α is proportional to the external field directed along the x-axis far from the beam and the square of the refractive index of the medium.

BECs, inherently have a spatially nonlocal nonlinear response due to the finite range of the inter-particle interaction potential. The model describing nonlinear interaction of ultra cold atoms in BEC is the Gross-Pitaevskii equation [9]:

$$i\hbar\frac{\partial \Psi}{\partial t} = -\frac{\hbar^2}{2m}\frac{1}{2}\nabla^2\Psi + V(\mathbf{r})\Psi + U\Psi\int K(\mathbf{r}-\mathbf{r}')\Psi(\mathbf{r}')|^2 d(\mathbf{r}') \tag{2.8}$$

This is exactly the nonlocal NSE, but with the additional term for the external potential $V(x)$ [9]. Here $\Psi(\mathbf{r}, t)$ is the wave function of N particles. Though, the physics of the processes in BEC is different than the nonlocal nonlinearity in nonlinear optics and plasma physics, the same model used for their description, results in the same conclusions, i.e. collapse arrest [11] and soliton stabilization [12] in the presence of nonlocality.

Naturaly any process in material or system caused by an external force or field needs a transition time to develop. The delay of the responce of the physical media, can be considered as an analog to the nonlocal distribution of the external induced changes of the materials properties. This means that, the concept of

nonlocal nonlinearity can be expanded to the time domain, i.e. into a noninstantaneous or delayed nonlinear response. In nonlinear optics, the Raman effect is such noninstantaneous nonlinear response. The time delayed and the spatial nonlocal nonlinear effects are similar in the sense that they are modelled by similar equations. For example, if orthogonal component of the Raman response is neglected, the equation describing the delayed nonlinear Raman response is noninstantaneous or "nonlocal in time":

$$\begin{aligned} \frac{\partial A}{\partial z} &= -\mu A - \frac{i}{2}\frac{\beta_2}{2}\frac{\partial^2 A}{\partial \tau^2} \\ &+ i\gamma A\left[(1-f_R)|A|^2 + f_R\int h_R(\tau - s)|A(s)|^2 ds\right]. \end{aligned} \tag{2.9}$$

Here $A = A(t,z)$ is the envelope of the complex linearly polarized optical field. The time $\tau = t - z/\overline{v}$ is in a reference frame moving with the average group velocity, z is the propagation coordinate, μ is the loss, γ is the effective nonlinearity, and f_R is the fractional contribution of the Raman effect. To preserve the casuality in time the response function representing the delayed nonlinearity is $h_R = 0$ for $t = /left(-\infty$,0/right]. Also it should be noted that the Raman response function h_R is not sign definite. Thus the physical processes observed due to Raman delayed nonlinearity and the symmetric spatial nonlocal response, are different.

Another example of delayed or noninstantaneous nonlinear optical response is the plasma formation by intense ultrashort light pulses in gases [13, 14]. This phenomenon occurs due to the self-focusing of intense light pulses in gases, which allows the beam intensity to be increased enough to generate plasma. The regions where plasma is generated, have lower refractive index, thus further increase of the optical amplitude is prevented due to defocussing. The process of beam contraction and expansion that may repeat many times during pulse propagation in air is called "dynamic spatial replenishment in air" [15]. This process allows, self-guiding of short high-power light pulses in air.

2.2 Photonic crystals and photonic crystal fibers as nonlinear optical media

Photonic crystals are optical media, in which the refractive index is periodically modulated with a period of the order of an optical wavelength [28, 29]. Thus, in such media the propagation of light can be prohibited for certain wave frequencies and under specific angles. The periodic modulation of the refractive

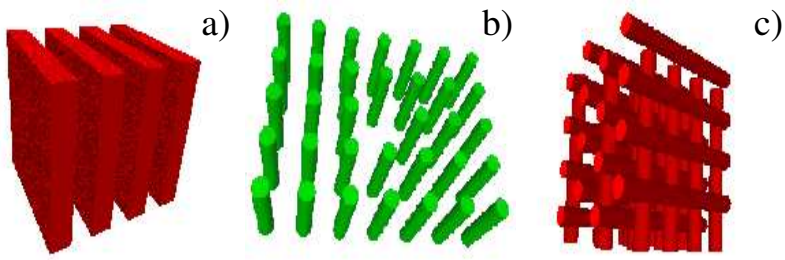

Figure 2.1: Examples of a) 1-D, b) 2-D and c) 3-D photonic crystal. Images are borrowed from: http://www.elec.gla.ac.uk/groups/opto/photoniccrystal/

index in the photonic crystal, can be in 1D, 2D or 3D dimensions, Fig. 2.1. It has been shown, that defects in the periodical refractive index modulation, may lead to formation of localized or guiding modes. The concept for guiding light in a photonic crystal, relies on the existence of band-gaps for a range of light frequencies. Light with frequency within the band-gap cannot propagate in any direction in a photonic crystal with no defect in the periodic structure [28, 29]. Any violation of the perfect periodic structure, will allow the existence of a defect induced light mode around it. The defect itself resembles an electromagnetic resonator. Thus, the frequency of this defect mode will be confined on the size of the defect. In a 2D photonic crystal, a line defect yielding a guiding mode in the first band-gap, is simply made by removing a row of the holes of the 2D periodic structure. In this case the waveguide is in the plane of symmetry. It is apparent, that there is no band-gaps for waves propagating along the z axes, that is perpendicular to the plane of symmetry. Thus, if a single rod in the

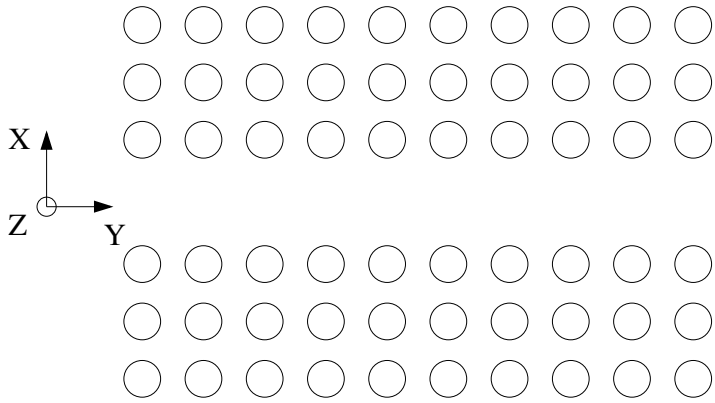

Figure 2.2: Plane of symetry section of a 2-D photonic crystal of dielectric rods, shown in Fig. 2.1 b). The z axis is along the rods length.

structure in Fig. 2.1 (b) is removed, localized transverse modes in the band-gap regions for the $x-y$ plane, will be allowed to propagate along the z axes, without penetrating into the rest of the material. Guiding light along the z axes of a planar photonic crystal in the $x-y$ plane is the concept of the creation of the so-called band-gap guiding photonic crystal fibers (PCFs)[32, 33]. The invention of photonic crystal fibers [30, 31, 32, 33, 34, 35], revolutionized the optical fiber technology. PCFs are optical fibers with wavelength-scale transverse structure of air and silica regions. Many different PCF structures have been considered both theoretically and experimentally. The transverse structure determines the mechanism of guidance and therefore the dispersion and nonlinear properties of the PCF. According to the mechanism of guiding of light, PCFs are divided in two main classes. The band-gap PCFs, guide light only over a limited range of wavelengths that correspond to the band-gap of the cladding material. The effective-index PCFs, guide light due to the total internal reflection. Though the effective-index PCFs resemble the basic features of the standard optical fibers, many novel fenomena and applications of these fibers are shown to be possible by a proper structure design. Already a single-mode operation for all the wavelengths of interest [30, 31] is reported to be possible in effective-index PCFs. The highly nonlinear PCFs are effectively index-guiding fibers, with a significantly reduced core size (having a core diameter around $\approx 1\mu m$) and higher numerical aperture. The reduced effective area leads to increased light intensity of the single mode. Thus, the effective nonlinear coefficient in the effective-index guiding PCFs is usually of several degrees higher than in a bulk material. In this way, a significant increase in the nonlinearity is possible without the addition of doping elements. Further, the longer interaction leghts additionaly increase the effective nonlinearity. Finaly, the highly nonlinear PCFs are an unique nonlinear medium for enhanced nonlinear processes, not accessible by the standard optical fibers or bulk nonlinear materials.

Chapter 3

Nonlinear nonlocal optics

As discussed in the begining of Chapter 3, nonlocality is a general feature of many nonlinear optical effects. In this sense any nonlinear optical medium or material can be regarded to some extent and as a nonlocal, but with different degree of nonlocality depending on the material's specific properties. However, the term "nonlinear nonlocal optical material (medium)" will be used in this thesis for such nonlinear optical materials, for which in the description of the nonlinear processes in them, the nonlocality can not be neglected for a wide range of light beam/pulse parameters at which nonlinearities are physically accessible.

In the previous chapter it was shown, that the nonlocal NLSE, is a generic model describing nonlocal nonlinearities in many different physical systems. In this chapter, the role of nonlocality in phenomena associated with propagation of optical beams in nonlinear media is discussed. These include modulational instability of plane waves, structural stability of localized beams and interaction of solitons. It is shown that the basic features, such as dark soliton stabilization and formation of dark soliton bound states, do not depend on the specific shape of the response function of the nonlocal nonlinear material. Here, background and additional results to that presented in the attached papers B and C will be given. In paper B, the analogy between the nonlocal cubic nonlinearity and the quadratic nonlinearity is concidered, and in paper C stable propagation and attraction of dark solitons in nonlocal nonlinear media is presented.

3.1 General features of the nonlocal NSE

In this section I will concider the general features, such as modulational instability (MI) and beam collapse for the nonlocal NSE. The formation and stable propgation of dark solitons and bound states of dark nonlocal solitons will be considered in the next section.

As was discussed in the previous chapter, the standard spatial NSE describes a stationary optical beam propagating along the z-axis with the scalar amplitude of the electric field $E(\vec{r},z)=\psi(\vec{r},z)\exp(iKz-i\Omega t)+c.c.$ and $\vec{r}=(x,y)$ a vector in the 2-dimensional transverse coordinate space:

$$i\partial_z\psi+\frac{1}{2}\left(\partial_x^2+\partial_y^2\right)\psi+\Delta n(I)\psi=0, \tag{3.1}$$

Here, K is the wavenumber, Ω is the optical frequency, and $\psi(\vec{r},z)$ is the slowly varying amplitude. In this case the time dependance of the optical field and the nonlinearity are neglected.

When the nonlinear optical response of the medium is nonlocal, the refractive index change $\Delta n(I)$, induced by a beam with intensity $I(\vec{r},z)=|\psi(\vec{r},z)|^2$ can be described by the following phenomenological nonlocal model:

$$\Delta n(I)=\Delta n(\vec{r},z)=s\int R(\vec{r}'-\vec{r})I(\vec{r}',z)d\vec{r}', \tag{3.2}$$

where the integral $\int d\vec{r}$ is over all transverse dimensions and $s=\pm1$ corresponds to a focusing or de-focusing medium respectively. The real, localized, and symmetric function $R(r=|\vec{r}|)$ is the response function of the nonlocal medium, that is normalized as follows:

$$\int R(\vec{r})d\vec{r}=1 \tag{3.3}$$

As generally in the spatial NSE, transient effects are neglected, the nonlocality is also assumed to be stationary. Further, the shape and the width of the response function are assumed to be the same along the propagation direction.

Usually the degree of nonlocality is defined by the ratio of the beam width and the width of the nonlocal response function. In this sense, the phenomenological nonlocal nonlinearity model (3.2) is more general and can be used to describe the local nonlinear and the highly nonlocal nonlinear case that corresponds to a linear waveguide problem [44]. This is evident, by simply considering the extreme limits of the width of the response function $R(r)$ relatively to the beam width. An illustration of the different degrees of nonlocalities is given in Fig. 3.1.

The local nonlinear case is accessible by letting the width of the normalized function $R(r)$ approach zero, which transforms it to a delta response function $R(r) = \delta(|\vec{r}|)$. In this case the refractive index change becomes a local function of the light intensity, $\Delta n(I) = sI(\vec{r}, z)$, i.e., the refractive index change at a given point is solely determined by the light intensity at that very point, and Eq.(3.1) simplifies to the ordinary NSE. The case of a local nonlinearity has been the subject of many investigations and analytical treatment was shown to be possible [68, 70]. Thus, the properties of the ordinary NSE will not be considered here. There are two other important physical situations when the

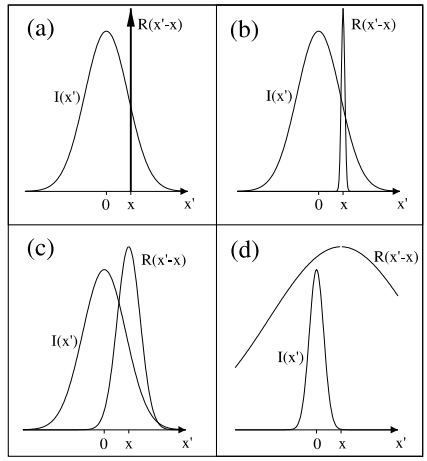

Figure 3.1: Different degrees of nonlocality, as given by the width of the response function R(x) and the intensity profile I(x). (a) is the local, (b) the weakly nonlocal, (c) a general nonlocal and (d) a strongly nonlocal response.

convolution term in equation Eq.(3.1) can be represented in a simplified form allowing for an extensive analytical treatment of the resulting equation. These are the weak nonlocality limit and the strong nonlocality limit. When the width of the response function is much less than the spatial extent of the beam, $I(\vec{r})$ can be formally expanded in a Taylor series and only the first significant terms be retained. This gives the nonlinearity in the following form:

$$\Delta n(I) = s\left(I + \gamma \nabla_{\perp}^2 I\right), \quad \gamma = \frac{1}{2}\int r^2 R(r) d\vec{r}, \tag{3.4}$$

where the positive definite γ is a measure of the strength of the nonlocality.

Here the nonlocal contribution to the Kerr-type local nonlinearity is reflected by the presence of the Laplacian of the wave intensity. It turns out that the nonlinearity in this particular form appears naturally in the theory of nonlinear

effects in plasma [43]. It has been shown recently that the one-dimensional version of Eq.(3.1) with nonlinearity Eq.(3.4) supports propagation of stable bright and dark solitons [52].

Another limiting case, the so called highly nonlocal limit, refers to the situation when the nonlocal response function is much wider than the beam itself. It can be shown that in this limit the nonlinear term may be approximated by

$$\Delta n(I) = sR(\mathbf{r})P, \tag{3.5}$$

where $P = \int_{\infty}^{\infty} I(\mathbf{r}')d\mathbf{r}'$ is the total power of the beam, that is a conserved quantity. Interestingly enough, in this case the propagation equation becomes linear. It describes the evolution of an optical beam trapped in an effective waveguide structure with the profile represented by the nonlocal response function. This highly nonlocal limit has been first explored by Snyder and Mitchell in the context of the so called "accessible solitons" [44]. The same authors also illustrated the influence of nonlocality on the dynamics of beams for the special logarithmic nonlinearity, which allows exact analytical treatment [45].

Even though it is quite apparent in some physical situations that the nonlinear response in general is nonlocal (as in the case of thermal lensing), the nonlocal contribution to the refractive index change was often neglected [54, 55]. This is justified if the spatial scale of the beam is large compared to the characteristic response length of the medium (given by the width of the response function). However, for very narrow beams or beams with fine spatial features (such as dark solitons) the nonlocality can be of crucial importance. Intuitively, the

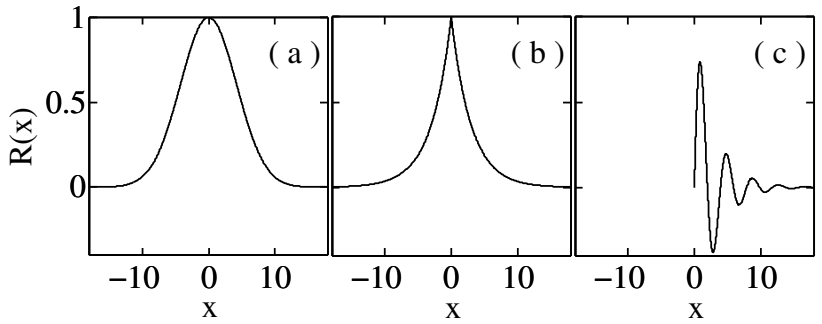

Figure 3.2: Different nonlocal response functions. (a) gaussian $\exp(-x^2/36.0)$, (b) exponential $\exp(-|x|/3.0)$ and (c) an assymetric decaying sinusoid $\sin(x * 5.0/\pi) * \exp(-x/3.0)$.

basic properties of the nonlocal nonlinear medium will be strongly dependent not only on the width of the response function, but also on the shape. In Fig.

3.2, three different response functions are shown, that describe real physical phenomena. Fig.3.2 (b), provides a very important connection between the nonlocal cubic nonlinearity and the χ^2 nonlinearity [91]. The important case of exponential nonlocality will be thoroughly discussed later in the context of possibility to form bound statets of dark solitons in nonlocal media with cubic nonlinearity. The last response function shown in Fig.3.2 (c) is an important case too. This nonlocal nonlinear response function describes the delayed Raman effect in nonlinear optics, provided the x coordinate is considered as time [2].

3.1.1 Modulational instability and beam collapse

Modulational instability (MI) and beam collapse are basic properties of the NSE [68, 69]. Thus, numerous studies of these properties for the nonlocal NSE have been done [65, 66, 94]. Here a general review of the main results with some theoretical background will be presented.

Modulational instability constitutes one of the most fundamental effects associated with wave propagation in nonlinear media. It signifies the exponential growth of a weak perturbation of the amplitude of the wave as it propagates. The gain leads to amplification of sidebands, which break up the otherwise uniform wave front and generate fine localized structures (filamentation). Thus, it may act as a precursor for the formation of bright spatial solitons. Conversely the generation of dark spatial solitons requires the absence of MI of the constant intensity background.

The phenomenon of MI has been identified and studied in various physical systems, such as fluids [57], plasma [58], nonlinear optics [59, 60], and discrete nonlinear systems [61]. It has been shown that MI is strongly affected by various mechanisms present in nonlinear systems, such as higher order dispersive terms in the case of optical pulses [62], saturation of the nonlinearity [63], and coherence properties of optical beams [64]. Here the influence of the nonlocality on the MI will briefly described. Lets consider the model (3.1) that permits plane wave solutions of the form:

$$\psi(\vec{r}, z) = \sqrt{\rho_0}\exp(i\vec{k_0}\cdot\vec{r} - i\beta z), \quad \rho_0 > 0, \tag{3.6}$$

where ρ_0, $\vec{k_0}$, and β are linked through the nonlinear dispersion relation

$$\beta = k_0^2 - s\rho_0. \tag{3.7}$$

Since, the nonlinearity of the model (3.1) is power dependent, $\Delta n(I) = s\int R(\vec{r}' - \vec{r})I(\vec{r}', z)d\vec{r}'$, the nonlinear dispersion relation (3.7) does not depend on the specific form and width of the nonlocal response function $R(\vec{r})$.

However, perturbations to the plane wave solution, are strongly influenced by the nonlocality of the nonlinearity. This can be shown by comsidering the perturbation to the plane wave solution in the following form

$$\psi(\mathbf{r},z) = [\sqrt{\rho_0} + a_1(\vec{r},z) + cc] \exp(i(\vec{k_0}\cdot\vec{r} - \beta z)), \qquad (3.8)$$
$$a_1(\vec{r},z) = \int \widetilde{a}_1(\vec{k}) exp(i\vec{k}\cdot\vec{r} + \lambda z) d\vec{k}$$

where $a_1(\vec{r},z)$ is the complex amplitude of the small perturbation and λ is the so called growth rate. When λ is positive, the perturbation grows during propagation indicating instability. The spectral ranges where λ is positive can be found by substituting Eq.(3.8) in the propagation equation and after linearizing around the plane wave solution the growth rate can be found as an eigenvalue of the resulting system of equations for the spectrum of the perturbation [65, 66].

$$\lambda^2 = -k^2\rho_0 \left[\alpha k^2 - s\widehat{R}(\vec{k})\right], \qquad (3.9)$$

where $k = |\vec{k}|$ denotes spatial frequency, $\alpha = 1/(4\rho_0)$, and $\widehat{R}(k)$ is the Fourier spectrum of $R(r)$.

The general eigenvalue equation (3.9) constitutes the main result of the analysis. First of all it can be noticed that $\widehat{R}(0) = 1$, since the response function is assumed to be normalized to unity $\int_{-\infty}^{\infty}\int_{-\infty}^{\infty} R(\vec{r})d\vec{r} = 1$.

Further, the well-known modulational instability (stability) result for the standard local NSE equation can easily be recovered from the general eigenvalue equation (3.9) by setting $R(\mathbf{r})$=$\delta(\mathbf{r})$, where $\delta(x)$ is the Dirac delta function, and the result is:

$$\lambda^2 = -k^2\rho_0(\alpha k^2 - s) \qquad (3.10)$$

where $s = +1$ ($s = -1$) yields instability (stability). As formula Eq.(3.9) shows the stability properties of the plane wave solutions are completely determined by the properties of spectrum of the nonlocal response function. The MI gain spectrum for the nonlocal NSE is:

$$gain_{MI} = Re(\lambda) = \sqrt{-k^2\rho_0 \left[\alpha k^2 - s\widehat{R}(\vec{k})\right]} \qquad (3.11)$$

Detailed analysis of all the possible scenarios is discussed in [66], but here they will be summarized.

The Fourier spectrum of typical response functions such as Gaussian, Lorentzian, and exponential is always positive definite. Therefore, for defocusing

nonlinearity (s=−1) plane wave solution remains always stable. For the focusing medium (s=+1), there always exist a certain wavenumber band symmetrically centered about the origin, where $\lambda^2 > 0$ for sufficiently small k. It means that the system will always exhibit a long wave MI in the focusing case, independently of the details in the behavior of the response function. However, the nonlocality tends to suppress the instability by decreasing the growth rate and the width of the instability band. This can be explained very well analytically considering Eq. 3.11, for the local and nonlocal cases. When the width of the nonlocal response function $\sigma = 0$, $\hat{R}(\vec{k}) = 1$ and for focusing media, the expression under the square root in Eq. 3.11 is positive for $k^2 < s/\alpha$, thus the $gain_{MI}$ is a real value. This means that MI exist for any $k^2 < s/\alpha = 4\rho$ or when $\rho = 1$, for $k < 2$. Thus, $k_{trl} = 2$ is the threshold value in the gain spectrum, above which MI does not exist in local nonlinear media. In the case of a nonlocal nonlinearity, $\hat{R}(\vec{k})$ is always a bounded function, thus the MI gain band will be always narower than that for the local case. Though, the threshold value of the wavevector k_{trnl} above which MI does not exist, will be always smaller that that for the local nonlinearity $k_{trnl} < k_{trl}$. However it can never eliminate it completely. The effect of the nonlocality for sign definite response functions as the Gaussian ($R(x) = 1\sqrt{\pi\sigma}exp(-x^2/\sigma^2)$), is to suppress the growth rate of the MI. Drastically different behavior is observed in case of response functions whose spectrum is not sign definite. As an example the decaying sinusoidal response function will be considered here. As mentioned earlier, this response function approximates very well the delayed Raman effect in nonlinear optics [2]. As seen from Fig. 3.3, the spectrum of the Raman response function is not

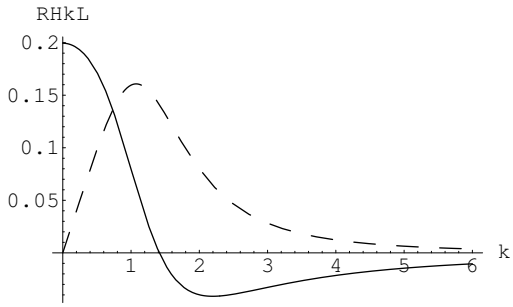

Figure 3.3: The real (solid line) and the imaginary (dashed line) parts of the spectrum of the Raman response function $R(x) = \sin(x)\exp(-|x|)$.

sign definite. This drastically changes the MI gain properties of the nonlocal NSE. For the Gaussian and the exponential response functions Fig. 3.4 (a) and (b) respectively, there is MI gain only for the focussing nonlinearity. However, for the Raman response function, MI appears for both the focussing and defocussing nonlinearity Fig. 3.4 (c) and (d) respectively. The above discussed

stability properties of the plane wave may seem to be somehow surprising in the light of the fact that what the nonlocality actually does is to smooth-out any sharp modulations of the wavefront. This is a generic property of the nonlocality independent of the particular functional representation. Therefore one would naively expect identical stability properties for all physically reasonable response functions. However, one can also look at the action of the nonlocality from a different perspective. In the Fourier domain the nonlocality acts as a filter with variable transmission determined by the form of the spectrum of the response function. For many nonlocal models such as, that represented by a Gaussian response function, the characteristic of the filter has a form of a well-behaved, sign-definite function. However, in cases, such the Raman noninstaneous response function, this filter not only modulates the amplitude of the spectral components of the signal beam (perturbation to the plane wave) but also inverts the phase of some of them. As the inversion of phase is equivalent to change of the sign of the nonlinearity (say, from defocusing to focusing), it leads, for instance, to amplification of certain harmonics in defocusing nonlinear medium.

Another interesting phenomena appearing in the field of nonlinear science and more precisely in nonlinear optics is wave collapse. It refers to the situation when strong self-focusing of waves leads to catastrophic increase (blow-up) of its intensity over finite time (or space) interval [68, 69, 71]. Wave collapse has been observed in plasma waves [72], electromagnetic waves or laser beams [73], Bose-Einstein condensates (BEC's) or matter waves [74] and even capillary-gravity waves on deep water [75]. Besides wave theory the effect of collapse has also been well known in the field of astrophysics, describing the effect of star transformation to a black hole [76, 77].

Usually, the existence of the collapse signals the limit of the applicability of the model equation. Physically, the collapse means that the approximations under which the model equation is derived are not valid anymore and additional processes have to be included that subsequently may stop the blow-up [68, 69, 71]. Nevertheless, "collapse-like" (or quasicollapse) dynamics can still occur in the real physical systems when nonlinearity leads to strong energy localisation.

The role of the nonlocality on the wave collapse was first studied by Turitsyn, who proved analytically the arrest of the collapse for a 3 specific choices of the nonlocal nonlinear response [80].

An analytical approach to beam collapse in nonlocal media is considered in [11] and [94].

In the local limit when the response function is a delta-function, the nonlinear response $\Delta n(I) = I$, which is the case of local optical Kerr media described

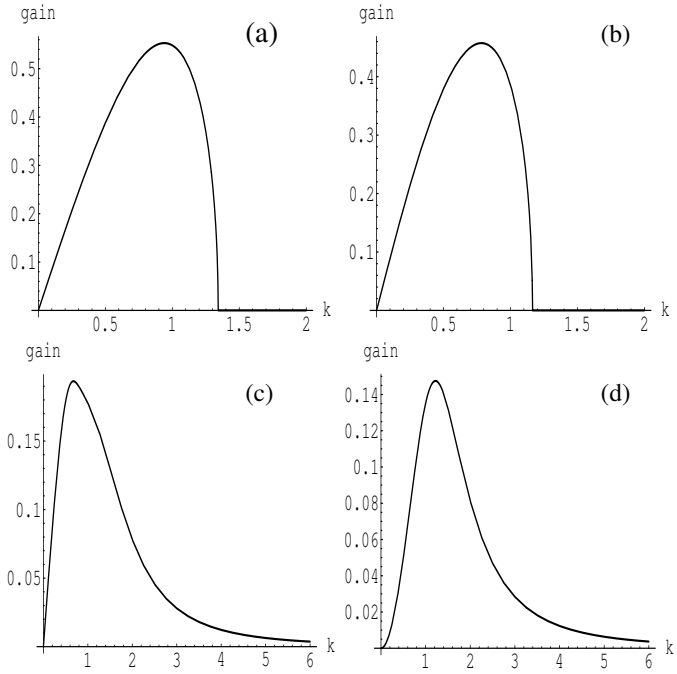

Figure 3.4: MI gain spectra Eq.3.11 calculated for $\rho = 1$. (a) gaussian response function $\exp(-x^2)$ and focussing nonlinearity. (b) exponential response function $\exp(-|x|)$ and focussing nonlinearity. Decaying sinusoidal (Raman) response function $\sin(x)\exp(-|x|)$ and focussing (c) and defocussing (d) nonlinearity.

by the conventional NLS equation and of BEC's described by the standard G-P equation. It is in this local limit that multidimensional optical beams with a power higher than a certain critical value would experience unbounded self-focusing and *collapse* after a finite propagation distance [68, 69, 71].

It can be easily shown that in the two extreme limits of a weakly and highly nonlocal nonlinear response the collapse is prevented [43, 82]. The stabilising effect of the nonlocality can be illustrated by the properties of the stationary solutions of Eqs. (3.1)-(3.4). It was shown by a variational technique [83], that for the simplest example of a Gaussian nonlocal optical response, the beam collapse is arrested [94].

In the 2D NSE equation the collapse is a critical collapse and the stationary solutions are "only" marginally unstable [69]. Typically any perturbation will act against the self-focusing, with several effects, such as non-paraxiality and

saturability, completely eliminating the possibility of a collapse [71].

Another important illustration of the stabilizing character of the nonlocality is provided by considering propagation of vortex beam in a self-focusing medium. Such a beam has a form of bright ring with a helical phase front. They are characterized by the so called charge defined as a closed loop contour integral of the wave phase modulo 2π. Typical example is the Gaussian-Laguarre beam

$$\psi(\vec{r}) = r \exp(-(r/r_0)^2) \exp(i\phi), \tag{3.12}$$

where r and ϕ are the radial and angular coordinates, respectively. This beam represents a vortex of charge one. Beams of such structure have been considered as candidates for vortex-type solitons in nonlinear self-focusing media [85]. However, it is well known that vortex beams cannot form stable stationary structures and disintegrate rather quickly when launched in the self-focusing nonlinear medium [86]. It turns out that the higher the charge the quicker the break-up of the beam occurs. To overcome this problem it has been proposed to co-propagate with the vortex another, mutually incoherent, nodeless beam. Such an object called vector or multi-component beam can form stable soliton. On the other hand, one can expect stabilization of the vortex beam by utilizing a nonlocal character of the nonlinearity. If the extent of the nonlocality is comparable with the size of the vortex beam then the resulting refractive index change will have form of broad circular waveguide which could trap the vortex beam ensuring its stable propagation, see [94].

3.2 Dark nonlocal solitons

Solitons are localized waves that propagate without change through a nonlinear medium. This is possible when the dispersion or diffraction associated with the finite size of the wave is balanced by the nonlinear change of the properties of the medium induced by the wave itself. Solitons are universal in nature and have been identified in physical systems, such as fluids, plasmas, solids, matter waves, and classical field theory. Temporal optical solitons - non-dispersive pulses of laser light - are already used in dispersion-managed high data rate optical fibre communication systems [37]. Spatial optical solitons - self-trapped light beams - have been proposed as building blocks in future ultra-fast all-optical devices. Spatial solitons can be used to create reconfigurable optical circuits that guide other light signals. Circuits with complex functionality and all-optical switching or processing can then be achieved through the evolution and interaction of one or more solitons [38]. The concept has now been verified in several optical materials [39, 40] and a number of new soliton effects have emerged through these studies, such as fusion, fission, and formation of bound states. A very

important fact is that the optical power needed to create such virtual circuits has been reduced to the milliwatt and even microwatt level, thus bringing the concept nearer to practical implementation.

Dark solitons are solutions to nonlinear equations, whose intensity profile exibits a dip in a uniform background. The dark soliton is called black if the intensity goes to zero in the center and gray if it is just smaller than the background intensity [2, 53]. A main difference between the dark and the bright solitons is that for dark solitons, the amplitude's phase changes across the transverse direction. Thus, the dark solitons are topological objects. A consequence of the transverse coordinate dependence of their phase is that in Kerr nonlinear meadium, higher-order dark solitons neither form a bound state nor follow a periodic evolution pattern [2]. This is due to the nonvanishing assymptotics of the optical field. As is well known, the exact dark soliton solution for the one dimensional NSE 2.1 is:

$$E(x,z) = \tanh(x/\sqrt{2})\exp(iz) \tag{3.13}$$

A bound state of solitons can be in some extent considered as a package of solitons, (i.e. solitons with form quite close to a single soliton solution), which are superposed close to each other. Thus, to form a bound state, packed dark solitons will be always out of phase, which as expected leads to a repulsive interaction between them. Indeed, Zhao and Bourkoff [101], who first numerically studied the propagation of closely packed dark temporal solitons in optical fibers, found that their interaction was repulsive and weak compared to that of bright solitons. Experimental studies of temporal and spatial dark solitons proved that their repulsion is generic [103]. To suppress the repulsion of the dark solitons in Kerr nonlinear media, different approaches have been pursued. Afanasjev *et al* proposed a perturbed NSE with incorporated higher-order gain terms [104]. Ostrovskaya *et al* proposed solitonic gluons, weak bright beams guided by dark solitons [105].

It was shown earlier that dark solitons and bound states of dark solitons exist in $\chi^{(2)}$ nonlinear materials [97]. However, it appeared later that these exact dark soliton solutions, are unstable due to MI of the backround [96]. Exact dark soliton solutions was shown to exist in weakly nonlocal cubic nonlinear media [52]. Further, due to analogy between the quadratic $\chi^{(2)}$ nonlinearity and cubic nonlinear nonlocal media [92, 91], exact dark soliton solutions and bound states of them (twin hole dark solitons) for a nonlocal nonlinear medium with arbitrary degree of nonlocality were found [91, 93].

3.2.1 χ^2 analogy and dark soliton bound states

Here the results presented in paper B will be overviewed.

It is well known, that the formation of solitons in quadratic nonlinear (or $\chi^{(2)}$) materials does not involve a change of the refractive index [87]. This in some sense leaves the underlying physics of quadratic solitons obscured by the mathematical model. Recently Assanto and Stegeman interpreted the self-focusing, defocusing, and soliton formation in $\chi^{(2)}$ materials by cascading phase shift and parametric gain [88].

It was also shown, that the stationary bright in-phase [92] soliton solutions in $\chi^{(2)}$ and nonlocal cubic nonlinear media are physically identical [92], and the formation of bound states of bright in phase solitons in $\chi^{(2)}$ media was explained by the nonlocality. Recently the $\chi^{(2)}$-nonlocal analogy was also used to show, that bright out of phase and dark solitons can also form bound states, provided the width of the nonlocality is enough to bound the first mode after the zeroth[91]. The possibility to form stationary bound states, does not at all tell anything about the dynamical properties. Indeed, as it was shown recently, the dynamics and stability is different for the $\chi^{(2)}$ and the stationary corresponding nonlocal model[93, 94].

The detailed description of the $\chi^{(2)}$-nonlocal analogy is described in [91, 92] and for completeness presented here.

Considering a fundamental wave (FW) and its second harmonic (SH) propagating along the z-direction in a $\chi^{(2)}$ crystal under conditions for type I phase-matching, the normalized dynamical equations for the slowly varying envelopes $E_{1,2}(x,z)$ are then [95]

$$\begin{aligned} i\partial_z E_1 + d_1\partial_x^2 E_1 + E_1^* E_2 \exp(-i\beta z) = 0 \\ i\partial_z E_2 + d_2\partial_x^2 E_2 + E_1^2 \exp(i\beta z) = 0. \end{aligned} \tag{3.14}$$

In the spatial domain $d_1 \approx 2d_2$, $d_{1,2} > 0$, and x represents a transverse spatial direction. In the temporal domain $d_{1,2}$ is arbitrary and x represents time. β is the normalized phase-mismatch. Physical insight into Eqs. (3.14) may be obtained from the cascading limit, in which the phase-mismatch is large, $\beta^{-1} \to 0$. Writing $E_2{=}e_2 \exp(i\beta z)$ and assuming slow variation of $e_2(x,z)$ gives the nonlinear Schröedinger (NLS) equation $i\partial_z E_1 + d_1\partial_x^2 E_1 + \beta^{-1}|E_1|^2 E_1 = 0$, with $e_2{=}E_1^2/\beta$. However, this model wrongly predicts several features that are known not to exist in Eqs. (3.14) and even for stationary solutions it is inaccurate, since the term $\partial_x^2 E_2$ is neglected [91].

To obtain a more accurate model a slow variation of the SH field is assumed $e_2(x,z)$ in the propagation direction only (i.e., only $\partial_z e_2$ is neglected). The relation between the FW and SH is then a convolution, leading to the *nonlocal equation for the FW*

$$\begin{aligned} i\partial_z E_1 + d_1\partial_x^2 E_1 + \beta^{-1}\Delta n(E_1^2)E_1^* = 0, \\ \Delta n(E_1^2) = \int_{-\infty}^{\infty} R(x-\xi)E_1^2(\xi,z)d\xi, \end{aligned} \tag{3.15}$$

with $E_2{=}\beta^{-1}\Delta n\exp(i\beta z)$. Equations (3.15) show that the interaction between the FW and SH is equivalent to the FW propagating in a medium with a nonlocal nonlinearity. In the Fourier domain (denoted with tilde) the response function $R(x)$ is a Lorentzian $\widetilde{R}(k){=}1/(1+s\sigma^2k^2)$, where $\sigma{=}|d_2/\beta|^{1/2}$ represents the degree of nonlocality and $s{=}\mathrm{sign}(d_2\beta)$. Both Eqs. (3.14) and (3.15) are trivially extended to more transverse dimensions.

For $s{=}{+}1$, where the $\chi^{(2)}$-system (3.14) has a family of bright (for $d_1{>}0$) and dark (for $d_1{<}0$) soliton solutions [98], $\widetilde{R}(k)$ is positive definite and localized, giving $R(x) = (2\sigma)^{-1}\exp(-|x|/\sigma)$. It is possible to show, e.g., that in this case the nonlocal model (3.15) does not allow collapse in any physical dimension [91], a known property of the $\chi^{(2)}$ system (3.14) not captured by the cascading limit NLS equation. The cascading limit $\beta^{-1}\to 0$ is now seen to correspond to the local limit $\sigma\to 0$, in which the response function becomes a delta function, $R(x)\to\delta(x)$. With the nonlocal analogy one can further assign simple physically intuitive models to the weakly nonlocal limit $\sigma{\ll}1$ (large mismatch $|\beta|{\gg}1$) and the strongly nonlocal limit $\sigma{\gg}1$ (small mismatch $|\beta|{\ll}1$). For $s{=}{-}1$, $\widetilde{R}(k)$ has poles on the real axis and the response function becomes oscillatory with the Cauchy principal value $R(x){=}(2\sigma)^{-1}\sin(|x|/\sigma)$. In this case the propagation of solitons has a close analogy with the evolution of a particle in a nonlinear oscillatory potential. In fact, it is possible to show that the oscillatory response function explains the fact that dark and bright quadratic solitons radiate linear waves [98].

Equations (3.15) show the important novel result, that in contrast to the conventional nonlocal NSE equation treated in detail in this work, the nonlocal response of the $\chi^{(2)}$ system depends on the square of the FW, not its intensity. Thus, the phase of the FW enters into the picture and one cannot directly transfer the known dynamical properties of plane waves and solitons, such as stability. The general model (3.15) and its weakly and strongly nonlocal limits thus represents novel equations, whose properties potentially allow to understand yet unexplained dynamical properties of quadratic solitons. In contrast, the stationary properties of nonlocal solitons, such as how their profiles de-

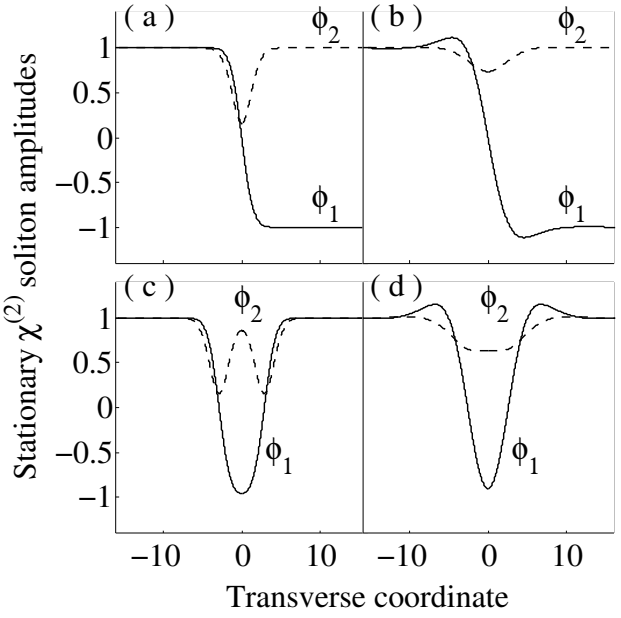

Figure 3.5: Stationary $\chi^{(2)}$ soliton amplitudes ϕ_1 (solid line) and ϕ_2 (dashed line). Single dark soliton with nonlocality parameter $\sigma = 0.5$ (a) and $\sigma = 4.0$ (b). Bound state with $\sigma = 0.5$ (c) and $\sigma = 4.0$ (d)

pend on material parameters, directly apply to quadratic solitons. Consider stationary solutions to Eqs. (3.14) in the form $E_1(x,z) = a_1\phi_1(\tau)\exp(i\lambda z)$ and $E_2(x,z) = a_2\phi_2(\tau)\exp(i2\lambda z + i\beta z)$, where the profile $\phi_{1,2}(\tau)$ is real, $\tau = x\sqrt{|\lambda/d_1|}$, $a_1^2 = \lambda^2|d_2/(2d_1)|$, and $a_2 = \lambda$. This scaling reduces the number of free parameters to one and transforms Eqs. (3.14) into the following system [98]

$$\begin{aligned} s_1\phi_1'' - \phi_1 + \phi_1\phi_2 = 0, \\ s_2\phi_2'' - \alpha\phi_2 + \phi_1^2/2 = 0, \end{aligned} \tag{3.16}$$

where $s_{1,2}$=sign$(\lambda d_{1,2})$, $\alpha = (2+\beta/\lambda)|d_1/d_2|$, and prime denotes differentiation with respect to the argument. The properties of solitons described by Eqs. (3.16) are well-known [98]. A family of bright (dark) solitons exist for s_2=s_1=+1 (s_2=$-s_1$=1) and $\alpha > 0$. We do not consider the combinations s_2=s_1=-1 and s_2=$-s_1$=-1. Equations (3.16) have the SH solution $\phi_2 = \gamma\Delta n(\phi_1^2)$, with $\gamma = 1/(2\alpha)$ and the nonlocal nonlinearity $\Delta n(\phi_1^2) = \int R(\tau-\xi)\phi_1^2(\xi)d\xi$. For sign$(s_2\alpha) = +1$ the response function is $R(\tau) = \exp(-|\tau|/\sigma)/(2\sigma)$, with the

degree of nonlocality $\sigma = |\alpha|^{-1/2}$, and Eqs. (3.16) then give the exact nonlocal model for the FW in the $\chi^{(2)}$ system

$$s_1\partial_\tau^2\phi_1 - \phi_1 + \gamma\phi_1 \int R(\tau-\xi)\phi_1^2(\xi)d\xi = 0, \tag{3.17}$$

where γ is the strength of the nonlinearity.

$$i\partial_z U_1 + d1\partial_x^2 U_1 + \beta^{-1}U_1 \int R(x-\xi)|U_1(\xi)|^2 d\xi = 0. \tag{3.18}$$

If the response function in the conventional nonlocal nonlinear Schröedinger equation 3.18 is $R(x) = \exp(-|x|/\sigma)/(2\sigma)$, then equation 3.18, reduces to the system of equations:

$$i\partial_z U_1 + d1\partial_x^2 U_1 + \beta^{-1}U_2U_1 = 0, -\beta U_2 + d_2\partial_x^2 U_2 + |U_1|^2 = 0. \tag{3.19}$$

Considering stationary soliton solutions of 3.19 of the form $U_1(x,z) = a_1\phi_1(\tau)\exp(i\lambda z)$ and $U_2(x,z) = a_2\phi_2(\tau)$, where $a_1^2 = \lambda^2|d_2/(2d_1)|$, $a_2 = \lambda$, and $\tau = x\sqrt{|\lambda/d_1|}$, then equations 3.19 are transformed to the $\chi^{(2)}$ soliton system 3.16, but with the effective mismatch parameter defined as $\alpha = (\beta/\lambda)|d_1/d_2|$. *Thus, the $\chi^{(2)}$ and nonlocal stationary soliton solutions are equivalent.* However, the dynamical evolution of the stationary soliton

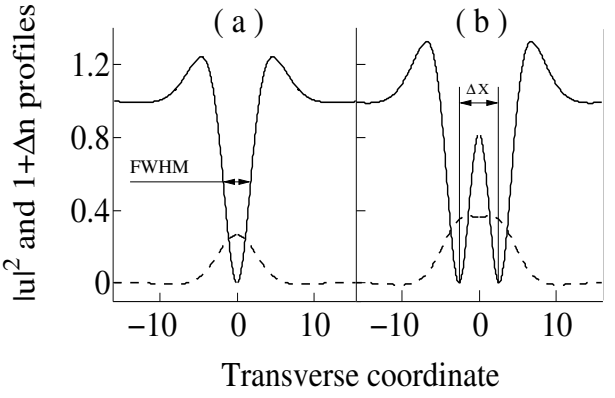

Figure 3.6: Intensity (solid line) and refractive index (dashed line) of single dark soliton (a) and bound state (b). The degree of nonlocality $\sigma = 4.0$

solutions of the dynamical $\chi^{(2)}$ 3.14 and nonlocal 3.19 systems might be significantly different. Indication for this is that the nonlocality of the nonlinearity in equation 3.18 is on the light intensity, and again it is the intensity $|U_1|^2$ in the second equation of the corresponding system 3.19, while in the dynamical $\chi^{(2)}$ system it is the square of amplitude. Thus, the influence of the phase of

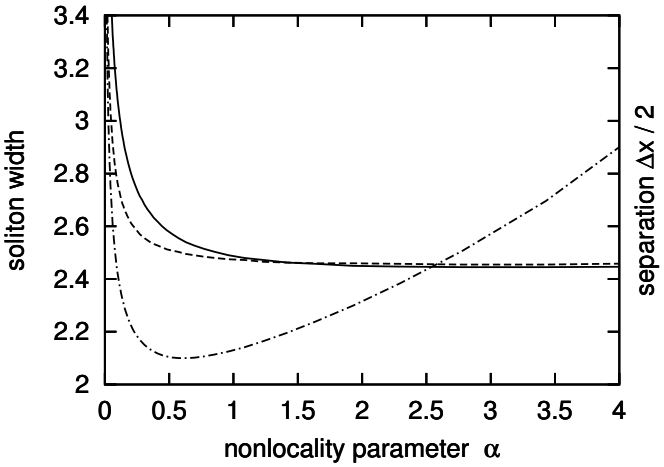

Figure 3.7: Single dark soliton FWHM (solid line), FWHM of the single soliton in a two soliton bound state (dashed line) and the half distance between the two humps of a two dark solitons bound state (dash dotted line).

the optical field U_1 on the nonlinearity in system 3.19 is neglected. As will be shown later, this is detrimental for the stability of dark solitons of the nonlocal NSE 3.18.

The stationary nonlocal soliton model (3.17) is identical to the conventional nonlocal model for stationary solitons and thus it has the same weakly and strongly nonlocal limits with the same exact bright and dark soliton solutions.It was recently shown that the nonlocal model elegantly explains the structural properties of both bright and dark solitons and their bound states as well as provides very good approximate quadratic soliton solutions in large regimes of the parameter space [91]. The possibility for formation of bright in phase bound states of nonlocal solitons was previously discussed in [92]. Here, for simplicity only a discussion on the profiles of the 1-D dark nonlocal solitons and their bound states will be presented. In Fig. 3.5 the amplitudes (ϕ_1) and the refractive index changes (ϕ_2) for a single dark solitons for two different nonlocalities $\sigma = 0.5$ and $\sigma = 4.0$ and their bound states are shown. Interesting properties of these nonlocal-$\chi^{(2)}$ dark soliton profiles are their nonmonotonic tails. In Fig. 3.6, the intensity profiles together with the intensity induced refractive index are printed for the single dark soliton (a) and the corresponding bound state for the degree of nonlocality $\sigma = 4.0$. From Fig.3.6 (b) the waveguiding mechanism is clearly demonstrated. The intensity induced refractive index change, traps the two holes in the dark soliton bound state. This, as will be explained in details later,

leads to a stable propagation of the dark soliton bound state [93]. Connecting to the formalism of the $\chi^{(2)}$ analogy, it should be noted, that the induced refractive index, corresponds to the SH intensity. Important feature of the stationary dark soliton solutions of the $\chi^{(2)}$ system 3.14, is that for $\sigma < 1/\sqrt{8}$, the single dark solitons have monotonic and for $\sigma > 1/\sqrt{8}$ nonmonotonic or oscilatory tails [87]. This property is directly connected with the possibility of the single dark solitons to form bound states. For $\sigma < 1/\sqrt{8}$ dark soliton bound states are not possible and for $\sigma > 1/\sqrt{8}$ they are possible [87]. This property can be nicely depicted, by considering the single dark soliton full width at half intensity maximum (FWHM) and the single soliton FWHM in a bound state as shown at Fig. 3.6. In Fig. 3.7, the two single dark soliton widths in a single state and in the two dip bound state are shown together with the half of the seperation distane between the two dips in the bound state $\Delta x/2$. As it is seen from Fig. 3.7, the two single dark soliton widths are approaching to each other when the nonlocality parameter α is increasing and the degree of nonlocality $\sigma = |\alpha|^{-1/2}$ is decreasing respectively. This is expected, since for values of $\sigma < \sigma_c$ the bound state of two dark soliton solutions should dissapear and the FWHM of the single dark soliton and the FWHM of the single dark soliton in the two dip bound state will not be distinguished anymore. The vanishing of the bound state for σ bellow the critical value of $1/\sqrt{8}$, can be depicted by observing the infinite growth of $\Delta x/2$ for large values of α. This is explained with the numerical algorithm for finding the dark soliton bound states, that fails to find a bound state for big α and small σ, and relaxes to two widely separated single dark solions.

3.2.2 Dynamics and interaction of dark nonlocal solitons

So far mainly the properties of individual beams in nonlocal nonlinear media were discussed. It is natural to expect strong influence of the nonlocality on interaction of well separated localised waves and solitons. For instance, in case of two nearby optical beams each of them will induce refractive index change extending into the region of the other one, hence affecting its trajectory. One can actually show that in a self-focusing medium nonlocality always provides an attractive force between interacting bright solitons. This effect has been recently demonstrated in case of interaction of bright solitons formed in a liquid crystal [88]. It has been shown that even out-of-phase solitons, which in the local medium always repel, experienced strong attraction, which could only be overcome by a sufficiently large initial divergence of the soliton trajectories [88].As a consequence of the nonlocality aided attraction bound states of the out-of-phase solitons (multisolitons) could be formed [93].

In this section, novel phenomena associated with interaction of dark solitons in nonlocal nonlinear medium with self-defocusing type of nonlinearity will be

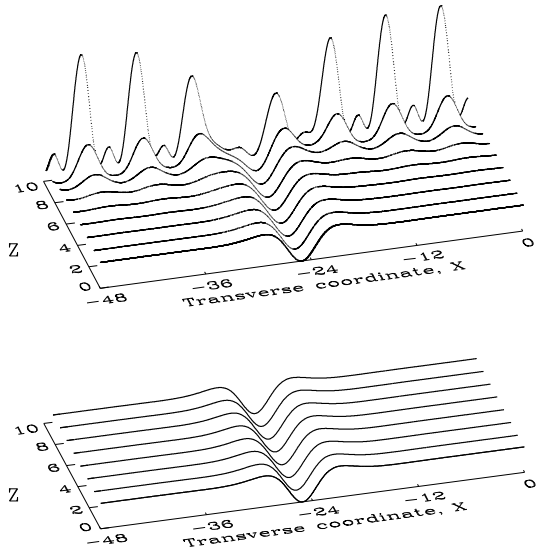

Figure 3.8: Top: Fundamental intensity $|E_1(x,z)|^2$ of a dark soliton propagating in the $\chi^{(2)}$-system 3.14 with $d_2 = -d_1 = 1$ and $\beta = -1.9$. Below: Intensity $|U_1(x,z)|^2$ of the same dark soliton propagating in the corresponding nonlocal system 3.19 with $d_2 = -d_1 = 1$ and $\beta = 0.1$. In both cases the dark soliton is the same solution of Eqs. 3.16 with $s_2 = -s_1 = 1$ and $\alpha = 0.1$.

described. As was noted in the previous section, propagation of optical dark solitons in the self-defocusing nonlinear Schröedinger equation has a repulsive nature. In paper C, interaction of dark solitons were investigated. Here these investigations will be previewed and more detailed results will be provided. Without the loss of generality, the following normalized response function is concidered $R(x) = \frac{1}{2\sigma}\exp(-|x|/\sigma)$. As was shown in the previous section, the nonlocal nonlinear Schröedinger equation with the exponential response is formally equivalent to the system of coupled Eqs.(3.14) describing stationary profiles of optical solitons in quadratic nonlinear materials. According to Ref. [98], this system predicts the existence of a single fundamental dark soliton solutions with non-monotonic tails above a certain critical value of the σ_c and as a result bound states involving two or more solitons can be formed. To test stability of the soliton bound states the dynamical equation Eq. (3.15) with the exact soliton bound state solution as initial condition are numerically integrated. Numerical simulations confirm stable propagation of single solitons and their bound states over distance of hundreds of diffraction lengths, see paper C. In Fig. 3.8, propagation of 1-D single dark soliton in $\chi^{(2)}$ (top) and nonlocal (bottom) media is displayed. The initial condition for the two types of nonlinear systems is one and the same, this is a single dark soliton solution

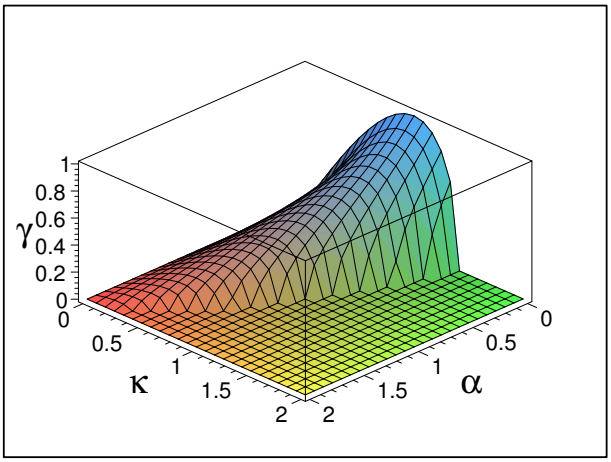

Figure 3.9: MI gain spectrum for equation 3.14 with $d_2 = -d_1 = 1\ \alpha = 0.1$, as given in [71]

for the stationary system of differential equations. Even though the stationary solutions are the same, the dynamics of the two systems is drastically different as seen from Fig. 3.8. The propagation of the dark soliton solution in $\chi^{(2)}$ medium experiences MI of the backround, which destroys the dark soliton. This is exactly predicted from the MI gain profile shown in Fig. 3.9 and calculated for the dynamic $\chi^{(2)}$ system, Eqs. 3.14 as in [71]. Interestingly, the propagation of the same initial condition in the nonlocal NSE 3.1 is MI stable. This is a direct consequence of the intensity induced nonlinear nonlocal response, that implies a self-waveguiding of the dark beam.

The concept of nonlocal soliton induced refractive index change, explaines the attraction of dark solitons in nonlocal nonlinear medium. It can be illustrated by considering interaction of dynamically formed dark solitons by a phase modulation as an initial condition. In paper C, it is shown that the nonlocality of the nonlinearity induces attraction of dark solitons and further, for a proper value of the parameters, initial soliton velocities can be compensated. This behaviour is shown in Fig. 3.10 as in paper C, where two π (a) and 0.95π (b) phase jumps are used for an initial condition to generate two dark solitons without and with opposite transverse velocities, Fig. 3.10 (a) and (b) respectively. It is important to note, that the dark solitons may not exibit attraction, provided the initial seperation distance x_0 is too large, i.e. $x_0 = 5.5$ Fig. 3.10 (a) left. In this case the degree of nonlocality is not enough to spread the refractive index change induced from the one soliton over the regions where the other soliton is propagating, and thus the dynamically formed dark solitons propagate as individual entities. If the initial seperation distance is decreased to $x_0 = 4.0$, the two dark

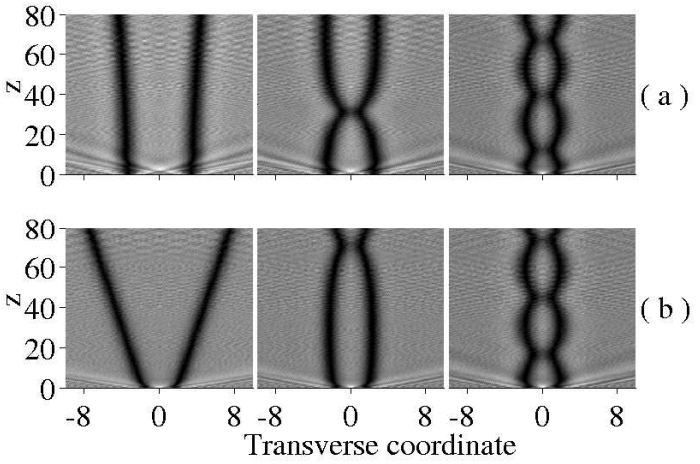

Figure 3.10: Dark nonlocal solitons formed by phase modulation of a cw background. In (a) the phase jump is π and the degree of nonlocality is $\sigma = 2.0$, and the initial soliton separation is $x_0 = 5.5, 4.0, 2.5$ from left to right. In (b) the phase jump is 0.95π and $x_0 = 2.5$, and $\sigma = 0.1, 1.0, 2.0$ from left to right.

solitons exibit attraction Fig. 3.10 (a), center. Further decrease of x_0 to 2.5, allows the formation of oscilating bound state of two dark solitons in nonlocal nonlinear media Fig. 3.10 (a), right. Further, provided the initial separation distnace and the degree of nonlocality are optimally chosen, it is possible to form a bound state two dark solitons, initialy propagating with opposite transverse velocities Fig. 3.10 (b). Another initial condition has been considered too. It is well known that an initial condition of narrow gap in the incident cw background (a wire imposed on a wide beam) develops into an even number of solitons, propagating in opposite directions. The wider the gap, the larger number of solitons to be formed and with smaller transverse velocities. Fig. 3.11 illustrates the dynamics and interaction of nonlocal dark solitons, formed by an intensity gap over a cw background. Two different response functions are considered, Fig. 3.11 (a) is for an exponential response function with width of $\sigma_e = 2.0, 4.0, 6.0$ from left to right. At Fig. 3.11 (b) a Gaussian response function is considered, with width of $\sigma_g = 4.0, 8.0, 12.0$. When the nonlocality is strong, enough some of the dark solitons formed by the intensity gap, experience attraction. In order to compare the dark nonlocal solitons interactions for different response functions in a more accurate way, it is necessary to chose a suitable nonlocality parameter that is independent on the specific form of the response function. Though, a proper physical analysis is needed to chose

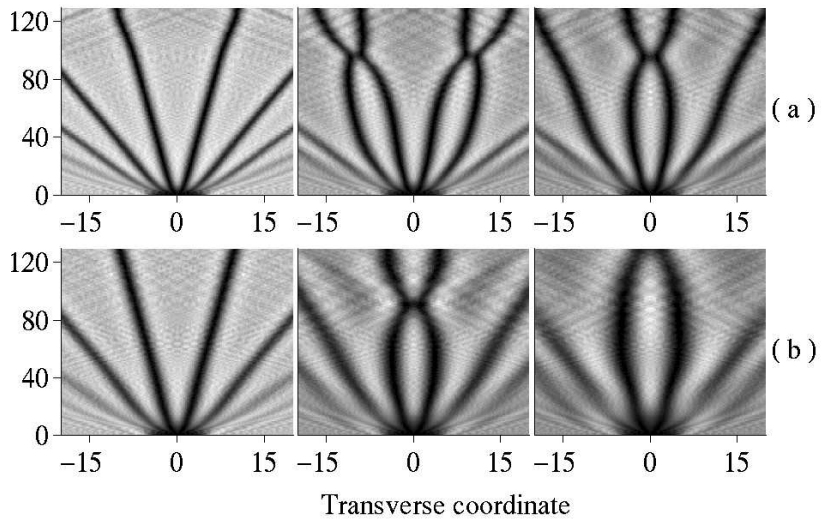

Figure 3.11: Dark nonlocal solitons formed by intensity modulation of a cw background. In (a) the wire width is $x_0 = 7.5$, the nonlocal response function is exponential with $\sigma_e = 2.0, 4.0, 6.0$ from left to right. In (b) the wire width is $x_0 = 7.5$, the nonlocal response function is gaussian with $\sigma_g = 4.0, 8.0, 12.0$ from left to right.

a response-function-form independent nonlocal width, the integral width determined by $\sigma_I = \sqrt{\int x^2 R(x) dx}$ is used here. The idea is that the overal spreading of the nonlinearity in this way will be the same, and hopefully similar dark soliton interaction will be observed. This is really proved by Fig. 3.11, where dark solitons produced in nonlocal media with a Gaussian and exponential response functions with equal integral widths, behave similarly. The values of σ_g are chosen such that the integral width for the exponential response function and the Gaussian are identical, and which results in $\sigma_e = 2.0\sigma_g$.

The dark soliton attraction in nonlocal nonlinear media can be demonstrated and by another numerical experiment in which the two formed solitons are with opposite initial velocities. In this way the two dynamically formed solitons are always forced to interact, or hit each other. Several different scenarious of interaction are observed. When the degree of nonlocality is almost negligible as in Fig. 3.12 $\sigma = 0.1$, the interaction is always ellastic scattering. For higher nonlocality, formation of oscilating bound states is possible as seen in some of the examples of Fig. 3.13 (b) middle, 3.14, 3.15 (a), and 3.16. The ability for dark solitons to form bound states and their subsequent stability is a direct

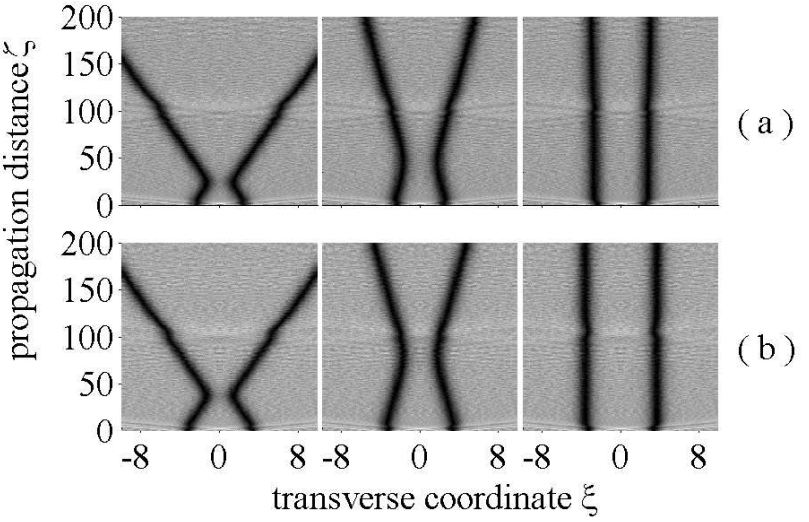

Figure 3.12: Dark nonlocal solitons formed by phase modulation of a cw background for degree of nonlocality $\sigma = 0.1$. In (a) the initial soliton separation is $x_0 = 4.0$ and the initial phase jump is 0.95π, 0.98π and π, from left to right. In (b) the initial soliton separation is $x_0 = 5.5$ and the initial phase jump is 0.95π, 0.98π and π, from left to right.

consequence of the *nonlocality-induced long range attraction of solitons*. This effect can be qualitatively explained using the self-guiding concept. In case of a local defocusing medium the refractive index change corresponding to two distant dark solitons has the form of two waveguides separated by the region of lower refractive index (potential barrier). In the presence of nonlocality the effect of the convolution term in Eq. (3.1) is to decrease the index difference between these two separate waveguides (lower the barrier) hence allowing light to penetrate the area between solitons what, consequently, appears as their attraction.

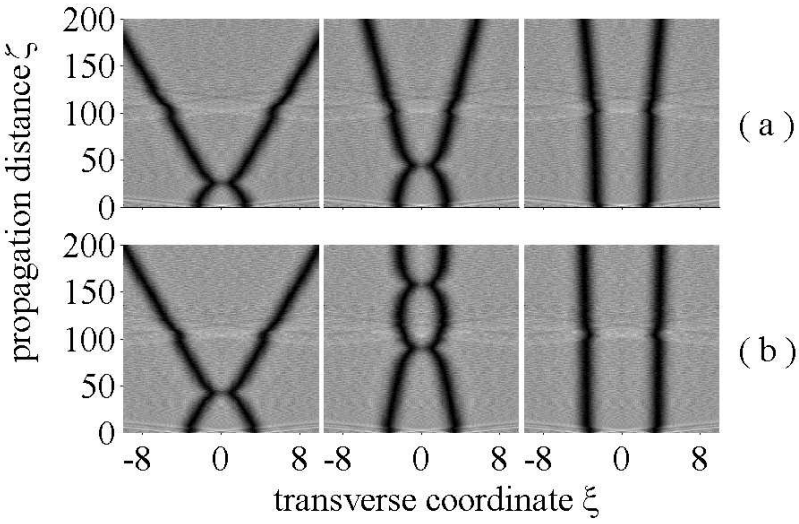

Figure 3.13: Dark nonlocal solitons formed by phase modulation of a cw background for degree of nonlocality $\sigma = 1.0$. In (a) the initial soliton separation is $x_0 = 4.0$ and the initial phase jump is 0.95π, 0.98π and π, from left to right. In (b) the initial soliton separation is $x_0 = 5.5$ and the initial phase jump is 0.95π, 0.98π and π, from left to right.

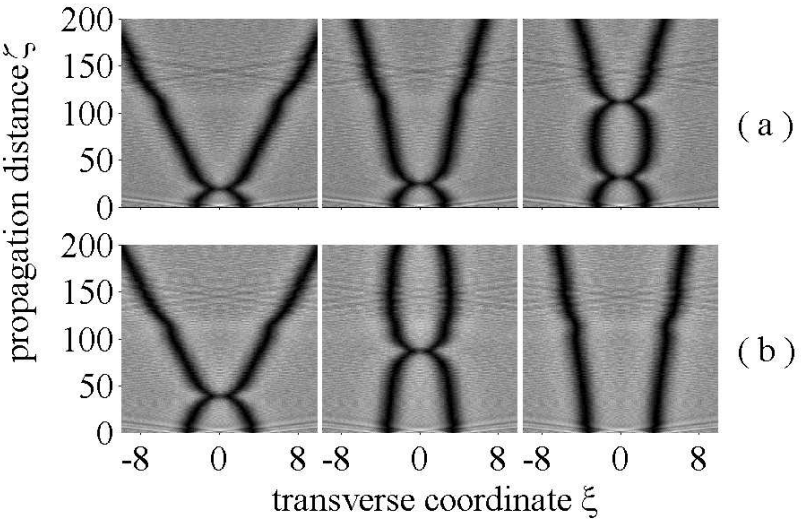

Figure 3.14: Dark nonlocal solitons formed by phase modulation of a cw background for degree of nonlocality $\sigma = 2.0$. In (a) the initial soliton separation is $x_0 = 4.0$ and the initial phase jump is 0.95π, 0.98π and π, from left to right. In (b) the initial soliton separation is $x_0 = 5.5$ and the initial phase jump is 0.95π, 0.98π and π, from left to right.

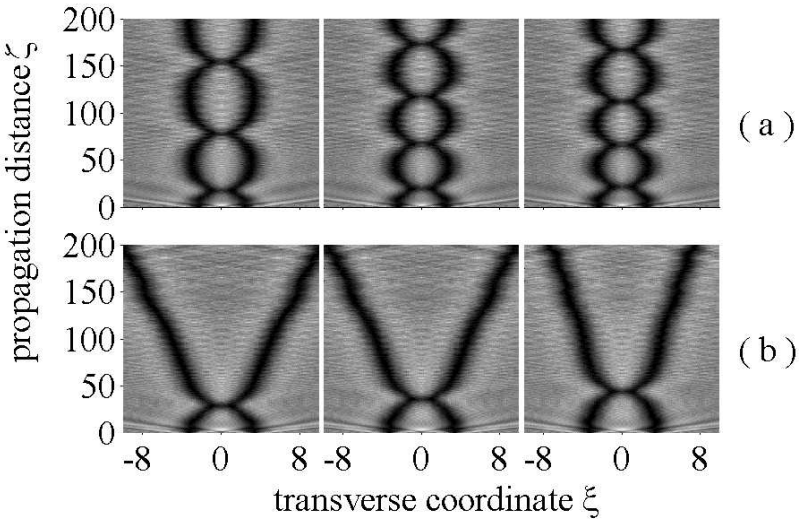

Figure 3.15: Dark nonlocal solitons formed by phase modulation of a cw background for degree of nonlocality $\sigma = 4.0$. In (a) the initial soliton separation is $x_0 = 4.0$ and the initial phase jump is 0.95π, 0.98π and π, from left to right. In (b) the initial soliton separation is $x_0 = 5.5$ and the initial phase jump is 0.95π, 0.98π and π, from left to right.

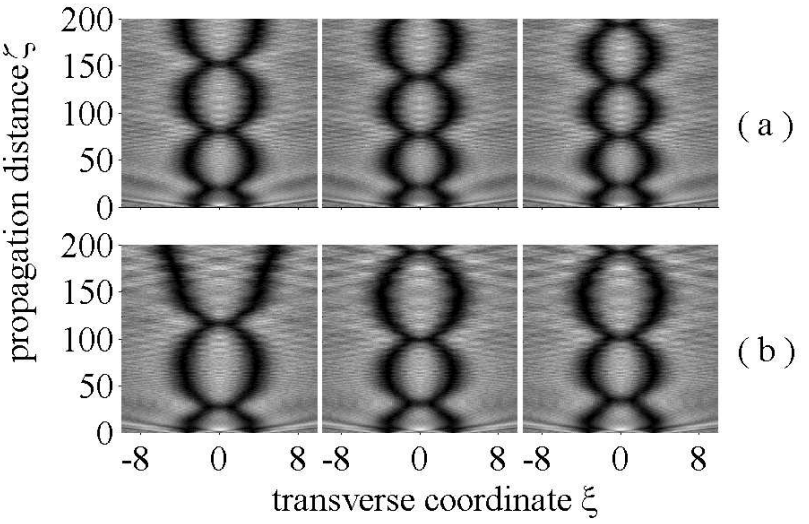

Figure 3.16: Dark nonlocal solitons formed by phase modulation of a cw background for degree of nonlocality $\sigma = 6.0$. In (a) the initial soliton separation is $x_0 = 4.0$ and the initial phase jump is 0.95π, 0.98π and π, from left to right. In (b) the initial soliton separation is $x_0 = 5.5$ and the initial phase jump is 0.95π, 0.98π and π, from left to right.

Chapter 4

Supercontinuum generation

One of the most interesting applications of nonlinear optics is the possibility for generation of new optical frequencies from a powerful laser source. Laser wavelengths are now available in almost the whole spectral range. However, the obtaining of additional frequencies is still demanded. Many fields of contemporary science such as spectroscopy, telecommunications, medical science and optical metrology need a spectrally broad continuum or white light with characteristics of a laser source, i.e., coherence and brightness. Light with these characteristics is called a supercontinuum (SC). Spectral slicing of the SC is used in telecommunication for the formation of multiple frequency channels [107, 108]. The use of a white light pulse, allows simultaneous measurement of optical characteristics in a single shot [109, 110]. Ultra-wide frequency combs are used to link optical with microwave frequencies, enabling building of an all-optical clock and comparing to the cesium microwave standard [111, 112].

SC generation is a combined effect of several nonlinear processes in different regimes leading to a dramatic spectral broadening of intense light pulses [113]. Thus numerous experimental and theoretical investigations for better understanding and control of this process have been performed. The research in the SC field aims at the generation of broader and flatter SC spectra in the whole optical domain. However, high coherence properties must be preserved by simpler experimental techniques, i.e., using low-power and low-cost light sources.

The quest for efficient SC generation requires maximization of the nonlinear optical response. As the magnetude of the specific nonlinearity of any nonlinear optical material is bounded, stronger nonlinear response is achievable by focusing intense laser pulses in bulk liquid and solid nonlinear media. Formation of a 200-THz SC spectrum of light in bulk glass was first observed in 1970 [114, 115]. Another concept of obtaining strong nonlinear optical response is the increase of the effective interaction length. Thus, highly nonlinear optical fibers proved to be an extremely promising sources for efficient SC generation. Further, the spatial characteristics of the SC light from an optical fiber can be also improved. Thus, single mode SC generation was shown to be possible.

Fundamental nonlinear processes contributing to the formation of a SC spectrum are self- and cross-phase modulation, various parametric processes and stimulated Raman scattering. In bulk nonlinear materials and air, addditional nonlinear processes, that can lead to SC generation are self-focusing, multiphoton ionization and plasma formation [153, 154].

In this chapter we consider the model for SC generation in photonic crystal fibers (PCFs) [34, 35] by low-power ps pulses. Due to the multiple parametric processes involved in the SC generation with such pulses, an accurate description of the dispersion properties of the PCF is essential.

4.1 Supercontinuum generation in PCF.

The experiments in bulk materials required extremely high peak powers ($> 10MW$), achieved by focussing of intense fs pulses. Thus, for SC generation in bulk media, operation with optical powers close to the threshold for material destruction is usually required. New techniques based on the use of optical fibers as a nonlinear medium for SC generation allowed lower peak powers to be used due to the long interaction length and high effective nonlinearity [116, 117, 118, 119]. However, for the convential optical fibers it was necessary to operate near the wavelength for zero group velocity dispersion. Thus, the SC generation was restricted to the spectral region around and above 1.3μm. The use of dispersion-flattened or dispersion-decreasing fibers as nonlinear media for SC generation resulted in a flat SC spanning 1400-1700nm [120, 121] and 1450-1650nm [122], respectively. However, the spectrum was still far from the visible wavelengths.

Photonic crystal fibers (PCFs) are newly developed optical fibers that revolutionized the concepts of fiber optics. Their nontrivial transverse structure consists of multiple air holes, running along the fiber length, Fig. 4.1. Thus,

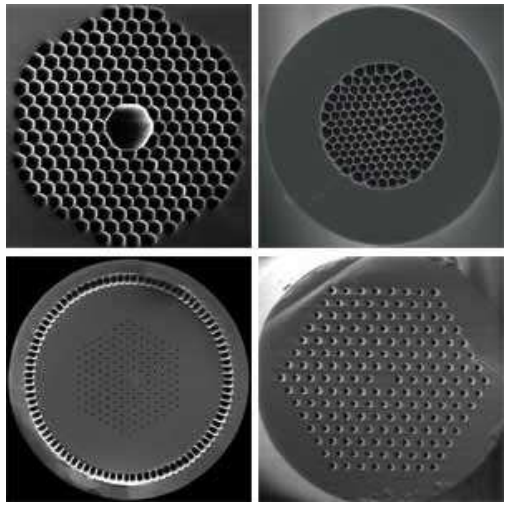

Figure 4.1: Photonic crystal fiber (PCF) structures. Top row: from left to right hollow core and higly nonlinear PCF respectively. Bottom row: from left to right, double cladding and single mode PCF respectively.

these fibers are also called microstructure fibers, which is a more precise term in the case when the transverse structure is not periodic. PCFs are classified in photonic bandgap and index guiding fibers, according to the waveguide mechanism. Like conventional fibers, index-guiding PCFs, confine light inside a solid core by total internal reflection thanks to a cladding that on average has a slightly lower index of refraction Fig. 4.1. In this case the transverse structure of the PCF, is not nessesary to be periodic. In contrast, the bandgap-guiding PCFs have periodic transverse structure with a defect in the center. Light with frequency in the bandgap of the periodic structure can be trapped and propagate along the center defect. Thus, light can be guided even along a hollow core, provided the frequency is in the bandgap of the transverse periodic structure, see for example Fig. 4.1 (top-left).

Due to the unique control over the linear and nonlinear properties of the PCFs, they have turned to be an extremely usefull tool for SC generation. The possibility to obtain PCFs with small core sizes and high NA, allows a significant increase of nonlinearity. The unprecidented dispersion control allows intrinsic phase matching of various nonlinear processes. Further, the proper structure design of the effective index guiding PCFs can lead to single-mode operation for all the wavelengths of interest [30, 31]. The highly nonlinear PCFs are effectively index-guiding fibers, with a significantly reduced core size, having a diameter around $\approx 1\mu m$). Thus, a significant increase in the nonlinearity is

possible without the addition of doping elements. The highly nonlinear PCFs were shown to be useful in various applications targeting effective nonlinear processes. However, due to their unique dispersion properties, the process of supercontinuum (SC) generation became their fundamental application.

Highly nonlinear PCFs and tapered fibers have similar dispersion and nonlinear characteristics. Tapered fibers are produced by heating and streching conventional fibers. Their cross-sectional diameter or area is adiabatically reduced. This means, the change of fiber diameter is slow enough in the axial direction so that energy of existing modes get little reflected back and couple as little as possible into other order modes [126]. However, PCFs have the advantage they are not limited by length and that their dispersion can be significantly modified by a proper design of the cladding structure [31, 123, 124, 125], while for the tapered fibers this can be achieved by changing the degree of tapering [126].

SC spanning 400-1500nm, has been experimentally achieved by seeding kilowatt-peakpower femtosecond pulses in a PCF [127] and in a tapered fiber [126]. The observed broad SC has been explained to be a result of self phase modulation (SPM) and direct degenerate four-wave-mixing (FWM) [128]. Later, it was also reported that a SC spanning from 380 to 1600nm is obtainable using 200fs pulses with an energy less than 5nJ [129]. In this case, the SC is theoretically explained to be due to nonlinear processes such as fission of higher order solitons [129, 130, 131].

It was later experimentally and theoretically shown, that high power femtosecond lasers are not needed for the observation of SC generation. SC was achieved with low-power picosecond [119, 117] and even nanosecond [132] pulses. Coen *et al.* demonstrated a broad SC in a PCF with picosecond pulses and sub-kilowatt peakpower. The primary mechanism for the SC generation in this case was shown by numerical modelling, to be due to a combined effect of SRS and parametric FWM [119].

The observed SC with 200 fs high-power pulses and a 1cm long tapered fiber was extending beyond the obtainable spectra due to SPM solely. Gusakov has shown that direct degenerate FWM can lead to ultra wide spectral broadening and pulse compression [128] in such experiments.

It was recently shown, that the efficiency of the SC generation by low-power ps pulses, can be significantly improved if the spectral bands generated by direct degenerate FWM, broaden and merge with the main SC part [134]. This significantly improves the efficiency of the SC generation, since the power in the Stokes and anti-Stokes lines is no longer lost.

Improvement of the SC generation by enhancing the role of the parametric pro-

cesses, such as direct degenerate FWM, relies on the possibility to fabricate PCFs with a proper dispersion. It is theoretically predicted that by varying the hole size and pitch in a triangular silica-air PCF, an ultra flattened dispersion is achievable [123, 124]. Flat dispersion profiles with slope within $0.017\text{ps}/(\text{nm}^2 \cdot \text{km})$ have been obtained [136]. Recently, a new fiber structure with a three-fold symmetry has been shown to enable unprecedented dispersion control, while maintaining low loss and a high nonlinear coefficient [137].

In real optical fibers, different types of imperfections are present. Further external perturbations combined with the fiber imperfections, can lead to fluctuations of the fiber parameters along the length of the fiber. Fluctuations in fiber birefringence [139, 140], dispersion [141, 142, 143], and nonlinearity [144, 145] has been investigated to understand their influence on different regimes of light propagation. As parametric processes require phase matching, the effectiveness of the FWM could be strongly influenced by random fluctuations of the dispersion. Indeed Coen *et.al.* in their PCF experiments with low-power picosecond pump pulses at 647nm [119, 117] and nanosecond pump pulses at 532nm [132] explains the absence of frequencies generated by direct degenerate FWM from the pump, by the large frequency shift and the violation of the required phase-matching condition due to fiber irregularities. However, it was recently shown, that the proper dispersion design can avoid the destructive role on the SC generation of the dispersion fluctuations along the fiber [134]. Further, by varying the core diameter of a cob-web PCF [138], dispersion profiles similar to those predicted to give the most efficient SC generation, was shown to be manufacturable [134, 135].

4.2 Applications of the SC

Continuum light sources have applications in various fields as: laser spectroscopy, optical tomography, remote sensing, optical system characterization and wavelength division multiplexing in telecommunications. Numerous investigations have been performed in order to optimize the properties of the SC to meet the requirements for different applications (for an overview see [151]). In this section some examples of applications of a SC light are given.

4.2.1 Pulse Compression

Ultrashort optical pulses find applications in optical communication, ultrafast measurements, or high-intensity laser-matter interactions. In optical commu-

nication ultrashort pulses offer a large potential bandwidth and in ultrafast measurements they can offer the time-scale necessary to resolve the dynamical process under study. For laser-matter interactions short pulses can be required to obtain the desired peak power.

Most laser sources generating sub-picosecond pulses rely on the process of mode-locking. Generation of shorter pulses as long as a single period, requires additional pulse compression techniques to be used. Though, different methods for pulse compression have been proposed and developed, all of them rely on broadening of the spectrum and simultaneously or separately synchronising the pulse spectrum. The traditional method for pulse compression is based on the Kerr nonlinearity in waveguides to produce spectral broadening by self-phase modulation SPM and subsequent chirp compensation by anomalous dispersion carefully designed linear optical elements such as prism pairs, chirped mirrors, or spatial light modulators [155]. Pulses down to 5 fs were generated using single-mode fibers [156] and 4.5 fs by hollow fibers filled with a noble gas [157]. However, as only the pulse spectral components with linear chirp can be compensated by the optical elements, the quality of the compressed pulse is limited due to higher order dispersion in the grating and the optical fiber [155]. Numerous methods for dynamic pulse compression have been proposed, where simultaneously the spectra of the pulse broadens and the phases of the aquired chirp is compensated. Such methods for pulse compression as higher-order soliton generation, higher-order SRS or XPM induced pulse compression are promissing tools for short-pulse extraction. Nevertheless, if the phase of a supercontinuum spectra can be totally synchronized, this would allow extremely effective short pulse formation in the whole spectral domain. It was theoretically shown that the SC generation process can be optimized to allow an exact compensation of the phase shift of the supercontinuum by a liquid-crystal spatial light modulator [161].

4.2.2 Remote sensing

The light detection and ranging (LIDAR) technique is a routinely employed tool for providing atmospheric pollution monitoring. The effectiveness of this technique can be signifficantly increased if a continuum wavelength laser source is used instead of a tunnable one [152]. In this case a wide range of pollutants can be detected simmultaneously. Indeed it has recently been shown that a supercontinuum based lidar technique can be used due to he ultrawide spectral broadenning of intense laser pulses propagating in air [153, 154].

4.2.3 Medical viewing

Optical coherence tomography (OCT) is a noninvasive optical imaging technology that allows in vivo and in situ three-dimensional cross-sectional visualization of microstructural morphology in superficial regions of transparent and nontransparent biological tissue [162].

Because OCT uses partially coherent light, the axial resolution of the image is determined by the temporal coherence of the light source. In the case of superluminescent diodes, the axial OCT resolution is typically limited to 10-15 μm. When using broad-bandwidth light sources, the axial OCT resolution can be enhanced. The diagnosing of many diseases, including cancer in its early stages, higher resolution is necessary. New broad-bandwidth light sources, like photonic crystal fibres, and new contrasting techniques, allow the axial resolution to be improved to 0.5μm [163, 164].

4.2.4 Optical systems and telecommunications

Efficient characterization of the properties of an optical-fiber systems is an important issue in the contemporary telecommunications. SC allows the transmission spectrum and dispersion of a fiber-optic components, to be determined with only one single-shot measurement [109, 110]. In contrast, the use of tunable lasers would require the whole bandwidth of the component to be scanned.

SC light is useful in data transmission systems. An efficient way to increase the bandwidth in optical telecommunication is the dense wavelength-division multiplexing (DWDM) technique. Using DWDM, the amount of information transfer can be significantly increased by the simultaneous transmission of multiple individual channels through an optical fiber [107]. Thus, several light sources are needed for the generation of the different channels. Using SC, over 1000 DWDM channels can be generated [108] by a single light source.

4.3 Modelling of the SC generation with picosecond pulses

The model for supercontinuum generation with ps pulses in PCFs and tappered fibers, has been used extensivelly and described by many authors, see [119, 117] and the references therein. Here, for the sake of completeness, it will be

thoroughly explained.

The model used to describe the SC generation with picosecond light pulses is based on the generalized nonlinear Schrödinger equation (GNSE) [149, 146]. By definition in the process of SC generation the spectrum of the field is allowed to cover the whole optical spectrum. Thus, the "slowly varying amplitude" approximation that is valid for the describtion of nonlinear interaction between optical waves when the spectrum is narrow arround the carrier frequency is not used in the derivation of the GNSE. Further, when modelling pulse propagation in optical fibers, the direction of propagation is assumed to be determined when the refractive index along the propagation direction does not change significatly over an optical wavelength. This means, that back reflecting waves and their contribution to the nonlinearity can be neglected. In all cases of SC generation, the major nonlinear contributions comes from the $\chi^{(3)}$ nonlinear processes. Self-focussing and plasma formation are the dominant nonlinear processes leading to SC generation in bulk (solid, liquid or gaseous) nonlinear optical materials. When the nonlinear media used for the SC generation is an optical fiber, the power of the optical wave is usually below the threshold for self-focussing ($I_p << \lambda_0^2/(\pi n_2)$) [150]. Thus diffraction and plasma formation terms are neglected for the modelling of SC generation in optical fibers. Dispersion of the nonlinearity $\chi^{(3)}(\omega)$ is possible to be due to delayed nonlinear response of the medium $n_2(\omega)$, or the frequency dependence of the effective area, $A_{eff}(\omega)$. Generally the nonlinear frequency dependence of the refractive index is due to the delayed Raman response. The response time of the electronic contribution to the nonlinearity is of the order of 1fs, so usually $n(\omega) = const$ is assumed. However, due to the stimulated Raman scattering, a delayed nonlinear response has to be taken into account. When multimode operation is considered, $A_{eff}(\omega)$ should also not be neglected. The frequency dependence of the loss $\alpha(\omega)$ might be important too.

SC with low-power ps and ns pulses has been reported only in highly nonlinear PCFs and tapered fibers. Since the highly nonlinear PCFs are birefringent, the equation describing SC generation in these fibers has to include x- and y-polarization components of the field, while the dispersion and effective area are assumed to be the same for the two principle axes [134]. Thus the equation for the modelling the propagation of spectrally broad light, in nonlinear media [146, 149] has to be extended to two differential equations, for the two polarization

axes [119, 134].

$$\begin{aligned}\frac{\partial A_j}{\partial z} &= -\mu A_j + i(j-1)\delta\beta A_j + (-1)^j \frac{\Delta}{2}\frac{\partial A_j}{\partial \tau} + \frac{i}{2}\sum_{k=2}^{7} i^k \frac{\beta_k}{k!}\frac{\partial^k A_j}{\partial \tau^k} \quad (4.1)\\ &+i\gamma\left(1+\frac{i}{\omega_p}\frac{\partial}{\partial\tau}\right)\Big\{\\ &A_j f_R \int h_R(\tau-s)\left(|A_j(s)|^2+|A_{3-j}(s)|^2\right)ds\\ &+(1-f_R)\left[\left(|A_j|^2+\frac{2}{3}|A_{3-j}|^2\right)A_j+\frac{1}{3}A_j^* A_{3-j}^2\right]\Big\}.\end{aligned}$$

Here the complex fields $A_j = A_j(t,z)$ with j=1,2 are given by $A_1 = E_x$ and $A_2 = E_y \exp(i\delta\beta z)$, where E_x and E_y are the envelopes of the real linearly polarized x- and y-components. The retarded time $\tau = t - z/\overline{v}$ is in a reference frame moving with the average group velocity $\overline{v}^{-1} = (v_x^{-1} + v_y^{-1})/2$, z is the propagation coordinate along the fiber, μ is the fiber loss, $\delta\beta = \beta_x - \beta_y = \omega_0\delta n/c$ is the phase mismatch due to birefringence $\delta n = n_x - n_y$, and $\Delta = (v_x^{-1} - v_y^{-1})$ is the group velocity mismatch between the two polarization axes. The propagation constant $\beta(\omega)$ is expanded to 8^{th} order around the pump frequency ω_p with coefficients β_k keeping β_{2-7} the same for x- and y-linearly polarized components, γ is the effective nonlinearity, f_R is the fractional contribution of the Raman effect, and finally * denotes complex conjugation.

Eq. 4.1 accounts for self-phase-modulation (SPM), cross-phase-modulation (XPM), four wave mixing (FWM), and stimulated Raman scattering (SRS). The first row from the right hand side of Eq. 4.1, includes all the linear terms. The next two lines contain only terms describing nonlinear effects. The derivative in the second row that is over all the nonlinear terms, describes the self-steepening effect. The integral term on the third row is for the description of the delayed nonlinear response due to the SRS. The terms in the square brackets on the last row, describe the SPM and the XPM and FWM between the two polarisation axes, from left to right respectively. Due to the broad band validity of the model, FWM between frequences for the field of one polarisation are inherently included, provided the nessessary phase matching is satisfied.

The exact description of the Raman effect in birefringent fibers, requires the consideration of the orthogonal and parallel delayed nonlinear responses [147]. However, as is seen from Fig.1 in [147], and shown here as Fig.4.2, the orthogonal component of the Raman susceptibility h_R is generally negligible in the frequency ranges considered here, so we include only the parallel component. In Fig. 4.2, the imaginary and the real parts of the orthogonal component and

the parallel components of the Raman susceptibility as function of frequency are shown with solid and dotted curves, crosses and dashed curve respectively. Further the Raman susceptibility can be approximated by the expression [2]:

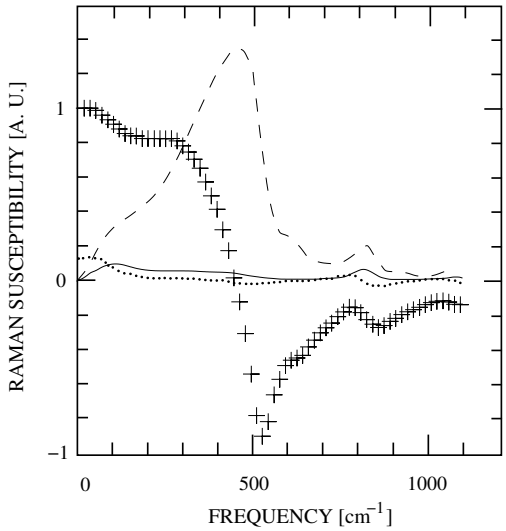

Figure 4.2: Reproduced from [147] with permission from the Optical Society of America. The solid curve and the dotted curve shows the imaginary and the real parts of the orthogonal component of the Raman susceptibility as function of frequency, respectively. The crosses and the dashed curve represent, the imaginary and the real parts of the parallel component of the Raman susceptibility, respectively.

$$h_R(t) = \frac{\tau_1^2 + \tau_2^2}{\tau_1 \tau_2^2} \exp(-t/\tau_2) \sin(t/\tau_1), \tag{4.2}$$

where τ_1=12.2fs and τ_2=32fs. Furthermore, f_R=0.18 is estimated from the known numerical value of the peak Raman gain [2].

Expression 4.2 is shown to describe the Raman response of a silica-core fibers very well, provided the values of the period τ_1 and the decay rate τ_2 are properly chosen to match the phenomenologically determined Raman gain of these fibers [148]. The period corresponds to the frequency of the peak of the Raman-gain spectrum and the decay rate corresponds to the width of the gain spectrum.

As it was stated above, equation 4.1 is derived for the total field, thus, describtion of parametric processes due to a third-order nonlinearity is automatically included in it. Therefore, generation and amplification through parametric pro-

cesses of all frequencies that are inside the spectral window of interest is possible, when the dispersion of the considered fiber allows the phase-matching condition to be fulfiled. It was recently shown, that the direct degenerate FWM process can have signifficant influence due to the generation of widely separated spectral bands [134]. Thus, it is important to consider the phase mismatch for direct degenerate FWM of two photons at the pump frequency: $\Delta\beta = \beta_s + \beta_{as} - 2\beta_p + 2\gamma I_p$ [2]. Here, I_p is the peak power, and, $\beta_{s,as}$ and β_p are the propagation constants corresponding to the Stokes, anti-Stokes and the pump frequencies. For the degenerate FWM, the Stokes and anti-Stokes spectral components have frequency shifts with opposite signs, but equal value: $\Omega = \omega_p - \omega_s = \omega_p - \omega_{as}$. Thus, the expansions of $\beta_{s,as}$ around ω_p, will cancel their odd order coefficients, and the frequency dependance of the phase mismatch will be:

$$\Delta\beta = 2\left[\Omega^2\frac{\beta_2}{2!} + \Omega^4\frac{\beta_4}{4!} + \Omega^6\frac{\beta_6}{6!} + \gamma(1-f_R)I_p\right], \tag{4.3}$$

where $\Omega = \omega_p - \omega_s = \omega_{as} - \omega_p$. The gain g of the direct degenerate FWM [117, 2] is:

$$g = \left\{[(1-f_R)\gamma I]^2 - (\Delta\beta/2)^2\right\}^{1/2}, \tag{4.4}$$

where I is the power of the frequency component generating the degenerate FWM spectra .

4.3.1 Numerical method for solving the GNSE

The GNSE Eq.4.1, is usually solved by a modification of the standard second order split-step Fourier method. In this method the linear and nonlinear parts are separately computed [2]. This can be better explained if Eq.4.1 is written in a matrix form:

$$\frac{\partial}{\partial z}\vec{A}(\omega;z) = \left(\hat{L} + \hat{S}\hat{N}\right)\cdot\vec{A}(\omega;z), \tag{4.5}$$

Here $\vec{A}$ is a two component complex vector describing the two polarizations of the optical field. $\hat{L}$ and $\hat{N}$ are complex 2×2 matrixes for the linear and the nonlinear operators respectively, with elements:

$$\begin{aligned} L_{1,1} &= -\mu(\omega) - i\frac{\Delta}{2}\omega + \frac{i}{2}\sum_{k=2}^{7}\frac{\beta_k}{k!}(i\omega)^k \\ L_{2,2} &= -\mu(\omega) + i\frac{\Delta}{2}\omega + \frac{i}{2}\sum_{k=2}^{7}\frac{\beta_k}{k!}(i\omega)^k + i\delta\beta \end{aligned} \tag{4.6}$$

$$
\begin{aligned}
N_{j,\,j} &= (1-f_R)\left(|A_j|^2 + \frac{2}{3}|A_{3-j}|^2\right) \\
&\quad + f_R h_R(\omega)\left[|A_j(\omega)|^2 + |A_{3-j}(\omega)|^2\right] \\
N_{j,3-j} &= \frac{1-f_R}{3} A_j(\omega)^* A_{3-j}(\omega) \\
S_{j,j} &= i\gamma\left(1 + i\frac{\omega}{\omega_p}\right)
\end{aligned}
\tag{4.7}
$$

The linear operator is actually represented by a constant matrix containing explicitly the propagation coordinate z. Thus, if the split-step integration procedure starts with the linear operator, two constant matrixes will be need, one for the full propagation step Δz and one for the half. For this reason, starting the integration with the nonlinear operator is preffered. The computation of the linear operator is done in the frequency domain. This is very convenient as the time derivatives in the frequency domain are replaced by a simple multiplication with frequency. The losses $\mu(\omega)$ are also defined as a spectral charcteristic. However, the calculation of the nonlinear operator is more complicated. It was

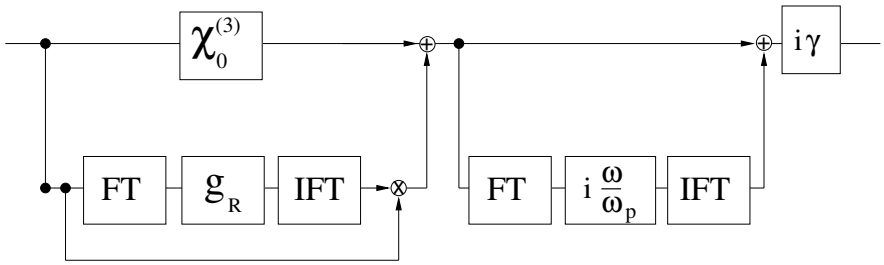

Figure 4.3: Scheme for the numerical procedure for computing the nonlinear term of the GNSE 4.1, if a single polarization mode is assumed.

previously shown [119, 146], that the numerical integration of the nonlinear part can be done by a second-order Runge-Kutta method and applying the convolution theorem, while the derivative in front the nonlinear term is treated as a perturbation. However, in this case the conservation of the photon number is already violated by 5% after approximately 60000 integration steps. Recently, a better procedure for calculation of the nonlinear operator was proposed [134] and presented in papers D and E. Fig. 4.3 illustrates this numerical procedure. The rectangulars denote subroutines as the fourier transform (FT), the inverse fourire transform (IFT) and the calculation of the Kerr nonlinearity $\chi^{(3)}$ which is simply the modulous of the optical field. The dots denote data used as an input for several subroutines. x is a multiplication and + a sum of several outputs. Using this numerical procedure, the accuracy of the numerical integration

was improved by calculating the nonlinear part by a fourth order Runge-Kutta method and also applying the convolution theorem. The essential difference is that the time derivative of the nonlinear part is exactly calculated by Fourier transform back and forth. In this way, the reliable propagation distance at which the photon number is conserved within the critical 5% is increased to 86000 integration steps.

However, the advantages gained from the use of equation for the total field do not come for free. Higher resolution is required for the numerical modelling, as the time step must be chosen to correctly sample the carrier wave, not the envelope. To get the highest acceptable resolution, 2^{17} points have been used [134] in a time window of $T = 236$ps, giving the wavelength window $(405 - 1613$nm). This guaranteed that all the frequency components expected to be generated are in the simulation window. As was noted, the time derivative of the nonlinear term is exactly calculated, thus, it is not nessessary to increase the resolution in the propagation step, which can be kept the same as in [119, 134] $\Delta z = 43\mu$m. Consequently, the critical violation of the photon number up to 5% determines the longest length of a PCF to be $L = 3.7$m, in a reliable simulation.

Laser sources generate pulses with some noise fluctuations of their amplitude and phase. Thus the accurate modelling of the SC generation requires seeding with a random noise of the initial condition. Previously a random phase noise was seeded of one photon per mode [119, 134]. The exact investigation of the influence of the noise on the SC characteristics requiers many simulation runs for different initial random seeds of the phase noise. Then the average of the SC at the output for the different noise seeds at the input, can be compared with the average from many experimentally measured spectra.

4.4 SC generation with picosecond pulses

SC generation with picosecond [119] and nanosecond [132] pulses have been first obtained using PCFs. In this regime, the SC generation was explained to be due to initial Raman-induced energy transfer from the pump to higher-wavelengths in the vicinity of zero-dispersion wavelength. This is followed by FWM coupling of the higher-wavelengths with lower, resulting in a symmetricaly broad continumm [119]. It was also shown experimentally [128] and theoretically [134], that the direct degenerate FWM from the pump wavelentgh can lead to further improving of the efficiency of the SC generation. In all these cases of SC generation due to the enhanced role of the parametric processes, special fibers as PCFs and tapered fibers are needed, that have unique dispersion properties. However, it was recently shown that ultrabroad SC generation is also possible in a con-

ventional longer dispersion shifted fiber[165] using nanosecond pulses from a microchip laser. In this case the broad SC of arround 1100 nm is obtained in a regime where direct degenerate FWM from the pump is not possible. Nevertheless, PCFs can still be attractive tools for SC generation, as their dispersion and nonlinear properties can be engineered in a wide range.

In this section results of the simulation of SC generation with an input of 30-ps pulses at 647 nm, and with peak power of 400 W are presented. These simulations are carried out by using the GNSE 4.1. Six different dispersion profiles d1-d6, previously considered in [134] are used to analyse the influence of the direct degenerate FWM. Their dispersion coefficients from the Taylor expansion around the pump wavelength are given in Table. 4.1 and the spectra recieved from the simulation of GNSE 4.1 with the initial conditions mentioned above and dispersion the profiles d1-d6 are presented in Fig. 4.4 for propagation distances 20cm, 30cm, 1m, and 2m. The temporal evolution of the pulse in fibers with the dispersion profiles d1-d6 are shown as grey colour plots in Fig. 4.5. The initial spectral broadening around the pump observed for all the dispersion profiles d1-d6 is accompanied with the generation of widely separated spectral bands due to a direct degenerate FWM. The Stokes and anti-Stokes wavelengths for the undepleted pump power are given in Table 4.1. It is apparent that if the dispersion is properly engineered, the spectral bands around the FWM Stokes and anti-Stokes lines can broaden enough to merge with the spectrum around the pump wavelength. This clearly happens for dispersion case d3. For the dispersion cases d1 and d2 formation of an ultrabroad SC does not happen due to the large separation of the Stokes and anti-Stokes lines from the pump wavelength d1, and or the weak spectral broadenning around them d2. For d4 and d5 dispersion cases, single band spectrum do not form due to pump depletion and change of the direct degenerate FWM gain spectrum along the propagation of the fiber. As it was discussed in [134], additonal spectral components are generated for dispersion case d6, that do not belong to the gain spectrum of the direct degenerate from the pump FWM.

To get a better understanding of the dynamics of the process, it is nessessary to consider the pulse evolution in the time domain. Due to dispersion, the group velocity of light pulse is different for different frequencies. Thus light with frequency ω, shifted from the pump frequency ω_p by Ω, $\omega = \omega + \Omega$, will exibit time delay $\tau(\omega_p + \Omega)$ from the light with the pump frequency, given by:

$$\tau(\omega_p + \Omega) = \left[\frac{1}{v_{gp}} + \beta_2\Omega + \beta_3\frac{\Omega^2}{2} + \beta_4\frac{\Omega^3}{6} + \beta_5\frac{\Omega^4}{24} + \beta_6\frac{\Omega^5}{120} + \beta_7\frac{\Omega^6}{720} + ...\right] \quad (4.8)$$

Here, the time delay $\tau(\omega_p + \Omega)$ is in units of inverse velocity, i.e. time per unit length, ω_p is the pump frequency, v_{gp} is the group velocity at the pump, $\beta_{2..7}$ are

Table 4.1: Dispersion coefficients $\beta_2\,[\mathrm{ps}^2/\mathrm{km}]$, $\beta_4\,[10^{-5}\mathrm{ps}^4/\mathrm{km}]$ and $\beta_6\,[10^{-10}\mathrm{ps}^6/\mathrm{km}]$ for dispersion profiles d1-d6, with corresponding dispersion at the pump wavelength $D(\lambda_p)\,[\mathrm{ps}/(\mathrm{nm}\cdot\mathrm{km})]$, zero dispersion wavelength $\lambda_{ZD}\,[\mathrm{nm}]$ and Stokes $\lambda_s\,[\mathrm{nm}]$, anti-Stokes $\lambda_{as}\,[\mathrm{nm}]$ wavelengths and the walk-off time field with Stokes $\Delta\tau_s\,[\mathrm{ps}]$ and anti-Stokes $\Delta\tau_{as}\,[\mathrm{ps}]$ wavelengths. Fixed coefficients: $\beta_3 = 5.1\times10^{-2}\mathrm{ps}^3/\mathrm{km}$, $\beta_5 = 1.2\times10^{-7}\mathrm{ps}^5/\mathrm{km}$, $\beta_7 = 1.2\times10^{-13}\mathrm{ps}^7/\mathrm{km}$.

case	β_2	β_4	β_6	λ_{ZD}	$D(\lambda_p)$	λ_s	λ_{as}	$\Delta\tau_s$	$\Delta\tau_{as}$
d1	7.0	-4.9	-1.8	677	-31.6	1108	457	-58.52	-38.51
d2	14	-34.4	-0.04	697	-62.3	852	522	-12.27	-15.18
d3	1.0	-2.5	-3.3	652	-4.5	849	523	-14.52	-12.26
d4	-0.28	0.05	0.29	647	1.3	1083	461	-44.41	-45.1
						822	534	-10.7	-10.4
d5	-1.01	2.14	-2.84	643	4.54	1096	459	-47.57	-45.84
						911	562	-20.45	-21.0
						735	578	-3.4	-3.0
d6	-1.3	-2.6	58.8	641	5.9	803	628	-7.3	-10.0
						713	593	-2.2	-1.5

the coeffcients in the Taylor expansion of the dispersion, and Ω is the frequency shift from the pump. Concider the time delay of the Stokes and anti-Stokes frequensies:

$$\Delta\tau_s = \tau(\omega_p) - \tau(\omega_p - \Omega) = \left[\beta_2\Omega - \beta_3\frac{\Omega^2}{2} + \beta_4\frac{\Omega^3}{6} - \beta_5\frac{\Omega^4}{24} + \beta_6\frac{\Omega^5}{120} - \beta_7\frac{\Omega^6}{720} + ...\right] \tag{4.9}$$

$$\Delta\tau_{as} = \tau(\omega_p) - \tau(\omega_p + \Omega) = \left[\beta_2\Omega + \beta_3\frac{\Omega^2}{2} + \beta_4\frac{\Omega^3}{6} + \beta_5\frac{\Omega^4}{24} + \beta_6\frac{\Omega^5}{120} + \beta_7\frac{\Omega^6}{720} + ...\right]. \tag{4.10}$$

Here, $\Delta\tau_s$ and $\Delta\tau_{as}$ are the walk-off times of the Stokes and the anti-Stokes spectral components of the direct degenerate FWM. As it is seen from Table 4.1, these wavelengths might be too far from the pump wavelength, and the zero-dispersion wavelenth of the fiber. Hence, the group velocities v_{gs} and v_{gas} and thus propagation times τ_s and τ_{as} of the light at the Stokes and anti-Stokes wavelengths will be considerablly different from these for the pump wavelength v_{gp} and τ_{gp}. The values of the walk-off times for the Stokes $\Delta\tau_s$ and anti-Sokes $\Delta\tau_{as}$ lines from the pump calculated from equation 4.10 are given in Table 4.1.

In Fig. 4.5, the pulse temporal evolution for the six d1-d6 dispersion profiles is shown as gray-colour plots. Regions with high intensity are shown in white.

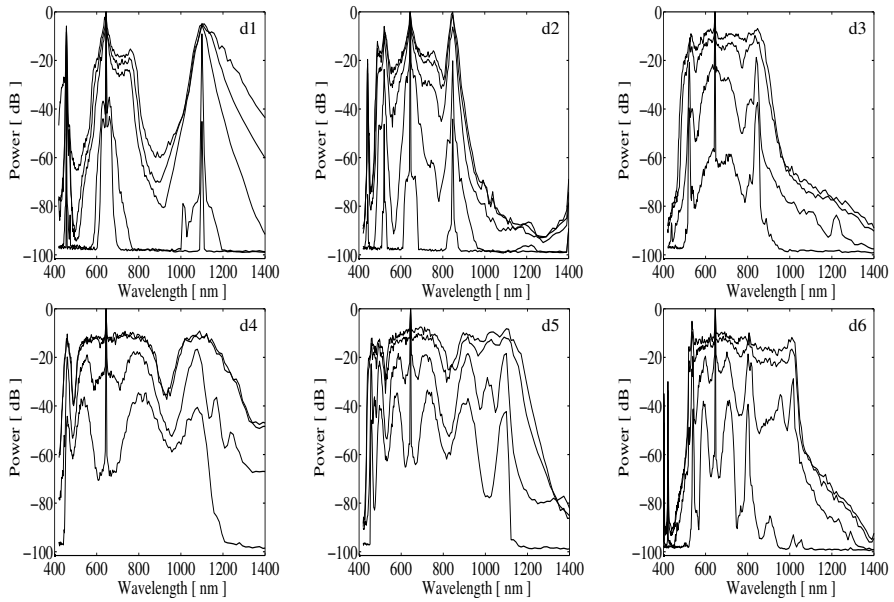

Figure 4.4: Spectrum for dispersion cases d1-d6 at L=20cm, 30cm, 1m, and 2m (down to up).

The time axis is in a reference frame moving with the group velocity of the pump. For the initial propagation distances z, in all plots the main part of the pulse does not move in the τ coordinate. However, as it is clearly seen, for longer propagation distances 4.5, for dispersion cases d1, d4 and d5, significant portion of the radiation leaves the pulse. This is seen as bunches of white stripes, propagating with nonzero transverse time - propagation length velocity, thus going out the pulse at some angle to the propagation direction z, towards the positive walk off time. The values of the walk-off times of the Stokes and anti-Stokes direct degenerate FWM spectral components from the pump given in Table 4.1, quite well agree with the observed spliting angles seen in Fig. 4.5. Realy, for dispersion case d4, the weaker pulse, splitting after z=0.5m from the pump pulse is exactly at 45ps away from the pump at z=1m. For the other dispersion cases, when there is some pulse splitting observed, it is also quite well explained by the walk-off of the Stokes and anti-Stokes direct degenerate FWM spectral components.

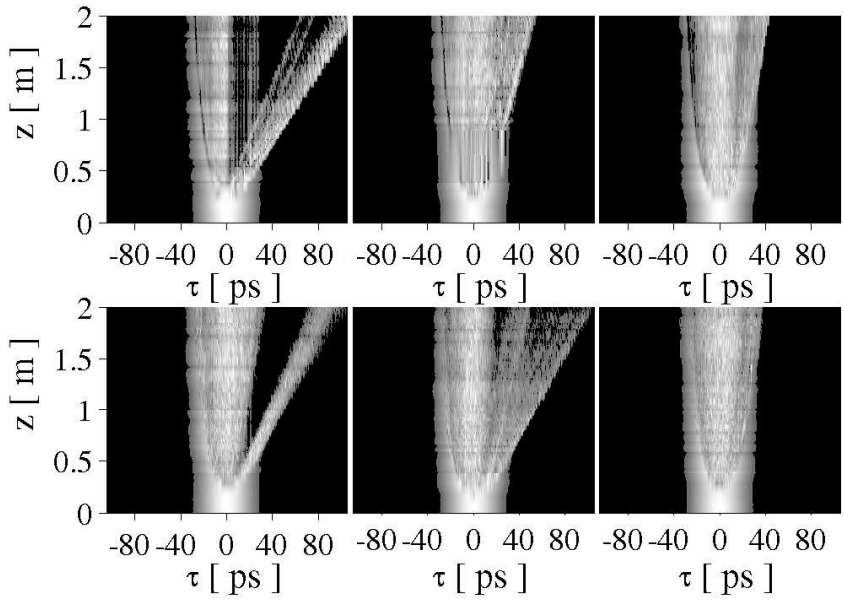

Figure 4.5: Pulse temporal evolution. Regions with high intensity are in white. Top row: from left to right dispersion cases d1-d3. Bottom row: from left to right dispersion cases d4-d6.

Chapter 5

Conclusion and further investigations

5.1 Nonlinear nonlocal optics.

In this work, nonlocal nonlinear optical meadium has been investigated. A well known fact for dark solitons and out of phase bright solitons in Kerr media is that they cannot form a bound state. Numerous theoretical and experimental investigations have proved, that their interaction is repelling. In this work, using the analogy between a quadratic nonlinear medium and cubic nonlocal nonlinear optical medium, it is demonstrated that bound states of stationary dark solitons are shown to exist. Further, numerical simulations show, that these bound states of dark solitons are stable in propagation. This is explained by the waveguiding concept. When the nonlocality of the nonlinearity is strong enough, the refractive index change of two nearby dark solitons forms a common waveguide in which the single solitons can transfrom to a higher order waveguide mode.

The studies of dark solitons in nonlocal nonlinear media are far from beeing completed. Further, the concept of the escape angle, which is the critical angle of propagation of two single dark solitons above which they cannot form a bound state, can be studied theoretically both through numerical calculations

and approximate analytical methods. The possibility to find exact single dark soliton solutions and their bound states for different nonlocal response functions also needs further investigations. Hence, the possibility of formation of stable dark solitons and bound states of them in nonlocal nonlinear media may be expected to be independent on the specific form of the response function.

The experimental study of nonlocal nonlinear effects and particularly the formation of stable bound states of dark soliton solutions will be possible with present day material and technology and it would be of great interest to verify the results. One of the most suitable medium is solutions of light absorbing dyes in transparent viscosic liquids. This type of optical materials are extremely suitable media for studying the nonlocal nonlinear effects, as by properly chosing the materials and their concentration, the degree of nonlocality and the nonlinearity can be adjusted over a wide range.

5.2 Supercontinuum generation.

The basic mechanisms and regimes of the process of SC generation have been reviewed. The model describing SC generation with pico-second pulses in cubic nonlinear optical media has been thouroughly described. Further, it is shown that the proper structure design of PCFs allows to achieve fiber dispersions most suitable for enhancing various parametric process. Thus, signifficant improvement in the process of SC generation is possible. This includes the possibility to generate ultrabroad SC by ps pulses, that is stable to strong fluctuations of the PCF's parameter due to irregularities. The temporal walk off of different spectral components is shown to be important. This should be additionally investigated to further optimize the efficiency of the SC generation. The construction of PCFs is fastly developing and with numerous applications in linear and nonlinear optics, new modifications as polymer PCFs and new fiber structures can be considered as a potential tool for a further improvement of the SC generation.

Appendix A

acronyms

DWDWM Dense Wavelength-Division Multiplexing

FW Fundamental Wave

FWHM Full Width Half Maximum

FWM Four Wave Mixing

FT Fourier Transform

GNSE Generalised Nonlinear Schröedinger Equation

IFT Inverse Fourier Transform

MI Modulational Instability

NSE Nonlinear Schröedinger Equation

PCF Photonic Crystal Fiber

SC Supercontinuum

SH Second Harmonic

SPM Self Phase Modulation

XPM Cross Phase Modulation

Appendix B

Quadratic solitons as nonlocal solitons

Nikola I. Nikolov, Dragomir Neshev, Ole Bang, and Wieslaw Królikowski, Quadratic solitons as nonlocal solitons, Physical Review E, Volume 68, 036614 (September 2003).

PHYSICAL REVIEW E 68, 036614 (2003)

Quadratic solitons as nonlocal solitons

Nikola I. Nikolov
Informatics and Mathematical Modelling, Technical University of Denmark, 2800 Kongens Lyngby, Denmark and Department of Optics and Fluid Dynamics, Risø National Laboratory, OFD-128, P.O. Box 49, 4000 Roskilde, Denmark

Dragomir Neshev
Nonlinear Physics Group and ARC Centre of Excellence for Ultrahigh-Bandwidth Devices for Optical Systems, Research School of Physical Sciences and Engineering, Australian National University, Canberra, Australian Capital Territory 0200, Australia

Ole Bang
Research Center COM and Department of Informatics and Mathematical Modelling, Technical University of Denmark, 2800 Kongens Lyngby, Denmark

Wieslaw Z. Królikowski
Laser Physics Centre and ARC Centre of Excellence for Ultrahigh-Bandwidth Devices for Optical Systems, Research School of Physical Sciences and Engineering, Australian National University, Canberra, Australian Capital Territory 0200, Australia

(Received 26 February 2003; published 26 September 2003; published 29 September 2003)

We show that quadratic solitons are equivalent to solitons of a nonlocal Kerr medium. This provides new physical insight into the properties of quadratic solitons, often believed to be equivalent to solitons of an effective saturable Kerr medium. The nonlocal analogy also allows for analytical solutions and the prediction of bound states of quadratic solitons.

DOI: 10.1103/PhysRevE.68.036614 PACS number(s): 42.65.Tg, 42.65.Ky, 42.65.Sf, 05.45.Yv

I. INTRODUCTION

Quadratic nonlinear (or $\chi^{(2)}$) materials have a strong and fast electronic nonlinearity, which makes them excellent materials for the study of nonlinear effects, such as solitons [1]. The main properties of quadratic solitons are well known [2] and both $(1+1)$-dimensional [3] and $(2+1)$-dimensional [4] bright spatial solitons have been observed experimentally. Unlike conventional solitons, which form due to a self-induced refractive index change, the formation of quadratic solitons does not involve any change of the refractive index. Thus the underlying physics of quadratic solitons is often obscured by the mathematical model. Only recently Assanto and Stegeman used the concepts of the cascading phase shift and parametric gain to give an intuitive interpretation of effects, such as self-focusing, defocusing, and soliton formation in $\chi^{(2)}$ materials [5].

Nevertheless certain features of quadratic solitons, such as formation of bound states, are still without a physical interpretation. The nice simple phase-shift approach of Assanto and Stegeman [5] predicts, e.g., that two dark solitons and two out-of-phase bright solitons will always repel and thus can never form a bound state, whereas it is known that such bound states of quadratic solitons do exist [6].

Here we use the analogy between parametric interaction and nonlocality and present a physically intuitive nonlocal theory, which is exact in predicting the profiles of stationary quadratic solitons and which provides a simple physical explanation for their properties including formation of bound states.

The nonlocal analogy was applied recently by Shadrivov and Zharov to find approximate bright quadratic soliton solutions [7]. The formal equivalence of bright solitons in nonlocal liquid crystals and parametric solitons was also discussed recently by Conti, Peccianti, and Assanto [8]. However, the nonlocal concept was not fully exploited in Refs. [7,8] to give a broad physical picture in the whole regime of existence and discuss, e.g., dark solitons and bound states of out-of-phase bright solitons.

We do that here and we go one step further in showing how a simple phase-sensitive nonlocal model provides a better description of the dynamics in $\chi^{(2)}$ materials than the nonlinear Schrödinger (NLS) equation obtained in the cascading limit.

We consider a fundamental wave (FW) and its second harmonic (SH) propagating along the z direction in a lossless quadratic nonlinear medium under conditions for type 1 phase matching. The normalized dynamical equations for the slowly varying envelopes $E_{1,2}(x,z)$ are then [9]

$$i\partial_z E_1 + d_1\partial_x^2 E_1 + E_1^* E_2 \exp(-i\beta z) = 0, \tag{1}$$

$$i\partial_z E_2 + d_2\partial_x^2 E_2 + E_1^2 \exp(i\beta z) = 0. \tag{2}$$

In the spatial domain $d_1 = 2d_2$, $d_j > 0$, and the coordinate x represents a transverse spatial direction. The term $\partial_x^2 E_j = \partial^2 E_j/\partial x^2$ then represents beam diffraction. In the temporal domain d_j is arbitrary and x represents time. In this case $\partial_x^2 E_j$ represents pulse dispersion. The parameter β is the normalized phase mismatch and $j = 1,2$.

II. GENERAL NONLOCAL MODEL

Physical insight into the properties of Eqs. (1) and (2) may be obtained from the cascading limit, in which the phase mismatch is large, $\beta^{-1}\to 0$. Writing $E_2 = e_2 \exp(i\beta z)$ and assuming slow variation of $e_2(x,z)$ gives the NLS equation

$$i\partial_z E_1 + d_1\partial_x^2 E_1 + \beta^{-1}|E_1|^2 E_1 = 0, \tag{3}$$

in which the *local* Kerr nonlinearity is due to the coupling to the SH field $e_2 = E_1^2/\beta$. The SH is thus slaved to the FW and the widths of the SH and FW are fixed. The sign of the mismatch β determines whether the effective Kerr nonlinearity is focusing or defocusing and thus the cascading limit predicts that bright and dark quadratic solitons exist for $\beta d_1 > 0$ and $\beta d_1 < 0$, respectively.

However, even for stationary solutions the NLS equation is inaccurate, since the term $\partial_x^2 E_2$ is neglected. Thus it predicts, e.g., modulational stability of dark quadratic solitons for all values of d_2, whereas this is known to depend on the value of d_2 [6]. It further predicts that in higher dimensions bright solitons are unstable and will either spread out or collapse [10], whereas it is known that stable quadratic solitons exist in all dimensions and that collapse cannot occur in the $\chi^{(2)}$ system (1) and (2) [11,12]. The stabilizing effect of the $\chi^{(2)}$ nonlinearity is often described as being due to saturation of the effective Kerr nonlinearity [5,11,13]. We show below that the nonlinearity is in fact nonlocal.

To obtain a more accurate model than that given by the cascading limit we assume a slow variation of the SH field $e_2(x,z)$ in the propagation direction only. Thus, neglecting only $\partial_z e_2$, we solve Eq. (2) exactly using Fourier transformation and the convolution theorem, treating E_1^2 as a function. The SH is still expressed in terms of the FW, but now the relation has the form of a convolution, leading to the *nonlocal equation* for the FW:

$$i\partial_z E_1 + d_1\partial_x^2 E_1 + \beta^{-1} N(E_1^2) E_1^* = 0, \tag{4}$$

$$N(E_1^2) = \int_{-\infty}^{\infty} R(x-\xi) E_1^2(\xi,z)\, d\xi, \tag{5}$$

with $E_2 = \beta^{-1} N \exp(i\beta z)$. Equations (4) and (5) clearly show that the interaction between the FW and the SH is equivalent to the propagation of a FW in a medium with a nonlocal nonlinearity. In the Fourier domain (denoted with tilde) the response function $R(x)$ is a Lorentzian $\tilde{R}(k) = 1/(1+s\sigma^2 k^2)$, where $\sigma = |d_2/\beta|^{1/2}$ represents the degree of nonlocality and $s = \mathrm{sgn}(d_2\beta)$. Both Eqs. (1) and (2) and (4) and (5) are trivially extended to include more transverse dimensions.

For $s = +1$, where the $\chi^{(2)}$ system (1) and (2) has a family of bright (for $d_1 > 0$) and dark (for $d_1 < 0$) soliton solutions [6], $\tilde{R}(k)$ is positive definite and localized, giving

$$R(x) = (2\sigma)^{-1} \exp(-|x|/\sigma). \tag{6}$$

The cascading limit $\beta^{-1}\to 0$ is now seen to correspond to the local limit $\sigma\to 0$, in which the response function becomes a δ function, $R(x)\to\delta(x)$.

With the nonlocal analogy one can assign simple physically intuitive pictures to several important cases. When the mismatch $|\beta|$ is large Eqs. (4) and (5) reduce to the so-called weakly nonlocal equation with $\sigma \ll 1$ [14]. Similarly the nearly phase-matched limit when $\beta \approx 0$ corresponds to the strongly nonlocal limit with $\sigma \gg 1$, when Eqs. (4) and (5) become effectively linear [15,16].

For $s = -1$, $\tilde{R}(k)$ has poles on the real axis and the response function becomes oscillatory in nature with the Cauchy principal value

$$R(x) = (2\sigma)^{-1} \sin(|x|/\sigma). \tag{7}$$

In this case the propagation of solitons has a close analogy with the evolution of a particle in a nonlinear oscillatory potential. In fact, it is possible to show that the oscillatory response function explains the fact that dark and bright quadratic solitons radiate linear waves for $s = -1$ [6].

Equations (4) and (5) show the important result that in contrast to the conventional nonlocal NLS equation, describing materials with a thermal [18] or diffusion [19] type nonlinearity, liquid crystals [20], and photorefractive crystals [21], the nonlocal response of the $\chi^{(2)}$ system depends on the square of the FW, not its intensity. Thus the phase of the FW enters into the picture and one cannot directly transfer the known nonlocal stability results for plane waves [15,17] and solitons [14,16].

However, the simple nonlocal model (4) and (5) is indeed an improved model of quadratic nonlinear materials, as compared with the even simpler NLS equation obtained in the cascading limit. Thus the nonlocal model correctly shows that the properties of quadratic solitons depends sensitively on the parameter d_2. For symmetric response functions, $R(x) = R(-x)$, the nonlocal model in arbitrary dimension conserves both power and Hamiltonian and it is straightforward to carry out the same analysis as for the conventional nonlocal NLS equation [16] and show that the Hamiltonian for the system (4) and (5) is also bounded from below. Thus the nonlocal model (4) and (5) also correctly predicts that collapse cannot occur in the $\chi^{(2)}$ system. Furthermore, for stationary fields $E_1(x,z) = E_1(x)$ the nonlocal model (4) and (5) represents an exact model for $\chi^{(2)}$ materials.

III. NONLOCAL QUADRATIC SOLITONS

The properties of nonlocal solitons in terms of profiles thus directly apply to quadratic solitons. Consider stationary solutions to Eqs. (1) and (2) in the form

$$E_1(x,z) = a_1\phi_1(\tau)\exp(i\lambda z), \tag{8}$$

$$E_2(x,z) = a_2\phi_2(\tau)\exp(i2\lambda z + i\beta z), \tag{9}$$

where the profile $\phi_j(\tau)$ is real, with $\tau = x|\lambda/d_1|^{1/2}$, $a_1^2 = \lambda^2|d_2/(2d_1)|$, and $a_2 = \lambda$. This scaling reduces the number of free parameters to one and transforms Eqs. (1) and (2) into the following system [6]:

$$s_1\phi_1'' - \phi_1 + \phi_1\phi_2 = 0, \tag{10}$$

$$s_2\phi_2'' - \alpha\phi_2 + \phi_1^2/2 = 0, \tag{11}$$

where $s_j = \mathrm{sgn}(\lambda d_j) = \pm 1$, $\alpha = (2+\beta/\lambda)|d_1/d_2|$, and prime denotes differentiation with respect to the argument. The properties of solitons described by Eqs. (10) and (11) are well known [6]. A family of bright (dark) solitons exist for $s_2 = s_1 = +1$ ($s_2 = -s_1 = +1$) and $\alpha > 0$. As discussed above we do not consider the combinations $s_2 = \pm s_1 = -1$, for which solitons do not exist in the whole α space.

Equation (11) has the formal solution $\phi_2 = \gamma N(\phi_1^2)$, with $\gamma = 1/(2\alpha)$ and the nonlocal nonlinearity $N(\phi_1^2)$ given by Eq. (5). For $\mathrm{sgn}(s_2\alpha) = +1$ the response function is $R(\tau) = (2\bar{\sigma})^{-1}\exp(-|\tau|/\bar{\sigma})$, with the degree of nonlocality $\bar{\sigma} = |\alpha|^{-1/2}$. Inserting the SH into Eq. (10) then gives the *exact nonlocal* model for the FW in the $\chi^{(2)}$ system (10) and (11):

$$s_1\partial_\tau^2\phi_1 - \phi_1 + \gamma\phi_1\int_{-\infty}^{\infty} R(\tau-\xi)\phi_1^2(\xi)\,d\xi = 0, \tag{12}$$

where γ is the strength of the nonlocal nonlinearity. Thus $\chi^{(2)}$ solitons are equivalent to nonlocal solitons.

In the weakly nonlocal case $\bar{\sigma} \ll 1$ (i.e., $|\alpha| \gg 1$) the response function $R(\tau)$ is much narrower than the FW intensity ϕ_1^2. Taylor expansion of ϕ_1^2 under the integral in Eq. (12) gives the weakly nonlocal model [14]

$$s_1\partial_\tau^2\phi_1 - \phi_1 + \gamma(\phi_1^2 + \bar{\sigma}^2\partial_\tau^2\phi_1^2)\phi_1 = 0, \tag{13}$$

where $\phi_2 = \gamma(1+\bar{\sigma}^2\partial_\tau^2)\phi_1^2$. This model has exact bright soliton solutions for $s_2 = s_1 = +1$ and $\alpha > 0$ [14]:

$$\pm\tau = \tanh^{-1}(\rho) + 2\bar{\sigma}\tan^{-1}(2\bar{\sigma}\rho), \tag{14}$$

where $\rho^2 = (a_1^2 - \phi_1^2)/(a_1^2 + 4\bar{\sigma}^2\phi_1^2)$, $a_1^2 = 2/\gamma$ being the maximum intensity of the FW. Exact stationary black soliton solutions exist for $s_2 = -s_1 = +1$ [14].

For $|\alpha| \ll 1$ the nonlocality is strong, $\bar{\sigma} \gg 1$, and we can expand the response function $R(\tau)$ in Eq. (12). For bright solitons we then obtain the linear equation for the FW:

$$s_1\partial_\tau^2\phi_1 - \phi_1 + \gamma P_1 R(\tau)\phi_1 = 0, \tag{15}$$

where $\phi_2 = \gamma P_1 R(\tau)$. In this eigenvalue problem the FW power $P_1 = \int_{-\infty}^{\infty}\phi_1^2(\tau)\,d\tau$ plays the role of the eigenvalue, and bright solitons correspond to the fundamental mode of the waveguide structure one can associate with the exponential response function. For $s_2 = s_1 = +1$ and $\alpha > 0$, Eq. (15) has exact bright soliton solutions in the form of the Bessel function of the first kind of order $2\bar{\sigma}$ [22]

$$\phi_1(\tau) = A_1 J_{2\bar{\sigma}}(\bar{\sigma}^2\sqrt{2P_1 R(\tau)}). \tag{16}$$

For the single-soliton ground-state solution P_1 is found as the first zero of the derivative, $J'_{2\bar{\sigma}}(\sqrt{\bar{\sigma}^3 P_1}) = 0$, which assures that $\phi_1'(0) = 0$. The amplitude A_1 is then found from the definition of P_1, giving $A_1^2 \approx P_1/2 - [P_1/(\pi^2\bar{\sigma})]^{1/2}$.

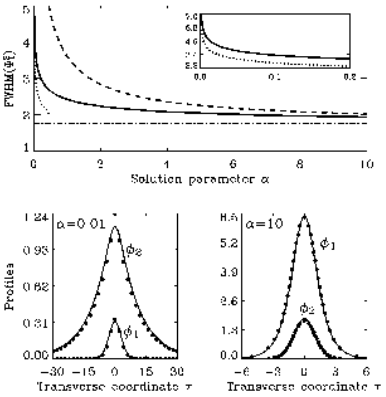

FIG. 1. Top: Numerically found FWHM(ϕ_1^2) of bright quadratic solitons vs α (solid), and the weakly nonlocal (dashed), strongly nonlocal (dotted), and cascading limit (chain-dashed) predictions. Bottom: Numerically found profiles (solid) and strongly nonlocal (left, $\alpha = 0.01$) and weakly nonlocal (right, $\alpha = 10$) solutions (dots). $s_2 = s_1 = +1$.

In Fig. 1 we show the full width at half maximum (FWHM) of the FW intensity ϕ_1^2 of bright quadratic solitons versus the phase-mismatch parameter α. The analytical solutions obtained using the nonlocal analogy correctly capture the increase of the soliton width with decreasing α. The nonlocal model elegantly explains this effect: Because of the convolution in the nonlinearity in Eq. (12) representing a trapping potential or waveguide structure, this potential is always broader than the FW intensity profile itself, leading to its weaker confinement and larger width when the degree of nonlocality increases. The profiles shown in Fig. 1 further illustrate the excellent agreement of the numerical results and approximate nonlocal analytical solutions in both the weakly ($\alpha \gg 1$) and the strongly ($\alpha \ll 1$) nonlocal limit.

The linear Eq. (15) describing the strongly nonlocal limit further predicts the existence of multihump bright solitons. Choosing P_1 as the Nth zero of the derivative of the Bessel function, i.e., the Nth root in the equation $J'_{2\bar{\sigma}}(\sqrt{\bar{\sigma}^3 P_1}) = 0$, gives solitons with an odd number of humps $(2N-1)$, as discussed in Ref. [7]. However, this does not exhaust all soliton solutions supported by the model (15). There also exist antisymmetric solitons with an even number of intensity peaks. If the power P_1 is found as the Nth zero of the Bessel function itself, and not its derivative, i.e., as the Nth root in the equation $J_{2\bar{\sigma}}(\sqrt{\bar{\sigma}^3 P_1}) = 0$ [so that $\phi_1(0) = 0$], then antisymmetric solitons with an even number of intensity peaks $(2N)$ exist with the form

$$\phi_1(\tau) = s_\tau A_1 J_{2\bar{\sigma}}(\bar{\sigma}^2\sqrt{2P_1 R(\tau)}), \tag{17}$$

where $s_\tau = \mathrm{sgn}(\tau)$. When P_1, e.g., is fixed by the first zero of $J_{2\bar{\sigma}}$ then solution (17) is a two-peak antisymmetric soliton,

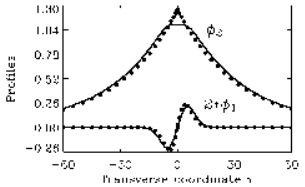

FIG. 2. Numerically found bound state of two out-of-phase bright solitons for $\alpha=0.001$ (solid) and the predicted strongly nonlocal solution (17) (dashed); $s_2=s_1=+1$.

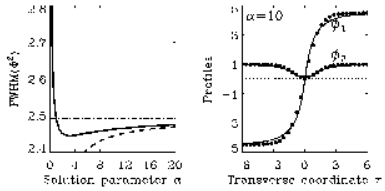

FIG. 3. Left: Numerically found FWHM(ϕ_1^2) of dark solitons vs α (solid), and the weakly nonlocal (dashed) and cascading limit (chain-dashed) predictions. Right: Numerically found profiles (dots) and weakly nonlocal solutions (solid) for $\alpha=10$. $\phi_1^2(\pm\infty)=2\alpha$, $\phi_2(\pm\infty)=1$, and $s_2=-s_1=+1$.

which can be interpreted as a bound state of two out-of-phase fundamental solitons. In Fig. 2 we have shown the bound state of two out-of-phase fundamental solitons predicted by Eq. (17), and the corresponding numerically found solution for $\alpha=0.001$. We see again that the strongly nonlocal model provides an excellent prediction of this bound state quadratic soliton solution.

In fact, all higher order solitons can be thought of as a bound state of a number of individual solitons. Formation of such bound states follows naturally from the nonlocal character of the nonlinear interaction. Consider two out-of-phase solitons, for which the intensity in the overlapping region is always zero. In local Kerr media the nonlinear change in the refractive index is decreased in the overlap region, as compared to the index change generated by a single soliton. This leads to a mutual repulsion of the solitons. The nonlocality tends to increase the nonlinear change of the refractive index in the overlapping region, and for a sufficiently high degree of nonlocality, the index change may even be higher than that for a soliton in isolation, despite the solitons being out of phase. This creates an attractive force and leads to formation of the bound state.

The linear equation for dark solitons in the strongly nonlocal limit ($\alpha \ll 1$) has the form

$$s_1\partial_\tau^2\phi_1-\phi_1+\gamma\{A_1^2-Q_1R(\tau)\}\phi_1=0, \qquad (18)$$

where $Q_1=\int_{-\infty}^{\infty}[A_1^2-\phi_1^2(\tau)]d\tau$ is the complementary FW power and $\phi_2=\gamma[A_1^2-Q_1R(\tau)]$. For $s_2=-s_1=+1$ and $\alpha>0$, Eq. (18) has exact dark soliton solutions in the form of the zeroth order Bessel function:

$$\phi_1(\tau)=s_\tau\sqrt{2\alpha}J_0(\bar{\sigma}^2\sqrt{2Q_1R(\tau)}). \qquad (19)$$

For the fundamental single-soliton solution Q_1 is found as the first zero $J_0(\sqrt{\bar{\sigma}^3}Q_1)=0$, which gives $Q_1=5.8/\bar{\sigma}^3$ and assures that $\phi_1(0)=0$. The background amplitude is fixed at $A_1^2=2\alpha$. Choosing the Nth root gives antisymmetric multihump dark solitons with $2N-1$ dips in the intensity profile. Choosing instead the Nth zero of the derivative, i.e., $J_0'(\sqrt{\bar{\sigma}^3}Q_1)=0$ gives symmetric multihump dark solitons with $2N$ dips in the intensity profile.

In the strongly nonlocal limit the bright soliton is the *fundamental mode* of the waveguide structure $R(\tau)$ and much narrower than the waveguide. In contrast the dark soliton is a *first mode* of the waveguide $R(\tau)$ at the cutoff and as such its width is comparable with that of the waveguide. Hence the expansion procedure leading to Eq. (18) is not a good approximation. This is reflected in the fact that the fixed background amplitude A_1 does not satisfy the self-consistency relation $Q_1=\int_{-\infty}^{\infty}[A_1^2-\phi_1^2(\tau)]d\tau$. Nevertheless the strongly nonlocal model is able to predict and physically explain the existence of multihump dark quadratic solitons found earlier [6].

In Fig. 3 we show the full width at half maximum of the FW intensity ϕ_1^2 of dark quadratic solitons versus the mismatch parameter α. The dark solitons have the constant background $\phi_1^2(\pm\infty)=2\alpha$, $\phi_2(\pm\infty)=1$. The analytical weakly nonlocal dark soliton solution exists for $\alpha>2$ and was taken from Ref. [14]. Unlike bright solitons, whose width is a monotonic function of α, dark solitons are seen to have a minimum width at $\alpha=\alpha_0\approx 3.1$.

Figure 3 confirms that for $\alpha>\alpha_0$ the weakly nonlocal model correctly predicts how the soliton width decreases when the mismatch parameter decreases. This, as well as the appearance of the minimum in the soliton width, is again elegantly explained by the nonlocal analogy: Because of the convolution in the nonlinearity in Eq. (12) representing the trapping potential or waveguide structure, the contibution from the constant background tends to contract this potential. This leads to a stronger confinement and thus a smaller width of the soliton. However, this is only true as long as the amplitude of the trapping potential is not affected by nonlocality, as in the weakly nonlocal regime. For a high degree of nonlocality (i.e., smaller value of α) not only the width of the trapping potential, but also its amplitude is affected. In this regime the nonlocality leads to a drop in the amplitude of the potential, resulting in a weaker confinement and an increase of the soliton width. The profiles shown in Fig. 3 further illustrate the excellent agreement of the numerical results and approximate nonlocal analytical solutions in the weakly nonlocal limit $\alpha \gg 1$.

IV. CONCLUSION

In conclusion, we have used the analogy between parametric interaction in quadratic media and nonlocal Kerr-type nonlinearities to provide a physically intuitive theory for

quadratic solitons, which allows for a deeper physical insight into their properties and an exact description of their profiles. Quadratic solitons are characterized by a single solution parameter α, which is an effective mismatch parameter depending on both the real phase mismatch and the power. We have shown that the nonlocal theory provides a simple and elegant explanation for how the soliton width depends on the mismatch α.

In particular the nonlocal analogy provides simple physical models in both the large mismatch limit $\alpha \gg 1$ and the near cutoff limit $|\alpha| \ll 1$, corresponding to the regimes of weak and strong nonlocality, respectively. Our results show that the weakly nonlocal approximation gives an accurate description of quadratic solitons in a relatively broad range of their existence domain. Also, the simple linear physics of the strongly nonlocal limit has enabled us to find bound states of bright quadratic solitons and explain their formation using the natural concept of the nonlocality-based attraction between out-of-phase constituent solitons.

Finally we have discussed how a simple phase-sensitive nonlocal model provides a better description of the dynamics as compared to the standard NLS equation obtained in the cascading limit.

ACKNOWLEDGMENTS

The research was supported by the Danish Technical Research Council (Grant No. 26-00-0355) and the Australian Research Council.

[1] For a recent review see G. Stegeman, D.J. Hagan, and L. Torner, **28**, 1691 (1996).
[2] For a recent review see A.V. Buryak, P. Di Trapani, D.V. Skryabin, and S. Trillo, Phys. Rep. **370**, 63 (2002).
[3] R. Schiek, Y. Baek, and G.I. Stegeman, Phys. Rev. E **53**, 1138 (1996).
[4] W.E. Torruellas, Z. Wang, D.J. Hagan, E.W. Van Stryland, G.I. Stegeman, L. Torner, and C.R. Menyuk, Phys. Rev. Lett. **74**, 5036 (1995).
[5] G. Assanto and G.I. Stegeman, Opt. Express **10**, 388 (2002).
[6] A.V. Buryak and Yu.S. Kivshar, Phys. Lett. A **197**, 407 (1995).
[7] I.V. Shadrivov and A.A. Zharov, J. Opt. Soc. Am. B **19**, 596 (2002).
[8] C. Conti, M. Peccianti, and G. Assanto, Phys. Rev. Lett. **91**, 073901 (2003).
[9] C.R. Menyuk, R. Schiek, and L. Torner, J. Opt. Soc. Am. B **11**, 2434 (1994); O. Bang, *ibid.* **14**, 51 (1997).
[10] For a recent review see Yu.S. Kivshar and D.E. Pelinovsky, Phys. Rep. **331**, 117 (2000).
[11] L. Bergé, V.K. Mezentsev, J.J. Rasmussen, and J. Wyller, Phys. Rev. A **52**, R28 (1995).
[12] L. Bergé, O. Bang, J.J. Rasmussen, and V.K. Mezentsev, Phys. Rev. E **55**, 3555 (1997).
[13] F. Wise and P. Di Trapani, Opt. Photonics News **13**, 28 (2002).
[14] W. Krolikowski and O. Bang, Phys. Rev. E **63**, 016610 (2001).
[15] W. Krolikowski, O. Bang, J.J. Rasmussen, and J. Wyller, Phys. Rev. E **64**, 016612 (2001).
[16] O. Bang, W. Krolikowski, J. Wyller, and J.J. Rasmussen, Phys. Rev. E **66**, 046619 (2002).
[17] J. Wyller, W. Krolikowski, O. Bang, and J.J. Rasmussen, Phys. Rev. E **66**, 066615 (2002).
[18] A.G. Litvak, V.A. Mironov, G.M. Fraiman, and A.D. Yunakovskii, Fiz. Plazmy **1**, 60 (1975) [Sov. J. Plasma Phys. **1**, 31 (1975)].
[19] D. Suter and T. Blasberg, Phys. Rev. A **48**, 4583 (1993).
[20] D.W. McLaughlin, D.J. Muraki, and M.J. Shelly, Physica D **97**, 471 (1996); M. Peccianti, K.A. Brzdakiewicz, and G. Assanto, Opt. Lett. **27**, 1460 (2002).
[21] A. Mamaev, A. Zozulya, V.K. Mezentsev, D.Z. Anderson, M. Saffman, Phys. Rev. A **56**, R1110 (1997); G.F. Calvo, F. Agullo-Lopez, M. Carrascosa, M. Belic, and W. Krolikowski, Europhys. Lett. **60**, 847 (2002).
[22] E.M. Conwell, Appl. Phys. Lett. **23**, 328 (1973).

Appendix C

Attraction of nonlocal dark optical solitons

Nikola I. Nikolov, Dragomir Neshev, Wieslaw Królikowski, Ole Bang, Jens Juul Rasmussen, and Peter Leth Christiansen, Attraction of nonlocal dark optical solitons, Optics Letters, Volume 29, 286 (February 2004).

286 OPTICS LETTERS / Vol. 29, No. 3 / February 1, 2004

Attraction of nonlocal dark optical solitons

Nikola I. Nikolov

Informatics and Mathematical Modelling, Technical University of Denmark, 2800 Kongens Lyngby, Denmark, Optics and Fluid Dynamics Department, Risø National Laboratory, OFD-128, 4000 Roskilde, Denmark

Dragomir Neshev and Wiesław Królikowski

Research School of Physical Sciences and Engineering, Australian National University, Canberra, ACT 0200, Australia

Ole Bang

Informatics and Mathematical Modelling and Research Center COM, Technical University of Denmark, 2800 Kongens Lyngby, Denmark

Jens Juul Rasmussen

Optics and Fluid Dynamics Department, Risø National Laboratory, OFD-128, 4000 Roskilde, Denmark

Peter L. Christiansen

Informatics and Mathematical Modelling, Technical University of Denmark, 2800 Kongens Lyngby, Denmark

Received August 21, 2003

We study the formation and interaction of spatial dark optical solitons in materials with a nonlocal nonlinear response. We show that unlike in local materials, where dark solitons typically repel, the nonlocal nonlinearity leads to a long-range attraction and formation of stable bound states of dark solitons. © 2004 Optical Society of America

OCIS codes: 190.5530, 190.4420.

Solitons are robust objects that display particlelike behavior during interaction.[1] In different nonlinear systems the details of their interaction may vary, but their generic features remain universal.[2] Dark solitons, which have an intensity profile in the form of a dip in an otherwise uniform background, are topological objects because of their nontrivial phase structure. It appears that dark solitons always repel,[3] unless special external perturbations are imposed. Already early theoretical studies of the self-defocusing nonlinear Schrödinger equation have indicated the repulsive nature of dark soliton interaction.[4] The first systematic investigations were conducted by Zhao and Bourkoff,[5] who numerically studied the propagation of closely packed dark temporal solitons in optical fibers and found that their interaction was repulsive and weak compared with that of bright solitons. Subsequent experimental studies of temporal[6] and spatial dark solitons[7–9] confirmed that their repulsive interaction is generic. To suppress the repulsion of dark solitons, Afanasjev *et al.* perturbed the Kerr response of a nonlinear medium by incorporating higher-order gain terms.[10] Ostrovskaya *et al.*[11] proposed the use of "solitonic gluons," i.e., two out-of-phase weak bright beams guided by closely spaced dark solitons.

Here we discuss propagation of dark solitons in a nondissipative self-defocusing nonlocal Kerr-like medium. We show that nonlocality drastically modifies the interaction of dark solitons by inducing a long-range attraction between them, thereby permitting the formation of stable dark soliton bound states for what is to our knowledge the first time in a homogeneous medium without external perturbations.

We consider the evolution of a one-dimensional optical beam $u = u(x, z)$ described by the nonlocal nonlinear Schrödinger equation

$$i\partial_z u + \partial_x{}^2 u + \Delta n(I)u = 0\,,$$

$$\Delta n(I) = -\int_{-\infty}^{\infty} R(x - \tau)I(\tau)\mathrm{d}\tau\,, \qquad (1)$$

where $I = I(x, z) = |u|^2$ is the intensity, z is the evolution coordinate, x represents a transverse coordinate, and Δn is the nonlinear refractive-index change of the medium. The function $R(x)$ characterizes the nonlocal response of the medium and is assumed to be real and symmetric.

The nonlocal term $\Delta n(I)$ in Eq. (1) represents a general phenomenological model for self-defocusing Kerr-like media, in which the change in the refractive index induced by an optical beam involves a transport process. This may include diffusion of molecules or atoms in atomic vapors[12] or thermal effects in plasma.[13] A nonlocal response in the form of Eq. (1) appears naturally as a result of many-body interaction processes in the description of Bose–Einstein condensates.[14] It was shown recently that such a nonlocal nonlinearity prevents the collapse of multidimensional beams and supports the formation of bright solitons.[15–17]

0146-9592/04/030286-03$15.00/0

February 1, 2004 / Vol. 29, No. 3 / OPTICS LETTERS 287

Without loss of generality,[18,19] we consider the normalized response function $R(x) = (2\sigma)^{-1}\exp(-|x|/\sigma)$. This form allows us to write Eq. (1) as two coupled equations:

$$i\partial_z u + \partial_x{}^2 u + \Delta n u = 0, \tag{2}$$

$$\Delta n - \sigma^2 \partial_x{}^2 \Delta n = -|u|^2, \tag{3}$$

where Eq. (3) is the diffusion equation for a defocusing material. In this context the degree of nonlocality σ is then the diffusion parameter. In particular, for $\sigma \to 0$, model (1) approaches the local Kerr nonlinearity.

Let us focus on fundamental dark solitons $u(x,z) = u(x)\exp(i\lambda z)$, where the real profile $u(x)$ has zero center amplitude, $u(0) = 0$, and a π phase jump at the center, and where λ is a propagation constant. It was shown recently[20–22] that Eqs. (2) and (3) written for these stationary dark solitons are identical to the equations describing spatial solitons in quadratic nonlinear [or $\chi^{(2)}$] materials. The $\chi^{(2)}$ system predicts[23] the existence of stationary dark solitons with monotonic tails for $\sigma < 1/\sqrt{8}$ and nonmonotonic tails for $\sigma > 1/\sqrt{8}$. This implies that bound states of two or more dark solitons can be formed in sufficiently nonlocal materials with $\sigma > 1/\sqrt{8}$.

In Fig. 1 we show a numerically found dark soliton solution and the corresponding two-soliton bound state for $\sigma = 4$. The dashed curve shows the soliton-induced waveguide $(1 + \Delta n)$ in which the soliton is guided.

It is important to note that, although the profiles of stationary nonlocal spatial dark solitons and their bound states are equivalent to those of the $\chi^{(2)}$ system, the $\chi^{(2)}$ dark soliton bound states are unstable and break up when propagating, whereas the corresponding nonlocal bound states are stable, robust entities. We demonstrate the stability by numerical integration of Eq. (1) with the exact numerically found solution as the initial condition. Our simulations confirm stable propagation of nonlocal dark solitons and their bound states over tens of diffraction lengths, as in the example shown in Fig. 2.

For a better verification of stability we used the same initial condition but now embedded in a broad Gaussian beam, as in typical experiments. The propagation of this structure is shown in Fig. 2(b). The solitons remain bounded even though the background beam experiences strong deformation as a result of self-defocusing. As the intensity of the background beam decreases, the solitons adiabatically follow, adjusting their widths and mutual separation.

The ability of nonlocal dark solitons to form stable bound states is a direct consequence of the long-range attraction induced by the nonlocality. This effect may be explained with the self-guiding concept. In a local defocusing Kerr medium the refractive-index distribution corresponding to two dark solitons always has the form of two waveguides separated by a region of lower refractive index that acts as a potential barrier. This potential barrier leads to repulsion of the solitons. In the presence of a sufficiently strong nonlocality, for which the width of the response function (σ) is comparable to or larger than the separation between the solitons, the convolution integral in Eq. (1) is able to even out this central dip completely and create a single broad waveguide (see Fig. 1) that traps the solitons and enables them to form a bound state.

Dark solitons are generated experimentally by use of odd or even boundary conditions.[7,8] In the first case a broad laser beam passes through a phase mask with a single phase jump, leading to formation of an odd number of dark solitons. In the second case the beam passes through an amplitude mask (a thin wire) that imposes a dark notch on the beam and excites an even number of dark solitons with opposite transverse velocities.[24]

In the simulations shown in Figs. 3(a) and 3(b) the solitons are created by imposing two opposite phase jumps in a cw background. In Fig. 3(a) the degree of nonlocality $\sigma = 2$ is fixed, while the initial separation x_0 between phase jumps (and thus the solitons) decreases from left to right. For distant solitons the interaction is weak and repulsive, and their separation gradually increases. However, when the solitons

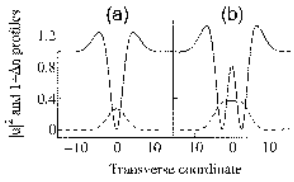

Fig. 1. Intensity profile $|u(x)|^2$ (solid curve) and induced waveguide structure $1 + \Delta n(x)$ (dashed curve) of (a) a single nonlocal dark soliton and (b) a bound state for $\lambda = 1$. The degree of nonlocality is $\sigma = 4$.

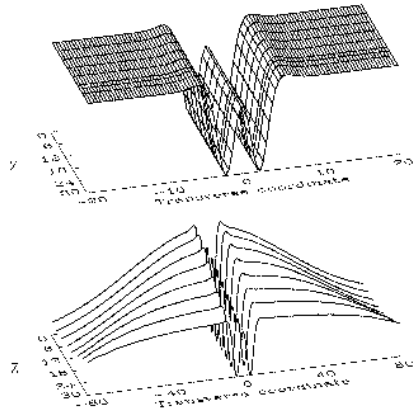

Fig. 2. Evolution of the intensity profile of a bound state of two nonlocal dark solitons for $\sigma = 1$ and $\lambda = 1$ on (top) a cw background and (bottom) a Gaussian background.

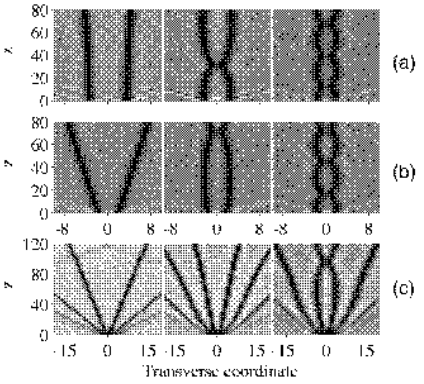

Fig. 3. Dark nonlocal solitons formed by (a), (b) phase or (c) intensity modulation of a cw background. In (a) the phase jump is π and the degree of nonlocality is $\sigma = 2$, and the initial soliton separation is $x_0 = 5.5, 4, 2.5$ from left to right. In (b) the phase jump is 0.95π and $x_0 = 2.5$, and $\sigma = 0.1, 1, 2$ from left to right. In (c) the width of the intensity gap is 7.5, and $\sigma = 0.1, 3, 6$ from left to right.

are brought closer the nonlocality-induced attraction becomes strong enough to overcome the repulsion and force the solitons to collide. For even smaller initial separation the solitons trap each other in an oscillatory transversal motion.

In Fig. 3(b) σ increases from left to right, while $x_0 = 2.5$ is fixed. For $\sigma = 0.1$ the nonlocality is too weak to affect the repulsive interaction of dark solitons, so they separate. As the degree of nonlocality increases, the effective range of attraction expands until it overcomes the repulsion. For a strong nonlocality the solitons are again mutually trapped and propagate together as a bound state exhibiting transversal oscillations.

Figure 3(c) illustrates the interaction of solitons created by a narrow gap in the incident cw wave front. Here the width of the gap is constant while the degree of nonlocality increases from left to right. For small σ the inherent repulsive force dominates and the solitons separate. As σ increases, the nonlocal attraction becomes stronger and the outward motion is slowed down. A strong nonlocality again leads to their mutual trapping.

In conclusion, we have investigated the interaction of dark solitons in Kerr-like nonlocal nonlinear media. We have shown that unlike local dark solitons, which repel, nonlocal dark solitons exhibit strong long-range attraction, which permits formation of stable bound states. We also demonstrated numerically that bound states of dark solitons can be created dynamically in sufficiently nonlocal materials.

This research was supported by the Danish Technical Research Council (grant 26-00-0355) and the Australian Research Council. W. Królikowski's e-mail address is wzk111@rsphysse.anu.edu.au.

References

1. Y. S. Kivshar and G. P. Agrawal, *Optical Solitons: from Fibers to Photonic Crystals* (Academic, San Diego, Calif., 2003), p. 560.
2. G. I. Stegeman and M. Segev, Science **286,** 1518 (1999).
3. Y. S. Kivshar and B. Luther-Davies, Phys. Rep. **298,** 81 (1998), and references therein.
4. K. J. Blow and N. Doran, Phys. Lett. A **107,** 55 (1985).
5. W. Zhao and E. Bourkoff, Opt. Lett. **14,** 1371 (1989).
6. D. Foursa and P. Emplit, Phys. Rev. Lett. **77,** 4011 (1996).
7. G. Swartzlander, D. R. Andersen, J. J. Regan, H. Yin, and A. E. Kaplan, Phys. Rev. Lett. **66,** 1583 (1991).
8. S. R. Skinner, G. R. Allan, D. R. Andersen, and A. L. Smirl, IEEE J. Quantum Electron. **27,** 2211 (1991).
9. B. Luther-Davies and Y. Xiaoping, Opt. Lett. **17,** 1755 (1992).
10. V. V. Afanasjev, P. L. Chu, and B. A. Malomed, Phys. Rev. E **57,** 1088 (1998).
11. E. A. Ostrovskaya, Y. S. Kivshar, Z. Chen, and M. Segev, Opt. Lett. **24,** 327 (1999).
12. D. Suter and T. Blasberg, Phys. Rev. A **48,** 4583 (1993).
13. A. G. Litvak, JETP Lett. **4,** 230 (1966).
14. A. Parola, L. Salasnich, and L. Reatto, Phys. Rev. A **57,** R3180 (1998).
15. O. Bang, W. Królikowski, J. Wyller, and J. J. Rasmussen, Phys. Rev. E **66,** 046619 (2002).
16. A. W. Snyder and D. J. Mitchell, Science **276,** 1538 (1997).
17. W. Królikowski and O. Bang, Phys. Rev. E **63,** 016610 (2001).
18. J. Wyller, W. Królikowski, O. Bang, and J. J. Rasmussen, Phys. Rev. E **66,** 066615 (2002).
19. W. Królikowski, O. Bang, J. J. Rasmussen, and J. Wyller, Phys. Rev. E **64,** 016612 (2001).
20. I. V. Shadrivov and A. A. Zharov, J. Opt. Soc. Am. B **19,** 596 (2002).
21. N. I. Nikolov, D. Neshev, O. Bang, and W. Krolikowski, Phys. Rev. E **68,** 36614 (2003).
22. C. Conti, M. Peccianti, and G. Assanto, Phys. Rev. Lett. **91,** 073901 (2003).
23. A. V. Buryak, P. Di. Trapani, D. V. Skyrabin, and S. Trillo, Phys. Rep. **370,** 63 (2002).
24. V. E. Zakharov and A. B. Shabat, Sov. Phys. JETP **37,** 823 (1973).

Appendix D

Modelling of SC Generation in highly nonlinear silica PCFs

Nikola I. Nikolov, Thorkild Sørensen, Ole Bang, Anders Bjarklev, and Jens Juul Rasmussen, Modelling of Supercontinuum Generation in highly nonlinear silica Photonic Crystal Fibers: Science and Applications" to be published in the series "Optical and Fiber Communications Reports", Ed. Anders Bjarklev (Springer-Verlag New York).

Modelling of Supercontinuum Generation in highly nonlinear silica Photonic Crystal Fibres

Nikola I. Nikolov[1,2], Ole Bang[1,3], Anders Bjarklev[3], Thorkild Sørensen[3], and Jens Juul Rasmussen[2]

[1]Informatics and Mathematical Modelling, Technical University of Denmark, DK-2800 Kongens Lyngby, Denmark
phone: (+45) 4525 3079, fax: (+45) 4593 1235, email: nin@imm.dtu.dk
[2]Risø National Laboratory, Optics and Fluid Dynamics Department, OFD-128 P.O. Box 49, DK-4000 Roskilde, Denmark
[3]Research Center COM, Technical University of Denmark, DK-2800 Kongens Lyngby, Denmark

Summary. We present a detailed explanation of the modelling of supercontinuum generation in highly nonlinear silica photonic crystal fibres with low-power picosecond pulses. Due to the strong nonlinearity and necessary broad-band description, the model takes into account effects such as self-phase-modulation, cross-phase-modulation, four-wave-mixing, stimulated Raman scattering, linear loss, birefringence, and up to 7th order dispersion. Variations in the fibre parameters along the length of the fibre are described as random fluctuations of the dispersion coefficients. Direct degenerate four-wave-mixing spectral components might have no contribution to the continuum spectra due to either big frequency shift and/or narrow gain band-width. When the dispersion is properly modified, optimum values for the Stokes frequency shift and the gain band-width will provide stable generation of the four-wave-mixing side bands. The numerical solution of our model shows, broadenning of the spectral component around the pump and the direct degenerate four-wave-mixing Stokes and anti-Stokes components and their finally merging. This leads to formation of an ultrabroad and independent on fiber parameter fluctuations supercontinuum spectra.

1 Introduction

Optical fibers are two dimensional dielectric waveguides, which are modelled as arbitrarily long in the propagation dimension. In optics, long propagation lenghts are usefull for telecommunication. However, long propagation lengths also give rise to high nonlinearities, and the opticalfibres may be designed to either minimize such effects or enhance them, and PCFs are especially suitable for this. The invention of the photonic crystal fibers (PCFs) [1, 2, 3, 4, 5], revolutionized the optical fiber technology. PCFs are optical fibers with wavelength-scale transverse structure of air and silica regions. Many different PCF structures have been considered both theoretically and experimentally. The transverse structure determines the mechanism of guidance and therefor the dispersion and nonlinear properties of the PCF. According to the mechanism of guiding of light PCFs are divided in two main classes. The band-gap

PCFs, guide light only over a limited range of wavelengths that correspond to the band-gap of the cladding material. The effective-index PCFs, guide light over the whole optical spectrum, but with physical limitations of the guiding comparable to those used for standard optical fibers. The proper structure design of the effective index guiding PCFs, can lead to single-mode operation for all the wavelengths of interest [1, 2]. The highly nonlinear PCFs are effectively index-guiding fibers, with a significantly reduced core size (having a diameter around $\approx 1\mu m$). Thus, a significant increase in the nonlinearity is possible without the addition of doping elements. The highly nonlinear PCFs were shown to be useful in various applications targeting effective nonlinear processes. However, due to their unique dispersion properties, the process of supercontinuum (SC) generation became their fundamental application.

SC generation is a combined effect of several nonlinear process in different regimes leading to a dramatic spectral broadening of intense light pulses [6]. The various applications of the SC sources in laser spectroscopy, optical tomography, remote sensing, wavelength division multiplexing in optical communications and many others, have stimulated numerous experimental and theoretical investigations for better understanding and control of this process. The research in the SC field aimed at the generation of broader and flatter SC spectras in the whole optical domain, while preserving high coherence properties by simpler experimental techniques, i.e., using low-power and low-cost light sources.

Formation of a 200-THz SC spectrum of light in bulk glass has been first observed in 1970 [7, 8]. Since then, generation of a SC spectra has been obtained in various nonlinear bulk media and optical fibers. The different nonlinear media and optical pulses used for obtaining SC, rely on different physical mechanisms and thus different theoretical models are required for the correct description of the process of SC generation.

The experiments in bulk materials required extremely high peak powers ($>$ 10MW). New techniques based on the use of optical fibers as a nonlinear medium for SC generation allowed lower peak powers to be used due to the long interaction length and high effective nonlinearity [9, 10, 11, 12]. However, the necessity to operate near the wavelength for zero group velocity dispersion restricted the SC generation to the spectral region around and above 1.3μm. The use of dispersion-flattened or dispersion-decreasing fibers as nonlinear media for SC generation resulted in a flat SC spanning 1400-1700nm [13, 14] and 1450-1650nm [15], respectively. The spectrum was still far from the visible wavelengths.

PCFs and tapered fibers have similar dispersion and nonlinearity characteristics, and they have the advantage that their dispersion may be significantly modified by a proper design of the cladding structure [2, 16, 17, 18], or by changing the degree of tapering [19], respectively.

Using kilowatt-peakpower femtosecond pulses, a SC spanning 400-1500nm has been generated in a PCF [20] and in a tapered fiber [19]. The broad SC

has been explained to be a result of self phase modulation (SPM) and direct degenerate four-wave-mixing (FWM) [21]. Later, it was also reported that a SC spanning from 380 to 1600nm is obtainable using 200fs pulses with an energy less than 5nJ [22]. The theoretical explanation includes nonlinear processes such as fission of higher order solitons [22, 23, 24].

Further, high power femtosecond lasers are not needed - it was shown that SC generation is achievable with low-power picosecond [12, 10] and even nanosecond [25] pulses. Coen *et al.* demonstrated a broad SC in a PCF with picosecond pulses and sub-kilowatt peakpower. It was shown by numerical modelling that the primary mechanism for the SC generation in his experiments was a combined effect of stimulated Raman scattering (SRS) and parametric FWM [12].

Using 200 fs high-power pulses and a 1cm long tapered fiber, Gusakov has shown that direct degenerate FWM can lead to ultra wide spectral broadening and pulse compression [21]. We consider, how the direct degenerate FWM can significantly improve the efficiency of SC generation with sub-kilowatt picosecond pulses in PCFs, and go one step further by optimizing the effect through engineering of the dispersion properties of the PCF. We show that by a proper design of the dispersion profile, the direct degenerate FWM Stokes and anti-Stokes lines can be shifted closer to the pump, thereby allowing them to broaden and merge with the pump to form an ultra broad SC. This significantly improves the efficiency of the SC generation, since the power in the Stokes and anti-Stokes lines is no longer lost.

Improvement of the SC generation by enhancing the role of parametric processes, such as direct degenerate FWM, relies on the possibility to fabricate PCFs with a proper dispersion. It is theoretically predicted that by varying the hole size and pitch in a triangular silica-air PCF, an ultra flattened dispersion is achievable [16, 17]. Flat dispersion profiles with slope within $0.017 ps/(nm^2 \cdot km)$ have been obtained [28]. Recently, a new fiber structure with a three-fold symmetry has been shown to enable unprecedented dispersion control, while maintaining low loss and a high nonlinear coefficient [29]. In this contribution, we discuss how by varying the core diameter of a cob-web PCFs [30] it is possible to obtain dispersion profiles similar to those predicted to give the most efficient SC generation.

External perturbations and different types of imperfections lead to fluctuations of the fiber parameters along the length of the fiber. Fluctuations in fiber birefringence [31, 32], dispersion [33, 34, 35], and nonlinearity [36, 37] has been investigated to understand their influence on different regimes of light propagation. As parametric processes require phase matching, the effectiveness of the FWM could be strongly influenced by random fluctuations of the dispersion. Indeed Coen *et.al.* in their PCF experiments with low-power picosecond pump pulses at 647nm [12, 10] and nanosecond pump pulses at 532nm [25] explains the absence of frequencies generated by direct degenerate

FWM from the pump, by the large frequency shift and the violation of the required phase-matching condition due to fiber irregularities.

We have analyzed the influence of a random change of the dispersion coefficients along the fiber on the process of SC generation and find that the generation and merging of the direct degenerate FWM Stokes and anti-Stokes waves with the pump could be robust enough to survive fiber imperfections, and thus a significant improvement of the process of SC generation should indeed be possible in real PCFs.

2 Physical model of SCG in PCFs

The model used to describe the SC generation with picosecond light pulses is based on the generalized nonlinear Schrödinger equation (GNLSE) [38]. This equation is derived without the assumptions of a "slowly varying amplitude" approximation. Further, the direction of propagation is assumed to be determined, so back reflecting waves and their contribution to the nonlinearity are neglected. This determines the spectral range of validity to 1/3 of the pump frequency ω_0 [38]. These approximations are generally valid for all cases of light propagation, when such broad spectrum is considered for propagation of extremely short pulses, SC generation in bulk materials and optical fibers. In all cases of SC generation, the major nonlinear contributions comes from the $\chi^{(3)}$ nonlinear processes. Self focussing and plasma formation are the dominant nonlinear processes leading to SC generation in bulk (solid, liquid or gaseous) nonlinear optical materials. When the nonlinear media used for the SC generation is an optical fiber, the power of the optical wave is usually below the threshold for self-focussing ($I_p << \lambda_0^2/(\pi n_2)$) [39] and single mode operation is assumed. Thus diffraction and plasma formation terms are neglected. Further in our model, the dispersion of the nonlinearity $\chi^{(3)}(\omega)$, the frequency dependance of the effective area, $A_{eff}(\omega)$ and the loss $\alpha(\omega)$ are neglected [12, 23, 26, 25, 27]. Usually the highly nonlinear PCFs have three-fold symmetry structure, but fiber imperfections may induce weak birefringence. Thus, we model the weak birefringence observed in the highly nonlinear PCFs by considering x- and y-polarization components of the field, while assuming the same dispersion and effective area for the two principle axes. The system of equations Eq. (1), which model the SCG in a weakly birefringent highly nonlinear PCFs consists of a two coupled GNLSEs describing the propagation of the two polrization components.

$$\frac{\partial A_j}{\partial z} = -\mu A_j + i(j-1)\delta\beta A_j + (-1)^j \frac{\Delta}{2}\frac{\partial A_j}{\partial \tau} \qquad (1)$$
$$+\frac{i}{2}\sum_{k=2}^{7} i^k \frac{\beta_k}{k!}\frac{\partial^k A_j}{\partial \tau^k} + i\gamma\left(1+\frac{i}{\omega_p}\frac{\partial}{\partial \tau}\right)\Big\{$$

$$A_j f_R \int h_R(\tau - s)\left(|A_j(s)|^2 + |A_{3-j}(s)|^2\right) ds$$
$$+(1-f_R)\left[\left(|A_j|^2 + \frac{2}{3}|A_{3-j}|^2\right) A_j + \frac{1}{3} A_j^* A_{3-j}^2\right]\Bigg\}.$$

Here the complex fields $A_j = A_j(t,z)$ with j=1,2 are given by $A_1 = E_x$ and $A_2 = E_y \exp(i\delta\beta z)$, where E_x and E_y are the envelopes of the real linearly polarized x- and y-components. The time $\tau = t - z/\overline{v}$ is in a reference frame moving with the average group velocity $\overline{v}^{-1} = (v_x^{-1} + v_y^{-1})/2$, z is the propagation coordinate along the fiber, μ is the fiber loss, $\delta\beta = \beta_x - \beta_y = \omega_0 \delta n/c$ is the phase mismatch due to birefringence $\delta n = n_x - n_y$, and $\Delta = (v_x^{-1} - v_y^{-1})$ is the group velocity mismatch between the two polarization axes. The propagation constant $\beta(\omega)$ is expanded to 8^{th} order around the pump frequency ω_p with coefficients β_k keeping β_{2-7} the same for x- and y-linearly polarized components, γ is the effective nonlinearity, f_R is the fractional contribution of the Raman effect, and, finally, * denotes complex conjugation. Theoretically the Raman effect is modelled by a convolution integral on the applied optical field and a delayed time-responce function $h_R(t)$, which exact form can be determined by taking a Fourier transform of the measured Raman gain.

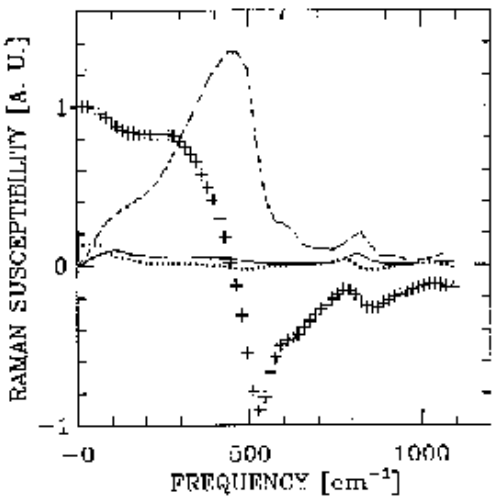

Fig. 1. Reproduced from 1 with permission from the Optical Society of America. The solid curve and the dotted curve shows the imaginary and the real parts of the orthogonal component of the Raman susceptibility as function of frequency, respectively. The crosses and the dashed curve represent, the imaginary and the real parts of the parallel component of the Raman susceptibility, respectively.

This model accounts for self-phase-modulation (SPM), cross-phase-modulation (CPM), self-steepening, FWM, and stimulated Raman scattering (SRS). As seen from Fig.1 in [40], and reproduced here as Fig.1, the orthogonal component of the Raman susceptibility h_R is generally negligible in the frequency ranges considered here, so we include only the parallel component. Further, we approximate the Raman susceptibility by the expression [41]:

$$h_R(t) = \frac{\tau_1^2 + \tau_2^2}{\tau_1 \tau_2^2} \exp(-t/\tau_2) \sin(t/\tau_1), \tag{2}$$

where τ_1=12.2fs and τ_2=32fs. Furthermore, f_R=0.18 is estimated from the known numerical value of the peak Raman gain [41].

The phase-mismatch for degenerate FWM of two photons at the pump frequency is: $\Delta\beta = \beta_s + \beta_{as} - 2\beta_p + 2\gamma I_p$ [41], where I_p is the peak power, and, $\beta_{s,as}$ and β_p are the propagation constants corresponding to the Stokes, anti-Stokes and the pump frequencies. For the degenerate FWM, the Stokes and anti-Stokes spectral components have frequency shifts with opposite signs, but equal value: $\Omega = \omega_p - \omega_s = \omega_p - \omega_{as}$. Thus, the expansions of $\beta_{s,as}$ around ω_p, will cancel their odd order coefficients, and the frequency dependance of the phase mismatch will be:

$$\Delta\beta = 2\left[\Omega^2 \frac{\beta_2}{2!} + \Omega^4 \frac{\beta_4}{4!} + \Omega^6 \frac{\beta_6}{6!} + \gamma(1 - f_R) I_p\right], \tag{3}$$

where $\Omega = \omega_p - \omega_s = \omega_{as} - \omega_p$. The gain g of the direct degenerate FWM [10, 41] is:

$$g = \left\{\left[(1 - f_R)\gamma I\right]^2 - (\Delta\beta/2)^2\right\}^{1/2}, \tag{4}$$

where I is the power of the frequency component around which the degenerate FWM process takes place.

3 Numerical Method for Modelling of SCG

We solve the GNLSE, using a modification of the standard second order split-step Fourier method. Thus, the linear and nonlinear parts are separated [41]. Then Eq.1 can be written in a matrix form:

$$\frac{\partial}{\partial z}\boldsymbol{A} = \left(\hat{L} + \hat{N}\right) \cdot \boldsymbol{A}, \tag{5}$$

The electric field vector $\boldsymbol{A}$ of the optical wave has two complex elements corresponding to the two linearly polarized components of the electrical field. The linear operator is represented by the diagonal 2x2 matrix $\hat{L}$ with elements:

$$L_{1,1} = i\mu - \frac{\Delta}{2}\frac{\partial}{\partial\tau} - \frac{i}{2}\sum\frac{\beta_k}{k!}\frac{\partial^k}{\partial\tau^k}$$
$$L_{2,2} = i\mu + \frac{\Delta}{2}\frac{\partial}{\partial\tau} - \frac{i}{2}\sum\frac{\beta_k}{k!}\frac{\partial^k}{\partial\tau^k} + i\delta\beta \tag{6}$$

The nonlinear operator is represented by the 2x2 matrix $\tilde{N}$ with elements

$$N_{j,\,j} = (1 - f_R)\left(|A_j|^2 + \frac{2}{3}|A_{3-j}|^2\right) + f_R\int h_R(\tau - s)\left[|A_j(s)|^2 + |A_{3-j}(s)|^2\right]ds$$
$$N_{j,3-j} = \frac{1 - f_R}{3}A_j^* A_{3-j} \tag{7}$$

The linear operator is actually represented by a constant matrix containing explicitly the propagation coordinate z. Thus, if the split-step integration procedure starts with the linear operator, we will need two constant matrixes, one for the full propagation step Δz and one for the half. We chose to start the integration with the nonlinear operator. The linear operator $\tilde{L}$ is calculated in the Fourier space. As was previously shown [12, 38], the numerical integration of the nonlinear part can be done by a second-order Runge-Kutta method and the convolution theorem, while the derivative in front the nonlinear term is treated as a perturbation. However, in this case the conservation of the photon number is already violated by 5% after approximately 60000 integration steps. We improve the accuracy of the numerical integration by solving the nonlinear part with a forth order Runge-Kutta method and the convolution theorem. The essential difference is that the time derivative of the nonlinear part is exactly calculated by Fourier transform fourth and back. In this way, the reliable propagation distance at which the photon number is conserved within the critical 5% is increased to 86000 integration steps.

The convenience of using a single equation for a broad spectral range, comes on the expense of the higher resolution required for the numerical modelling. The transverse step must be chosen to correctly sample the carrier wave, not the envelope. To get the highest acceptable resolution, we use 2^{17} points in a time window of $T = 236$ps, giving the wavelength window $(405 - 1613\text{nm})$. This garantees us that all the frequency components expected to be generated are, in the simulation window. As noted, here the time derivative of the nonlinear term is exactly calculated, thus, we do not increase the resolution in the propagation step and keep it the same as in [12, 27] $\Delta z = 43\mu$m. Consequently, the critical violation of the photon number up to 5% determines the longest length of a PCF to be $L = 3.7$m, in a realiable simulation.

An initial random phase noise seeding of one photon per mode (approximately 10^{-8} percent of the pulse peak power) is included as in [12, 27]. All the presented spectra have been smoothed over 32 points.

4 Dispersion properties of highly nonlinear silica PCFs

The special transverse structure of the highly nonlinear silica PCFs gives rise to their specific dispersion properties in combination with single-mode operation over a wide spectral range, shift of the zero-dispersion wavelength into the visible region and better dispersion control. These extraordinary properties originate from the large index difference between the micron-size pure silica core and the cladding, composed predominantly of voids filled with air.

We consider the same PCF and use the same numerical and experimental data as in [12], kindly provided by S. Coen. We pump along the slow axis with 30ps standard soliton shape $A(\tau) = A_0 sech(\tau/\tau_0)$ pulses of $|A_0|^2 = I_p =$ 400W peak power and a pump wavelength $\lambda_p = 647$nm. The PCF has a core area $A_{core} = 1.94\mu m^2$, birefringence $\delta n = 1.9 \times 10^{-6}$, and the nonlinearity is given by $n_2 = 3 \times 10^{-20} m^2/W$.

In our initial numerical analysis we consider six different artificial dispersion profiles, for which β_{2-7} are given in Table 1, where case d1 corresponds to the PCF used in [12]. Note that cases d4+d6 and d5 have two and three sets of Stokes and anti-Stokes waves, respectively.

Here, we are interested in studying the separate effect of different dispersion profiles (i.e., different values of β_{2-7}). We, therefore, keep all other fiber and pulse parameters constant and neglect the frequency dependence of the effective area A_{eff} and the loss μ. Thus, we assume a uniform loss of $\mu = 0.1$dB/m and approximate A_{eff} with the core area, so that $\gamma = 2n_2/(\lambda_p A_{core}) = 0.15(Wm)^{-1}$.

As will be shown later, the FWM nonlinear process is very important for the efficient SC generation using low-power ps and ns input pulses [27]. Thus, we here discuss, how to receive the most suitable FWM gain spectrum for the efficient SC generation by changing the dispersion profile. As seen in Eqs. (3) and (4), the even numbered dispersion coefficients $\beta_{2,4,6,...}$ are included only in the expression for the FWM gain. Thus, for simplicity, we do not change the odd numbered dispersion coefficients $\beta_{3,5,7,...}$. Next, we consider six dispersion profiles $d1 - d6$ with the corresponding coefficients of the Taylor expansion given in Tabel 1 and dispersion profiles shown in Fig. 2. The only information obtainable from just knowing the dispersion coefficients is whether the pump wavelength is in the anomalous or normal dispersion regime, i.e., whether the process of higher-order soliton splitting is expected to contribute to the SC generation. To analyze the contribution of the parametric processes, it is necessary to determine the phase-mismatch and the gain spectrum. As in the SC generation experiments, usually a single wavelength source is used in one

Table 1. Dispersion coefficients β_2 [ps^2/km], β_4 [10^{-5}ps^4/km] and β_6 [10^{-10}ps^6/km] for dispersion profiles d1-d6, with corresponding dispersion at the pump wavelength $D(\lambda_p)$ [ps/(nm · km)], zero dispersion wavelength λ_z [nm] and Stokes λ_s [nm] and anti-Stokes λ_{as} [nm] wavelengths. Fixed coefficients: $\beta_3 = 5.1 \times 10^{-2}$ps^3/km, $\beta_5 = 1.2 \times 10^{-7}$ps^5/km and $\beta_7 = 1.2 \times 10^{-13}$ps^7/km.

case	β_2	β_4	β_6	λ_z	$D(\lambda_p)$	λ_s	λ_{as}
d1	7.0	-4.9	-1.8	677	-31.6	1108	457
d2	14	-34.4	-0.04	697	-62.3	852	522
d3	1.0	-2.5	-3.3	652	-4.5	849	523
d4	-0.28	0.05	0.29	647	1.3	1083	461
						822	534
d5	-1.01	2.14	-2.84	643	4.54	1096	459
						911	562
						735	578
d6	-1.3	-2.6	58.8	641	5.9	803	628
						713	593

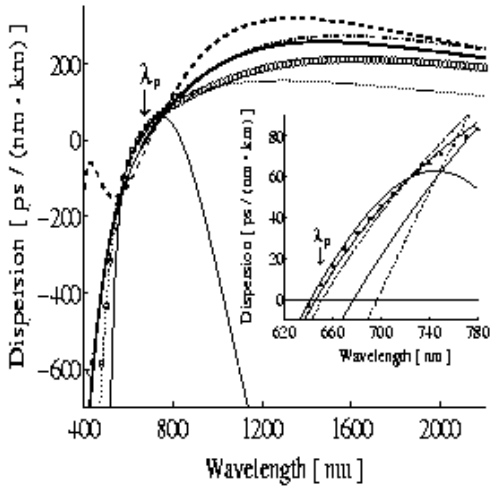

Fig. 2. Dispersion profile d1 (thick solid line), d2 (dashed line), d3 (dash-dotted line), d4 (dotted line), d5 (circles), and d6 (thin solid line).

of the principle polarizations, we consider only the FWM parametric process. The phase mismatch and gain curves for pump wavelength 647nm are shown in Fig.3 and Fig.4. Intuitively, it should be expected that the broader the FWM gain, the broader the SC spectra would be. However, in the expression for the gain Eq.4, the pump depletion due to loss and generation of new frequency components is not taken into account and it is not possible to conclude directly from the FWM gain curves, which dispersion profile will

produce SC spectra with optimal width and quality. Further, as will be shown by the SC simulation results in Section 5 cascaded parametric processes may further improve the efficiency of SC generation.

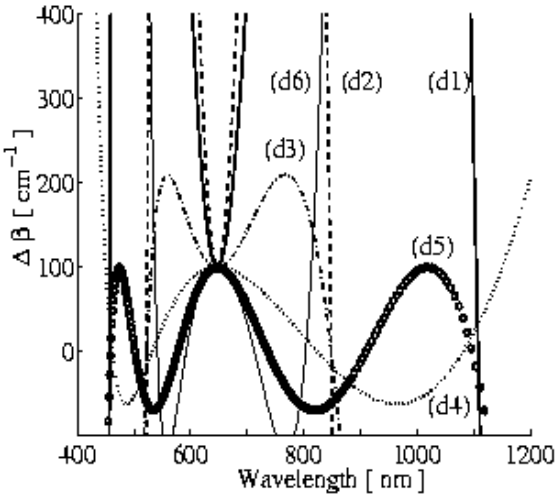

Fig. 3. Phase mismatch $\Delta\beta(\lambda)$ for dispersion profile d1 (thick solid line), d2 (dashed line), d3 (dash-dotted line), d4 (dotted line), d5 (circles), and d6 (thin solid line).

In additon, all kind of impurities and PCF imperfections could lead to distortion of the phase mismatch condition Eq. (3), hence reducing the FWM gain, as it was previously reported [12, 27]. Thus, the expected spectral bands due to FWM, have not been seen in SC generation experiments [12]. Here we also analyze the influence on the FWM gain of the random fluctuation of the dispersion parameters along the fiber.

It has indeed been shown experimentally that a variation of the zero-dispersion wavelength λ_z of the order of 0.1nm over the entire length of a dispersion shifted fiber could significantly reduce the FWM efficiency [33]. This reduction in the FWM efficiency was later explained theoretically from expressions for the average parametric gain, phase-conjugation efficiency, and gain band-width [34]. It has also been shown that in order to control the dispersion within $\pm$1ps/(nm·km), the allowable deviation of the core radius in W-type dispersion-flattened fibers is 0.04μm, while for other types of dispersion-flattened fibers, the allowable core radius deviation is 0.1μm [35]. As PCFs have larger index steps and more complex structures, strong fluctuation of the fiber dispersion could also be expected. However, to our knowledge a thorough study of the influence of fluctuations of the PCF pa-

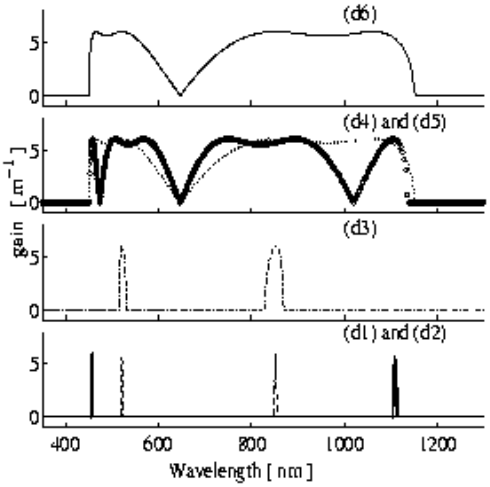

Fig. 4. Degenerate FWM gain $g(\lambda)$ for dispersion profile d1 (thick solid line), d2 (dashed line), d3 (dash-dotted line), d4 (dotted line), d5 (circles), and d6 (thin solid line).

rameters (e.g., core size and pitch) on the variation of the dispersion profile (i.e., the dispersion coefficients β_{2-7}) is not available in literature.

For a newly developed highly nonlinear PCF with λ_z=1.55μm, it was recently shown that the variation of λ_z is only 6nm and the variation of the dispersion slope at λ_z, $D'_z = dD(\lambda_z)/d\lambda$, varies between -0.25 and -0.27 ps/(nm^2·km) over a 150m span [18]. Expanding the propagation constant to third order around the pump wavelength λ_p=647nm, the dispersion has the form

$$D(\lambda) = -\frac{2\pi c}{\lambda^2}\left[\beta_2 + 2\pi c\beta_3\left(\frac{1}{\lambda} - \frac{1}{\lambda_p}\right)\right]. \tag{8}$$

From this expression we find the dispersion coefficients

$$\beta_2 = \frac{\lambda_z^4 D'_z}{2\pi c}\left(\frac{1}{\lambda_p} - \frac{1}{\lambda_z}\right), \quad \beta_3 = \frac{\lambda_z^4 D'_z}{4\pi^2 c^2}, \tag{9}$$

which give the extreme β_2^{max}=7.51ps^2/km, β_2^{min} = 6.83ps^2/km, β_3^{max}=0.44ps^3/km, and β_3^{min}=0.40ps^3/km, and, thus, the relative variations $\langle\beta_2\rangle \simeq \langle\beta_3\rangle$=9.5%, where

$$\langle\beta_k\rangle \equiv \frac{\beta_k^{max} - \beta_k^{min}}{(\beta_k^{max} + \beta_k^{min})/2}, \qquad k = 1, 2. \tag{10}$$

Note that the relative variations of β_2 and β_3 are equal.

We model the effect of a fluctuating dispersion profile by imposing that $\delta\beta$, Δ, and all the dispersion coefficients β_{2-7} [see Eq. (1)] vary randomly along the fiber,

$$\delta\beta(z) = \delta\beta + \sigma_0(z), \quad \beta_{k,x}(z) = \beta_k + \sigma_{k,x}(z),$$
$$\Delta(z) = \Delta + \sigma_1(z), \quad \beta_{k,y}(z) = \beta_k + \sigma_{k,y}(z),$$

where k=2,..,7. The random fluctuation of the coefficients, represented by the σ-terms, is modelled as Gaussian distributed white noise with zero mean. To achieve the most severe case, we use different seeds for all terms. We have, thus, assumed that the fluctuations affect the dispersion in the two birefringent axes independently. With the results from Ref. [18] in mind, we assume that the strength (or variance) of the fluctuations is the same in all coefficients,

$$\frac{\langle\sigma_0^2(z)\rangle}{\delta\beta} = \frac{\langle\sigma_1^2(z)\rangle}{\Delta} = \frac{\langle\sigma_{k,x}^2(z)\rangle}{\beta_k} = \frac{\langle\sigma_{k,y}^2(z)\rangle}{\beta_k} = \rho, \tag{11}$$

and use the strength ρ=10%.

4.1 Obtaining dispersion profiles in cob-web PCFs

In Section 4 we have shown that the FWM gain spectrum can be engineered by a proper change of the even numbered dispersion coefficients $\beta_{2,4,6}$. In our analysis up to this point, we did not consider any practically realizable PCF structure that may provide the dispersion profiles d2-d6. PCFs with a cob-web transverse structure have three design parameters: pitch, wall thickness, and core diameter, that all influence the fiber dispersion [30]. In contrast the triangular PCF has only two design parameters: pitch and hole diameter. Using the MPB free software [42], we have, therefore, performed a full-vectorial plane-wave analysis of cob-web PCFs with different core diameters, keeping the pitch fixed at 8.5μm, and the wall thickness fixed at 130nm. The resulting dispersion profiles are shown in Fig. 5. As seen from the phase mismatch curves the direct degenerate Stokes and anti-Stokes wavelengths are closer to the pump wavelength when the core diameter is smaller. The cob-web PCF with core diameter 1450nm has a dispersion profile (cob3) and corresponding phase mismatch curve, which is very similar to the case d3.

5 Simulation Results of the Model for SCG in highly nonlinear silica PCFs

5.1 Propagation dynamics in the spectral domain

We first simulate SC generation using the same fiber as in [12], i.e., using the dispersion profile d1. Due to our large spectral window (405 − 1613nm), we see in Fig. 6 (left) the emergence of direct-degenerate FWM Stokes and anti-Stokes waves at the predicted wavelengths λ_s = 1100nm and λ_{as} = 458nm,

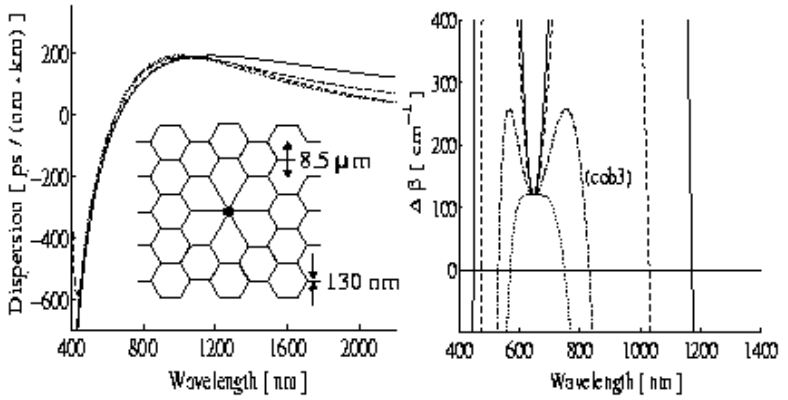

Fig. 5. Left: dispersion profiles for the cob-web PCF structures with pitch 8.5μm, wall thickness 130nm, and core diameter 1600nm (solid line), 1500nm (dashed line), 1450nm (dash-dotted line), and 1400nm (dotted line). Right: Corresponding phase mismatch curves.

for which the phase matching condition (3) is satisfied. From the standard expressions given in [41], we find the maximum direct degenerate FWM gain (g) to be twice the maximum SRS gain, which explains why the FWM Stokes and anti-Stokes components appear before the SRS components.

For a given peak power, the loss and temporal walk-off of the PCF gives the maximum distance L_{max} over which nonlinear processes, and thus the SC generation process, are efficient. From Fig. 6 (left) we see that after the FWM Stokes and anti-Stokes components are generated, they broaden in the same way as the central part of the spectrum around the pump. The merging of the spectral parts around λ_{as}, λ_p, and λ_s would create an ultra broad spectrum as observed in tapered fibers with high power femtosecond pulses [19, 21]. However, for high power femtosecond pulses, the SPM is the dominant mechanism that leads to broadening and merging of the Stokes and anti-Stokes lines with the pump. For low power picosecond pulses the Raman and parametric processes are dominant. Thus, in this particular case, the large frequency shift $\sim$ 193THz of the degenerate FWM sidebands and the narrow degenerate FWM gain bands $\sim$ 2THz prevent merging of the pump with the Stokes and anti-Stokes lines to happen within the maximum length L_{max}, i.e., before nonlinear effects become negligible. Indeed, it is seen from Fig.6, that the spectrum does not change significantly from 1m to 3.7m. The power transferred to the Stokes and anti-Stokes lines is in fact lost, i.e., the SC process is not very efficient. By increasing the peak power, it would be possible to achieve merging of the spectral parts around λ_{as}, λ_p, and λ_s. However, our aim is to keep the low peak power fixed and instead achieve this merging only by engineering the dispersion profile. Thus, we modify the dispersion profile

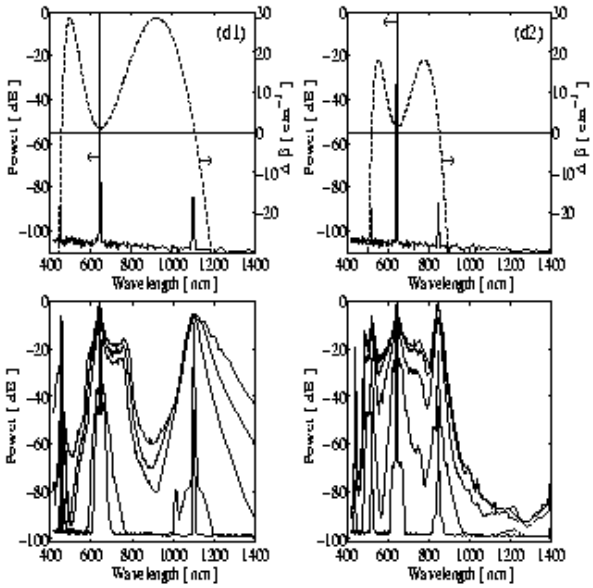

Fig. 6. Dispersion profiles d1 (left) and d2 (right). Top row: phase mismatch $\Delta\beta$ for direct degenerate FWM (dashed line) and spectrum at L=10cm (solid line). Bottom row: spectrum at L=20cm, 30cm, 1m, 2m, and 3.7m (down to up).

to adjust Eq. (3) to be fulfilled for wavelengths λ_s and λ_{as} closer to the pump $\lambda_p = 647$nm. We do so by modifying β_2, β_4, and β_6 as listed in Table 1. The phase-matching condition $\Delta\beta = 0$ then gives $\lambda_s \approx 850$nm and $\lambda_{as} \approx 522$nm for case d2-d3. In case d4-d6 additional Stokes and anti-Stokes waves exist. The dispersion profiles and phase-mismatch curves corresponding to the cases in Table 1 are shown in Fig. 2 and Fig. 3, respectively. It is important to note that the curves $\Delta\beta(\lambda)$ have different slope around λ_s and λ_{as} (see Fig. 3).

We first consider only a shift of the Stokes and anti-Stokes lines closer to the pump and the effect it has on the improvement of the SC generation. Thus, for the dispersion profile d2, the slope of the phase mismatch curve around $\lambda_s \approx 850$nm and $\lambda_{as} \approx 522$nm is kept the same as for case d1. It is seen from Fig. 6 (right) that such a shift of the direct degenerate FWM Stokes and anti-Stokes lines closer to the pump is not enough for a complete merging to take place. This can be explained by considering the direct degenerate FWM gain $g(\lambda)$ shown in Fig. 4. The broadening of the Stokes and anti-Stokes lines is strongly influenced by the bandwidth of $g(\lambda)$, which is mainly determined by the slope around $\Delta\beta = 0$, i.e., around λ_s and λ_{as}. The slope and thus the gain bandwidth is the same in case d1 and d2, which explains why the broadening appears to be unchanged.

One way to improve the SC spectrum is to shift the Stokes and anti-Stokes lines even closer to the pump, keeping the slope of the phase mismatch curve around them constant. However, this will not significantly improve the width of the SC spectrum as compared to case d1, because the narrow direct degenerate FWM gain bands will then be in the region, where a SC is already generated by Raman and FWM processes. Moreover, this will lead to even more unusual dispersion profiles than that for case d2 (see Fig. 2), which does not seem to be experimentally realistic. Instead, we fix λ_s and λ_{as}, while reducing the slope and, thus, increasing the gain bandwidth. For dispersion profile d3, the direct degenerate FWM gain bandwidth is thus increased to 16.5THz (see Fig. 4). This leads to broader Stokes and anti-Stokes lines in the initial stages of the SC generation and, finally, to their merging with the spectrum around the pump as seen from Fig. 7 (right). Thus a SC, which is flat within 10dB and extending from around 500nm to 900nm is formed after a propagation distance of $L = 2$m despite using low-power picosecond pulses. Moreover, the dispersion profile d3 is more realistic and may in fact be obtained in realizable PCF structures, such as the so-called cob-web PCF [30], as has been discussed in Section 4.1.

The SC process is, thus, much more efficient with dispersion profile d3 than with d1, since the power in the Stokes and anti-Stokes lines is not lost. However, the SC may be further improved by designing the dispersion such that the phase-mismatch $\Delta\beta(\lambda)$ has two or even three sets of Stokes and anti-Stokes lines, i.e. roots of the polynomial (3). The dispersion profiles d4 and d5 represent such cases with two and three sets of Stokes and anti-Stokes lines, respectively, around which the spectrum can broaden. From the corresponding gain curves in Fig. 4, we see that two gain bands actually overlap and form one broad gain band. The presence of extra Stokes and anti-Stokes lines and the broad gain band could make the SC generation more efficient, provided they do not deplete the pump so much that the central SC spectrum around the pump deteriorates. In Fig. 8, we show the SC generated in a PCF with dispersion profile d3 and cob3. As expected, the SC obtained with the cob3 profile is nearly identical to the SC obtained with the d3 dispersion profile. This allows us to conclude that the proposed method for improving the efficiency of the SC generation by a proper dispersion design can indeed be achieved in a real experiment. To provide further evidence of this, we investigate in the next section, how fiber irregularities, modelled as random fluctuations of the dispersion coefficients, influence the SC generation.

From Fig. 9 (left) we see that with the dispersion profile d4 the initial stage of the SC generation is indeed improved, with the spectrum at L=10cm mainly reflecting the gain profile seen in Fig. 4. However, the small dip in the gain curve around 950nm has a strong effect on the evolution of the spectrum, leaving a clear dip at 930nm in the final SC spectrum. Optimizing the position of the two Stokes lines can remove this dip and lead to an even broader SC spectrum than observed in Fig. 7 for one set of Stokes and anti-Stokes lines.

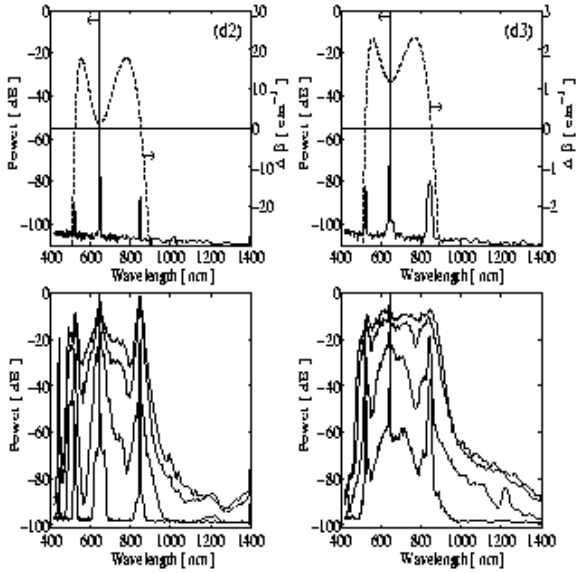

Fig. 7. Dispersion profiles d2 (left) and d3 (right). Top row: phase mismatch $\Delta\beta$ for direct degenerate FWM (dashed line) and the spectrum at L =10cm (solid line). Bottom row: spectrum at L=20cm, 30cm, 1m, and 2m (down to up).

Instead, we show in Fig. 9 (right) the evolution of the spectrum in a PCF with the dispersion profile d5, which has three sets of Stokes and anti-Stokes lines. The small dip in the gain curve around 800nm (see Fig. 4) is still reflected in the spectrum, but it is now less pronounced, and we obtain a final ultra-broad SC spectrum ranging from 450nm to 1250nm within the 20dB level. Of course the dispersion profile may be optimized further to remove the dip and make the SC spectrum more flat and even broader.

So far we have only considered the Stokes and anti-Stokes lines generated directly from the pump through degenerate FWM. However, so-called cascaded FWM processes also play an important role in the evolution of the spectrum, as discussed thoroughly in [12]. In particular, one can use these processes to obtain a broader SC. The dispersion profile d6 is designed to clearly illustrate this effect. It still implies two sets of Stokes and anti-Stokes lines, but now these are very close to the pump, within the regime of wavelengths covered by the central SC generated by the pump. Nevertheless we see in Fig. 10 (right) that additional lines are generated, around which the spectrum broadens, resulting in a final SC spectrum extending from 450nm to 1μm within 10dB. The line at 1030nm is generated by direct degenerate FWM from the Stokes wave at 720nm, and the line at 1060nm is generated by FWM between the Stokes wave at 720nm and the pump. Thus, these cas-

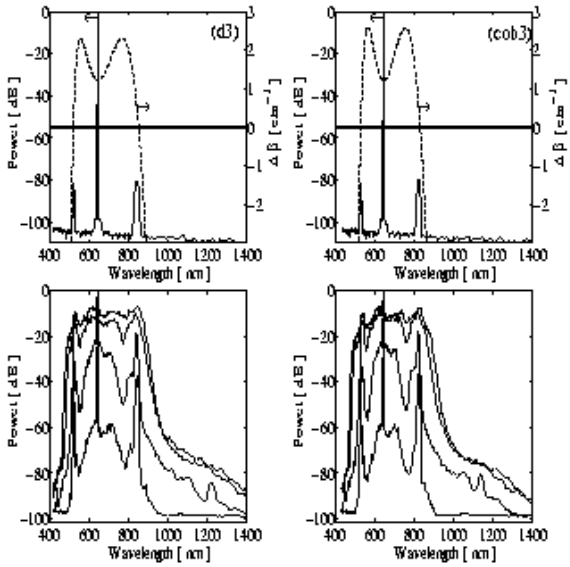

Fig. 8. Dispersion profiles d3 (left) and cob3 (right). Top row: phase mismatch $\Delta\beta$ for direct degenerate FWM (dashed line) and spectrum at L=10cm (solid line). Bottom row: spectrum at L=20cm, 30cm, 1m, 2m, and 3.7m (down to up).

caded parametric processes result in a spectrum, which is broader than what was obtained with the direct degenerate FWM process in case d3.

The process of SC geneartion, can be better analyzed, if we use an integral characteristic as the second momentum of the spectral intensity:

$$W = \frac{\int(\lambda - \lambda_0)^2 I(\lambda) d\lambda}{\int I(\lambda) d\lambda} \tag{12}$$

The evolution along the fiber of W and the measured and averaged SC width are shown in Fig. 11. Besides the many jumps in the dependance of the SC width from the propagation distance z, it is clear that there is a threshold propagation distance $z_{tr1} \approx 0.4$m, around which the spectral content broadens signifficanlty. After z_{tr1} the dependance of is monotonic and continuous, which is expected to saturate when the efficiency of the nonlinear processes is reduced due to pump power depletion. Interestingly, a second jump of the avaraged SC width from around 200nm to arround 400 nm can be clearly distinguished at propagation distances arround $z_{tr2} = 1.6$m. This is probably due to merging of the FWM sidebands with central SC part. Note, that for the integral characteristic W, a second jump is not observed, i.e., after the initial dramatic broadening at $z \approx 0.5$m, the integral spectral content is monotonically slowly increasing.

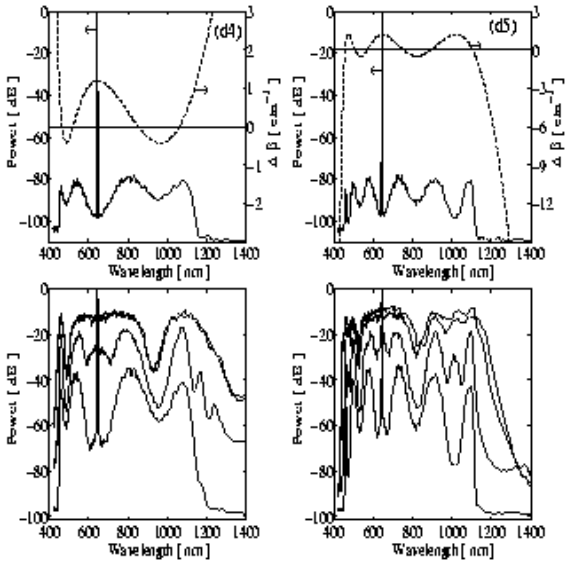

Fig. 9. Dispersion profiles d4 (left) and d5 (right). Top row: phase mismatch $\Delta\beta$ for direct degenerate FWM (dashed line) and the spectrum at L=10cm (solid line). Bottom row: spectrum at L=20cm, 30cm, 1m, and 2m (down to up).

5.2 Propagation dynamics in the temporal domain

Recently, it was theoretically and experimentally verified [22, 23, 24, 26] that the process of higher order soliton splitting can have a dominant contribution to the formation of SC spectra in PCFs. The influence of weak higher order perturbations to the NLSE on the pulse evolution has been reported by many authors, see e.g. [44, 45]. The main idea is that weak perturbations of the NLSE, do not significantly change the fundamental soliton solution. However, as the bound energy of a multisoliton or bound soliton solution of the NLSE is zero, the weak perturbations will lead to splitting of the initial multisoliton condition in to the constituent N solitons plus radiation of linear waves. In Fig.12, we show the temporal evolution of the fast axes component for the d1-d6 dispersion profiles. As seen, except for the d6 dispersion profile, there is a clear evidence for pulse splitting effect. However, it is not clear, which of the higher order additional linear and nonlinear terms in the GNSE have the dominant contribution for the corresponding simulation results. Thus, in Fig.13 we show two additional simulations for the dispersion case d4. It is apparent, that in the present case, the higher order dispersion has the strongest effect in the pulse splitting, but the contribution from the Raman effect cannot be completely neglected. In other cases—for other parameters—the relative importance of these terms may change and indeed

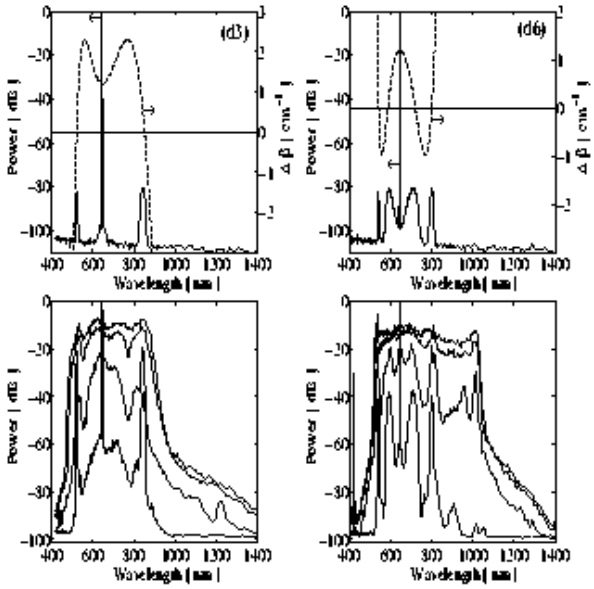

Fig. 10. Dispersion profiles d3 (left) and d6 (right). Top row: phase mismatch $\Delta\beta$ for direct degenerate FWM (dashed line) and the spectrum at L=10cm (solid line). Bottom row: spectrum at L=20cm, 30cm, 1m, and 2m (down to up).

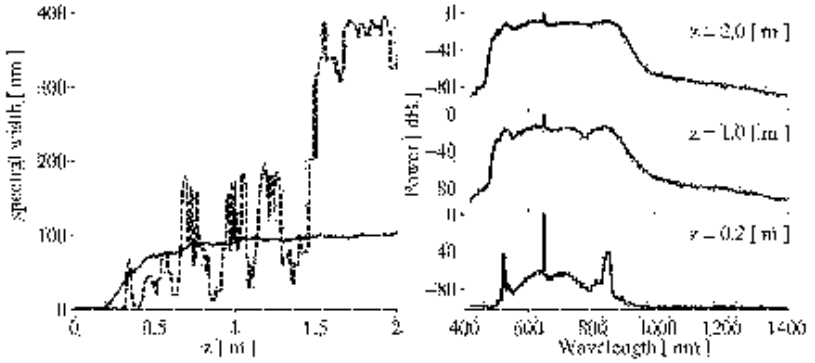

Fig. 11. Left: dashed line is the width of the SC spectra for dispersion profile d4 at 20dB from the maximal intensity and averaging 200 points and smoothed over 10, solid line, the integral width W(z) calculated from Eq.12. Right: SC spectra for dispersion case d4 for different propagation lenghts.

the Raman effect alone have been observed to mediate a splitting [44] and also the third-order dispersion alone may lead to splitting [45].

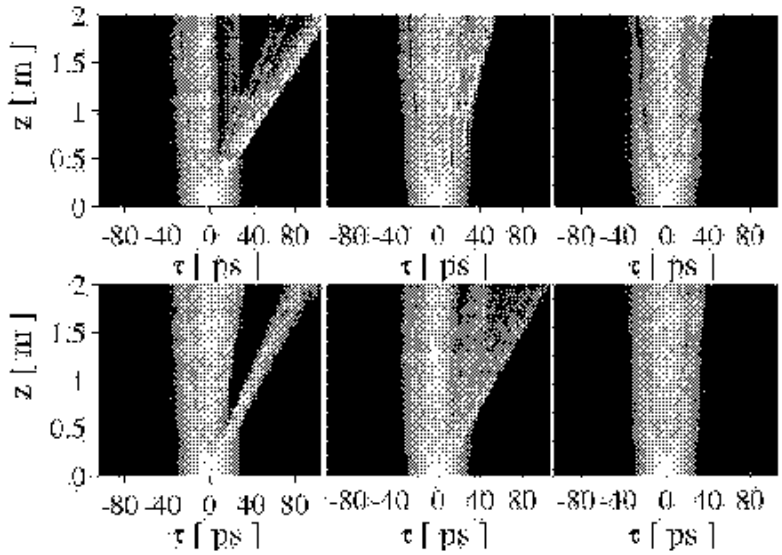

Fig. 12. Pulse temporal evolution. Regions with high intensity are in white. Top row: from left to right dispersion cases d1-d3. Bottom row: from left to right dispersion cases d4-d6

The observed effect can be explained by theoretical results. When relatively long picosecond and nanosecond pulses are considered, only the small frequency shift part of the Raman response function should be taken into account. Thus, according to the developed theory in [43, 44], the first-order single soliton acquires the largest Raman induced delay time, given by:

$$\Delta t[ps] = 6.5 * 10^{-4} \frac{Z^2[m] n_2[cm^2/W] E_m^4[W/cm^2] Im(a2)[cm.s/W]}{\lambda[nm]} \qquad (13)$$

Here, Z is the propagation distance along the fiber, $n_2 = 3.2 * 10^{-16} cm^2/W$ is the nonlinear coefficient for solica, $Ima_2 = 4.1 * 10^{-26} cm.s/W$ is the differential Raman amplitude gain coefficient, $E_m[W/cm^2] = I_p[W]/A_{eff}[cm^2]$ is the peak electric field, and λ is the pump wavelength. Thus, for $I_p = 400W$, $A_{eff} = 1.94 \mu m^2$, and $\lambda = 647nm$, we obtain for the induced delay time:

$$\Delta t[ps] = 1.5 * 10^{-3} \frac{ps}{m^2} Z^2[m] \qquad (14)$$

For our maximum propagation distance of $3m$, the amount of pulse splitting predicted by Eqs. (13 and 14) is $1.4 * 10^{-2} ps$. This is very small compared to

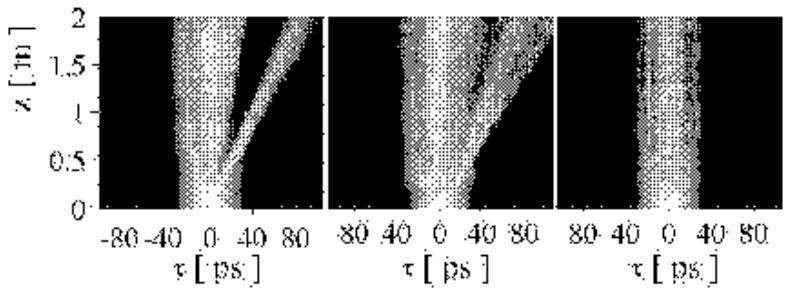

Fig. 13. Temporal evolution for dispersion case d4. Left: with Raman term and higher order, β_i, $i > 2$, dispersion terms. Center: Higher order dispersion terms are included, but there is no Raman contribution to the nonlinearity ($f_R = 0$). Right: All higher order dispersion terms($i > 2$) are zero while the Raman nonlinearity ($f_R = 0.18$) is retained.

the shown pulse splitting corresponding to the dispersion case d4 in Fig.12 and Fig.13. This also proves, that for the dispersion case d4, the Raman effect has almost no contribution to the pulse splitting. Since Eq. (13) does not depend on the dispersion, we can conclude, that for all other dispersion cases d1-d6, the Raman nonlinearity, does not contribute to the observed pulse splitting.

5.3 Influence of the PCF structural irregularities

The SC generation process that we have considered here is mainly determined by parametric FWM, which requires phase-matching. In the experiments with a PCF with dispersion profile d1 [12, 10], Stokes and anti-Stokes lines due to direct degenerate FWM were generally not observed. This was explained to be due to irregularities along the PCF, leading to violation of the required phase matching condition Eq. (3). Thus, in order to conclude that parametric FWM can be used for broad-band SC generation in real PCFs, we investigate the robustness of the process towards fluctuations of the dispersion coefficients along the fiber.

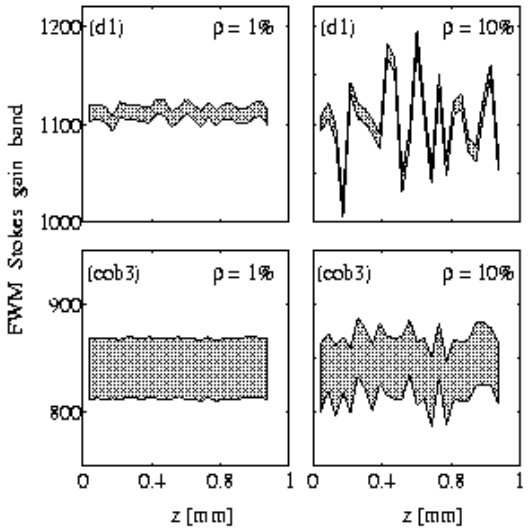

Fig. 14. Random fluctuations of the FWM Stokes gain band $g(\Delta\beta)$ (grey region), given by Eq. (4), for constant pump I_p and ρ=1% (left) and ρ=10% (right). The upper row is for case d1 and the bottom row for case cob3.

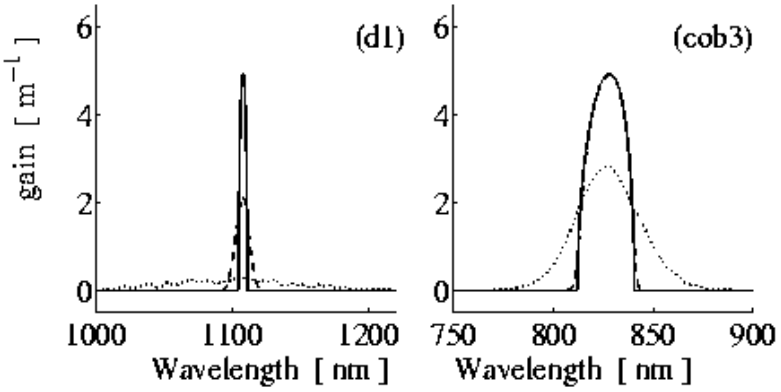

Fig. 15. Average FWM Stokes gain g_{av} over L=2cm, as given by Eq. (15) in the undepleted pump approximation. Shown is case d1 (left) and cob3 (right) for ρ=0 (solid), ρ=1% (dashed), and ρ=10% (dotted).

Random fluctuations of the whole dispersion profile will randomly change not only the zero-dispersion wavelength λ_{ZD}, but more importantly, the phase-mismatch curve $\Delta\beta(\lambda)$, given by Eq. (3). This in turn implies that the FWM gain spectrum $g(\Delta\beta)$, given by Eq. (4), will vary randomly along

the fiber, even in the undepleted pump approximation (constant peak power I_p).

In Fig. 14, we have depicted the fluctuation of the FWM Stokes gain band in the undepleted pump approximation over the first L=1mm of a PCF with dispersion profiles d1 (λ_s=1110nm) and cob3 (λ_s=800nm). As expected, the broader gain band of fiber cob3 is reflected in a suppression of the oscillations, as compared to the fiber d1 used in the experiments in [12].

The variation of the direct degenerate FWM Stokes gain band gives an impression of the influence of the dispersion fluctuations on the effectiveness of the FWM process. The important factor is the average FWM gain over the fiber length L, defined as

$$g_{av} \equiv \frac{1}{L} \int_0^L g[\Delta\beta(z)]\ dz, \tag{15}$$

where we have indicated the z-dependence of the phase-mismatch as a result of the fluctuations. In Fig. 15, we show the average FWM Stokes gain calculated over the first L=2cm using the undepleted pump approximation. The reduction of the average gain for increasing strength of the fluctuations are clearly observed. Theoretically, we thus predict that in fiber d1, realis-

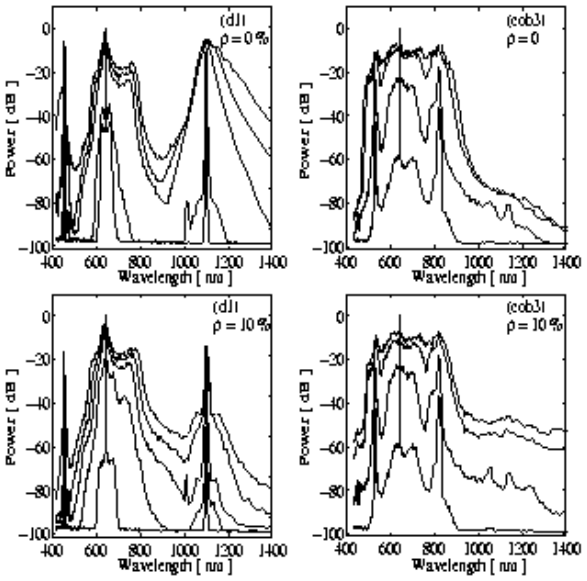

Fig. 16. Dispersion profiles d1 (left) and cob3 (right). Spectrum under influence of fluctuations with strength ρ=0 (top row) and ρ=10% (bottom row) at L=20cm, 30cm, 1m, 2m, and 3.7m (down to up).

tic fluctuations would significantly suppress the Stokes and anti-Stokes lines generated from the pump by direct degenerate FWM, as also stated by Coen *et al.* [12]. The corresponding simulations, presented in Fig. 16 (left), confirms this prediction. Using direct degenerate FWM to generate an ultra-broad SC in the particular fiber, d1 is, therefore, not realistic.

In contrast, with our proposed cob-web fiber cob3 with a broad gain band, even fluctuations with ρ=10% should not significantly reduce the FWM effectiveness, which is also confirmed by our simulations shown in Fig. 16 (right). In our proposed fibers d4-d5, the FWM gain band is even broader, indicating that fluctuations will have even less impact. Thus our numerical results show that using direct degenerate FWM to generate an ultra-broad SC is a realistic option.

6 Conclusion

We have described the theoretical model and the numerical procedure for the simulation of SCG in PCFs with low-power 30 picosecond pulses with 400W peak power. The model is applicable for simulations of wide spectral bands up to 1/3 of the central frequency. All possible nonlinear processes due to the $\chi^{(3)}$ nonlinearity are taken in to account.

It is shown that if the dispersion is properly designed, the parametric processes and particularly the direct degenerate FWM, can have significant contributions to the generated SC spectra. This is verified by performing simulations taking into account structural PCF irregularities modelled as random variation of the dispersion coefficients.

Further, we demonstrate, how the considered dispersion profiles leading to stable direct degenerate FWM, may be practically obtained. Calculations of the dispersion of PCF with a cob-web transverse structure show that for certain values of their parameters, the dispersion obtained is suitable for the formation of ultra broad SC spectra, by generation, broadening and final merging of the widely separated direct degenerate FWM bands with the central SC part.

In the temporal domain, pulse splitting is observed, which is probably caused by multisoliton fission due to higher-order linear and nonlinear terms included in the generalized NLSE. It is shown that for certain values of the simulation parameters, the different terms will have different influence. However, we do not quantify the exact contribution of this interesting and prospective mechanism for spectral broadening in the simulations of SC generation considered here.

Finally, we note that this model can be further modified to better represent the experimental conditions by considering the specific fiber loss and effective area spectral dependance as well as including the orthogonal component of the Raman gain.

We acknowledge support from the Danish Center for Scientific Computing (DCSC) under contract no. CPU-1101-27. This work was supported by the Danish Technical Research Council (Grant no. 26-00-0355) and the Graduate School in Nonlinear Science (The Danish Research Agency).

References

1. T. A. Birks, J. C. Knight, and P. St. J. Russel, "Endlessly single-mode photonic crystal fiber," Opt. Lett. **22**, 961-963 (1997).
2. J. C. Knight, T. A. Birks, P. St. J. Russel, and D. M. Atkin, "All-silica single-mode optical fiber with photonic crystal cladding," Opt. Lett. **21**, 1547-1549 (1996); **22**, 484-485 (1997).
3. J. C. Knight, J. Broeng, T. A. Birks, and P. St. J. Russel, "Photonic band gap guidance in optical fibers," *Science* **282**, 1476-1478 (1998).
4. J. Broeng, S. E. Barkou, T. Sondergaard, and A. Bjarklev, "Analysis of air-guiding photonic bandgap fibers," Opt. Lett. **25**, 96-98 (2000)
5. , J. C. Knight, "Photonic crystal fibers," Nature **424**, 847-851 (2003).
6. *The Supercontinuum Laser Source*, R. R. Alfano, ed. (Springer-Verlag, New-York, 1989).
7. R. R. Alfano and S. L. Shapiro, "Emmision in the region 4000 to 7000Å via four-photon coupling in glass," Phys. Rev. Lett. **24**, 584-587 (1970).
8. R. R. Alfano and S. L. Shapiro, "Observation of self-phase modulation and small-scale filaments in crystals and glasses," Phys. Rev. Lett. **24**, 592-594 (1970).
9. C. Lin and R. H. Stolen, "New nanosecond continuum for excited-state spectroscopy," Appl. Phys. Lett. **28**, 216-218 (1976)
10. S. Coen, A. H. L. Chau, R. Leonardt, J. D. Harvey, J. C. Knight, W. J. Wadsworth, and P. S. J. Russell, "White-lightsupercontinuum generation with 60-ps pulse in a photonic crystal fiber," Opt. Lett. **26**, 1356-1358 (2001)
11. P. L. Baldeck and R. R. Alfano, "Intensity effects on the stimulated four photon spectra generated by picosecond pulses in optical fibers," IEEE J.Lightwave Technol. **5**, 1712-1715 (1987)
12. S. Coen, A. Chao, R. Leonardt, and J. Harvey, J. C. Knight, W. J. Wadsworth, and P. S. J. Russell, "Supercontinuum generation via stimulated Raman scattering and parametric four-wave-mixing in photonic crystal fibers," J. Opt. Soc. Am. B **19**, 753-764 (2002)
13. K. Mori, H. Takara, S. Kawanishi and T. Morioka, "Flatly broadened supercontinuum spectrum generated in a dispersion decreasing fiber with convex dispersion profile," Electron. Lett. **33**, 1806-1808 (1997).
14. K. Mori, H. Takara, and S. Kawanishi, "Analysis and design of supercontinuum pulse generation in a single-mode optical fiber," J. Opt. Soc. Am. B **18**, 1780-1792 (2001).
15. K. Tamura, H. Kubota, and M. Nakazawa, "Fundamentals of stable continuum generation at high repetition rates," IEEE J. Quantum Electron. **36**, 773-779 (2000).
16. A. Ferrando, E. Silvestre, J. J. Miret, and P. Andres, "Nearly zero ultraflattened dispersion in photonic crystal fibers," Opt. Lett. **25**, 790-792 (2000).

17. A. Ferrando, E. Silvestre, P. Andres, J. J. Miret, and M. V. Andres, "Designing the properties of dispersion-flattened photonic crystal fibbers," Opt. Express **9**, 687-697 (2001).
18. Kim P. Hansen, J. R. Jensen, C. Jacobsen, H. R. Simonsen, J. Broeng, P. M. W. Skovgaard, A. Petersson, A. Bjarklev, "Highly Nonlinear Photonic Crystal Fiber with Zero-Dispersion at 1.55 m" OFC '02 Post Deadline FA **9**, 2002
19. T. A. Birks, W. J. Wadsworth, and P. St. J. Russell, "Supercontinuum generation in tapered fibers," Opt. Lett. **25**, 1415-1417 (2000).
20. J. K. Ranka, R. S. Windler, and A. J. Stentz, "Visible continuum generation in air-silica microstructure optical fibers with anomalous dispersion at 800 nm," Opt. Lett. **25**, 25-27 (2000).
21. A. V. Gusakov, V. P. Kalosha, and J. Herrmann, "Ultrawide spectral broadening and pulse compression in tapered and photonic fibers," *Quantum Electronics and Laser Science*, Vol.57 of OSA Trends in optical Technology Series (Optical Society of America, Wasington,D.C., 2001) p. 29
22. W. J. Wadsworth, A. Ortigosa-Blanch, J. C. Knight, T. A. Birks, T. P. M. Man, and P. St. J. Russell, "Supercontinuum generation in photonic crystal fibers and optical fiber tapers: a novel light source," J. Opt. Soc. Am. B **19**, 2148-2155 (2002)
23. A. V. Husakou and J. Herrmann, "Supercontinuum generation, four-wave mixing, and fission of higher-order solitons in photonic-crystal fibers," J. Opt. Soc. Am. B **19**, 2171-2182 (2002)
24. J. Herrmann, U. Griebner, N. Zhavoronkov, A. Husakou, D. Nickel, J. C. Knight, W. J. Wadsworth, P. St. J. Russell, and G. Korn, "Experimental Evidence for Supercontinuum Generation by Fission of Higher-Order Solitons in Photonic Fibers," Phys. Rev. Lett. **88**, 1739011-1739014 (2002)
25. J.M. Dudley, L. Provino, N. Grossard, H. Maillotte, R. S. Windler, B. J. Eggleton and S. Coen, "Supecontinuum generation in air-silica microstructured fibers with nanosecond and femtosecond pulse pumping," J. Opt. Soc. Am. B **19**, 765-771 (2002)
26. K. M. Hilligsøe, H. N. Paulsen, Jan Thøgersen, S. R. Keiding, and J. J. Larsen, "Initial steps of supercontinuum generation in photonic crystal fibers," J. Opt. Soc. Am. B **20**, 1887-1893 (2003)
27. N. I. Nikolov, O. Bang, T. Sørensen, and A. Bjarklev, "Improving efficiency of supercontinuum generation in photonic crystal fibers by direct degenerate four-wave-mixing," J. Opt. Soc. Am. B **20**, 2329-2337 (2003)
28. W.H. Reeves, J.C. Knight, and P.St.J. Russell, "Demonsttration of ultra-flattened dispersion in photonic crystal fibers", Opt. Express **10**, 609-613 (2002).
29. K. P. Hansen , "Dispersion flattened hybrid-core nonlinear photonic crystal fiber", Opt. Express **11**, 1503-1509 (2003).
30. J.C. Knight, J. Arriaga, T.A. Birks, A. Ortigosa-Blanch, W.J. Wadworth, and P.St.J. Russell, "Anomalous dispersion in photonic crystal fiber", IEEE Phot. Tech. Lett. **12**, 807-809 (2000).
31. C.D. Pole, J.H. Winters and J.A. Nagel, "Dynamical equations for polarization dispersion," Opt. Lett. **16**, 372-374 (1991).
32. P.K.A. Wai, C.R. Menyuk and H. H. Chen, "Effects of randomly varying birefringence on soliton interactions in optical fibers," Opt. Lett. **16**, 1735-1737 (1991)
33. P. O. Hedekvist, M. Karlsson, and P. A. Andrekson, "Polarization dependence and efficiency in a fiber four-wave mixing phase conjugator with orthogonal pump waves," Photonics Technol. Lett. **8**, 776-778 (1996)

34. M. Karlsson, "Four-wave mixing in fibers with randomly varying zero-dispersion wavelength," J. Opt. Soc. Am. B **15**, 2269-2275 (1998)
35. N. Kuwaki and M. Ohashi, "Evaluation of longitudinal chromatic dispersion," J.Lightwave Technol. **8**, 1476-1481 (1990)
36. J. Garnier and F.Kh. Abdullaev, "Modulational instability by random varying coefficients for the nonlinear Schrö dinger equation," Physica D **145**, 65-83 (2000)
37. R. Knapp, "Transmission of solitons through random media," Physica D **85**, 496-508 (1995)
38. K.J. Blow, and D. Wood, "Theoretical description of transient stimulated Raman scattering in optical fibers," IEEE J. Quantum Electron.**25**, 2665-2673 (1989)
39. S. Tzortzakis, L. Sudrie, M. franco, B. Prade, A. Mysyrowicz, A. Couairon, and L. Berge, "Self-guided propagation of ultrashort IR laser pulses in fused silica" Phys. Rev. Lett. **87**, 2139021-2139024 (2001)
40. P. T. Dinda, G. Millot, and S. Wabnitz, "Polarization switching and suppression of stimulated Raman scattering in birefringent optical fibers," J. Opt. Soc. Am. B **15**, 1433-1441 (1998)
41. G.P. Agrawal, *Nonlinear Fibre Optics*, 2nd ed. Academic, San Diego, Calif., (2000).
42. Steven G. Johnson and J. D. Joannopoulos, "Block-iterative frequency-domain methods for Maxwell's equations in a planewave basis," Opt. Express **8**, 173-190 (2001).
43. Y. Kodama and A. Hasegawa, "Nonlinear pulse propagation in monomode dielectric guide," IEEE J. Quantum Electron. **23**, 510-524 (1987)
44. K. Tai, A. Hasegawa and N. Bekki, "Fission of optical solitons by stimulated Raman effect," Opt. Lett. **13**, 392-394 (1988)
45. P. K. A. Wai, C. R. Menyuk, Y. C. Lee, and H. H. Chen, "Nonlinear pulse propagation in the neighbourhood of the zero-dispersion wavelength of monomode optical fibers," Opt. Lett. **11**, 464-466 (1986)

Contents

Appendix E

Improving efficiency of supercontinuum generation in photonic crystal fibers by direct degenerate four-wave mixing

Nikola I. Nikolov, Thorkild Sørensen, Ole Bang, and Anders Bjarklev, Improving efficiency of supercontinuum generation in photonic crystal fibers by direct degenerate four-wave mixing, Journal of the Optical Society of America B Volume 20, 2329 (2003).

Nikolov *et al.* Vol. 20, No. 11/November 2003/J. Opt. Soc. Am. B 2329

Improving efficiency of supercontinuum generation in photonic crystal fibers by direct degenerate four-wave mixing

Nikola I. Nikolov

Informatics and Mathematical Modelling, Technical University of Denmark, DK-2800 Kongens Lyngby, Denmark, and Risø National Laboratory, Optics and Fluid Dynamics Department, OFD-128 P.O. Box 49, DK-4000 Roskilde, Denmark

Thorkild Sørensen

Research Center COM, Technical University of Denmark, DK-2800 Kongens Lyngby, Denmark

Ole Bang

Research Center COM, Technical University of Denmark, DK-2800 Kongens Lyngby, Denmark, and Informatics and Mathematical Modelling, Technical University of Denmark, DK-2800 Kongens Lyngby, Denmark

Anders Bjarklev

Research Center COM, Technical University of Denmark, DK-2800 Kongens Lyngby, Denmark

Received July 28, 2003; revised manuscript received August 5, 2003; accepted August 5, 2003

We numerically study supercontinuum generation in photonic crystal fibers pumped with low-power 30-ps pulses close to the zero dispersion wavelength. We show how the efficiency is significantly improved by designing the dispersion to allow widely separated spectral lines generated by degenerate four-wave mixing directly from the pump to broaden and merge, resulting in a 800-nm-wide supercontinuum. Full-vectorial plane-wave calculations show that a cobweb photonic-crystal-fiber structure can realize the dispersion profiles under consideration. The predicted efficient supercontinuum generation is more robust and survives fiber imperfections modeled as random fluctuations of the dispersion coefficients along the fiber. © 2003 Optical Society of America

OCIS codes: 190.4370, 190.4380, 190.5650.

1. INTRODUCTION

After the first observation of a 200-THz supercontinuum (SC) spectrum of light in bulk glass,[1,2] much has been done on the understanding and control of this process.[3] A target of numerous experimental and theoretical investigations has been the improvement of the characteristics and simplification of the technical requirements for the generation of a SC.[3] The first experiments in bulk materials, based on self-phase modulation, required extremely high peak powers (>10 MW).

New techniques based on the use of optical fibers as a nonlinear medium for SC generation allowed lower peak powers to be used due to the long interaction length and high effective nonlinearity.[4–7] However, the necessity to operate near the wavelength for zero group-velocity dispersion restricted the SC generation to the spectral region around and above 1.3 μm. The use of dispersion-flattened or dispersion-decreasing fibers as nonlinear media for SC generation resulted in a flat SC spanning 1400–1700 nm[8,9] and 1450–1650 nm,[10] respectively. The spectrum was still far from the visible wavelengths.

Photonic crystal fibers (PCFs) and tapered fibers overcome these limitations. The unusual dispersion properties and enlarged effective nonlinearities make them a promising tool for effective SC generation.[6] PCFs and tapered fibers have similar dispersion and nonlinearity characteristics, and they have the advantage that their dispersion may be significantly modified by a proper design of the cladding structure[11–14] or by a change of the degree of tapering,[15] respectively. With kilowatt peak-power femtosecond pulses, a SC spanning 400–1500 nm has been generated in a PCF[14] and in a tapered fiber.[15] The broad SC has been explained to be a result of SPM and direct degenerate four-wave mixing[16] (FWM). Later, it was also reported that a SC spanning from 380 to 1600 nm is obtainable with 200-fs pulses with an energy less than 5 nJ.[17] The theoretical explanation includes nonlinear processes such as fission of higher-order solitons.[17–19]

However, high-power femtosecond lasers are not necessary; SC generation may be achieved with low-power picosecond[6,7] and even nanosecond[20] pulses. Thus Coen *et al.* generated a broad SC in a PCF using picosecond pulses with subkilowatt peak power and showed that the primary mechanism was the combined effect of stimu-

0740-3224/2003/112329-09$15.00

2330 J. Opt. Soc. Am. B/Vol. 20, No. 11/November 2003 Nikolov et al.

lated Raman scattering (SRS) and parametric four-wave mixing (FWM), allowing the Raman-shifted components to interact efficiently with the pump.[6]

Using 200-fs high-power pulses and a 1-cm-long tapered fiber, Gusakov has shown that direct degenerate FWM can lead to ultrawide spectral broadening and pulse compression.[16] We consider how the direct degenerate FWM can significantly improve the efficiency of SC generation with subkilowatt picosecond pulses in PCFs, and we go one step further by optimizing the effect through engineering of the dispersion properties of the PCF. We show that by a proper design of the dispersion profile, the direct degenerate FWM Stokes and anti-Stokes lines can be shifted closer to the pump, thereby allowing them to broaden and merge with the pump to form an ultrabroad SC. This significantly improves the efficiency of the SC generation, since the power in the Stokes and anti-Stokes lines no longer is lost.

Improvement of the SC generation by enhancing the role of parametric processes, such as direct degenerate FWM, relies on the possibility of fabricating PCFs with a proper dispersion. It is theoretically predicted that, by varying the hole size and pitch in a triangular silica–air PCF, an ultraflattened dispersion is achievable.[11,12] Flat dispersion profiles with slope within 0.017 ps/nm^2·km have been obtained.[21] Recently a new fiber structure with a threefold symmetry has been shown to enable unprecedented dispersion control while maintaining low loss and a high nonlinear coefficient.[22] In our work, we have considered cobweb PCFs,[23] and by varying the core diameter, we have obtained dispersion profiles similar to those predicted to give the most efficient SC generation.

External perturbations and different types of imperfections lead to fluctuations of the fiber parameters along the length of the fiber. Fluctuations in fiber birefringence,[24,25] dispersion,[26–28] and nonlinearity[29,30] have been investigated to understand their influence on different regimes of light propagation. As parametric processes require phase matching, the effectiveness of the FWM could be strongly influenced by random fluctuations of the dispersion. Indeed, Coen *et al.* in their PCF experiments with low-power picosecond pump pulses at 647 nm[6,7] and nanosecond pump pulses at 532 nm[20] explain the absence of frequencies generated by direct degenerate FWM from the pump, by the large frequency shift, and by the violation of the required phase-matching condition due to fiber irregularities.

We have analyzed the influence of a random change of the dispersion coefficients along the fiber on the process of SC generation and find that the generation and merging of the direct degenerate FWM Stokes and anti-Stokes waves with the pump could be robust enough to survive fiber imperfections, and thus a significant improvement of the process of SC generation should indeed be possible in real PCFs.

2. THEORETICAL MODEL AND FIBER DATA

We study numerically the SC generation process using the well known coupled nonlinear Schrödinger equations that describe the evolution of the x- and y-polarization components of the field for pulses with a spectral width of up to 1/3 of the pump frequency,[6,31]

$$\frac{\partial A_j}{\partial z} = i\mu A_j + i(j-1)\delta\beta A_j + (-1)^j\frac{\Delta}{2}\frac{\partial A_j}{\partial \tau} - \frac{i}{2}\sum_{k=2}^{7}\frac{\beta_k}{k!}\frac{\partial^k A_j}{\partial \tau^k} + i\gamma\left(1+\frac{i}{\omega_p}\frac{\partial}{\partial \tau}\right) \times \left\{A_j f_R\int h_R(\tau-s)(|A_j(s)|^2+|A_{3-j}(s)|^2)ds + (1-f_R)\left[\left(|A_j|^2+\frac{2}{3}|A_{3-j}|^2\right)A_j+\frac{1}{3}A_j^* A_{3-j}^2\right]\right\}. \tag{1}$$

Here the complex fields $A_j = A_j(t, z)$ with $j = 1, 2$ are given by $A_1 = E_x$ and $A_2 = E_y \exp(i\delta\beta z)$, where E_x and E_y are the envelopes of the real linearly polarized x and y components. The time $\tau = t - z/\bar{v}$ is in a reference frame moving with the average group velocity $\bar{v}^{-1} = (v_x^{-1} + v_y^{-1})/2$, z is the propagation coordinate along the fiber, μ is the fiber loss, $\delta\beta = \beta_x - \beta_y = \omega_0\delta n/c$ is the phase mismatch due to birefringence $\delta n = n_x - n_y$, and $\Delta = (v_x^{-1} - v_y^{-1})$ is the group-velocity mismatch between the two polarization axes. The propagation constant $\beta(\omega)$ is expanded to eighth order around the pump frequency ω_p with coefficients β_k keeping β_{2-7} the same for x- and y-linearly polarized components, γ is the effective nonlinearity, f_R is the fractional contribution of the Raman effect, and finally $*$ denotes complex conjugation.

This model accounts for self-phase modulation, cross-phase modulation, FWM, and SRS. For the Raman susceptibility h_R, we include only the parallel component, as the orthogonal component is generally negligible in most of the frequency regime that we consider.[32] The Raman susceptibility is approximated by the expression[33]

$$h_R(t) = \frac{\tau_1^2+\tau_2^2}{\tau_1\tau_2^2}\exp(-t/\tau_2)\sin(t/\tau_1), \tag{2}$$

where $\tau_1 = 12.2$ fs and $\tau_2 = 32$ fs. Furthermore, $f_R = 0.18$ is estimated from the known numerical value of the peak Raman gain.[33]

The phase mismatch for the direct degenerate FWM of two photons at the pump frequency is $\Delta\beta = \beta_s + \beta_{as} - 2\beta_p + 2\gamma I_p$,[33] where I_p is the peak power.[33] In the frequency domain we have

$$\Delta\beta = 2\left[\Omega^2\frac{\beta_2}{2!}+\Omega^4\frac{\beta_4}{4!}+\Omega^6\frac{\beta_6}{6!}+\gamma(1-f_R)I_p\right], \tag{3}$$

where $\Omega = \omega_p - \omega_s = \omega_{as} - \omega_p$. The gain g of the direct degenerate FWM[7,33] is

$$g = \{[(1-f_R)\gamma I_p]^2 - (\Delta\beta/2)^2\}^{1/2}. \tag{4}$$

We consider the same PCF and use the same numerical and experimental data as in Ref. 6, kindly provided by S. Coen. We pump along the slow axis with 30-ps sech-

Table 1. Dispersion Profiles[a]

Case	β_2	β_4	β_6	λ_π	$D(\lambda_p)$	λ_s	λ_{as}
d1	7.0	−4.9	−1.8	677	−31.6	1108	457
d2	14	−34.4	−0.04	697	−62.3	852	522
d3	1.0	−2.5	−3.3	652	−4.5	849	523
d4	−0.28	0.05	0.29	647	1.3	1083	461
						822	534
d5	−1.01	2.14	−2.84	643	4.54	1096	459
						911	552
						735	578
d6	−1.3	−2.6	58.8	641	5.9	803	628
						713	593

[a] Dispersion coefficients β_2 [ps^2/km], β_4 [10^{-5} ps^4/km], and β_6 [10^{-10} ps^6/km] for dispersion profiles d1–d6, with corresponding dispersion at the pump wavelength $D(\lambda_p)$ [ps/nm-km)], zero dispersion wavelength λ_π [nm], and Stokes λ_s [nm] and anti-Stokes λ_{as} [nm] wavelengths. Fixed coefficients: $\beta_8 = 5.1 \times 10^{-2}$ ps^8/km, $\beta_{10} = 1.2 \times 10^{-7}$ ps^{10}/km, and $\beta_{12} = 1.2 \times 10^{-12}$ ps^{12}/km.

shaped pulses of $I_p = 400$ W peak power and pump wavelength $\lambda_p = 647$ nm. The PCF has core area $A_{core} = 1.94\,\mu$m^2, birefringence $\delta n = 1.9 \times 10^{-6}$, and nonlinearity $n_2 = 3 \times 10^{-20}$ m^2/W. In our initial numerical analysis, we consider six different artificial dispersion profiles, for which β_{2-7} are given in Table 1, where case d1 corresponds to the PCF used in Ref. 6. Note that cases d4 + d6 and d5 have two and three sets of Stokes and anti-Stokes waves, respectively.

Here we are interested in studying the separate effect of different dispersion profiles (i.e., different values of β_{2-7}). We therefore keep all other fiber and pulse parameters constant and neglect the frequency dependence of the effective area A_{eff} and the loss μ. Thus we assume a uniform loss of $\mu = 0.1$ dB/m and approximate A_{eff} with the core area, so that $\gamma = 2n_2/(\lambda_p A_{core}) = 0.15$(W m)$^{-1}$.

For our numerical simulation, we use the standard second-order split-step Fourier method, solving the nonlinear part with a fourth-order Runge–Kutta method using a Fourier transform forth and back and the convolution theorem. Except where otherwise stated, we use 2^{17} points in a time window of $T = 236$ ps, giving the wavelength window (405–1613 nm). The propagation step is $\Delta z = 43\,\mu$m. In our longest simulation out to $L = 3.7$ m, the photon number is conserved to within 5% of its initial value. An initial random-phase noise seeding of one photon per mode is included as in Ref. 6. All the presented spectra have been smoothed over 32 points.

3. NUMERICAL ANALYSIS

We first simulate SC generation using the same fiber as in Ref. 6, i.e., using the dispersion profile d1. Due to our large spectral window (405–1613 nm), we see in Fig. 1 (left) the emergence of direct-degenerate FWM Stokes and anti-Stokes waves at the predicted wavelengths $\lambda_\pi = 1108$ nm and $\lambda_{as} = 457$ nm, for which the phase-matching condition (3) is satisfied. From the standard expressions given in Ref. 33, we find the maximum direct degenerate FWM gain (g) to be twice the maximum SRS gain, which explains why the FWM Stokes and anti-Stokes components appear before the SRS components.

For a given peak power, the loss and temporal walk-off of the PCF gives the maximum distance L_{max} over which nonlinear processes, and thus the SC generation process, are efficient. From Fig. 1 (left) we see that, after the FWM Stokes and anti-Stokes components are generated, they broaden in the same way as the central part of the spectrum around the pump. The merging of the spectral parts around λ_{as}, λ_p, and λ_π would create an ultrabroad spectrum as observed in tapered fibers with high-power femtosecond pulses.[15,16] However, for high-power femtosecond pulses, the SPM is the dominant mechanism that leads to broadening and merging of the Stokes and anti-Stokes lines with the pump. For low-power picosecond pulses, the Raman and parametric processes are dominant. Thus in this particular case, the large frequency shift (~193 THz) of the degenerate FWM sidebands and the narrow degenerate FWM gain bands (~2 THz) prevent merging of the pump with the Stokes and anti-Stokes lines to happen within the maximum length L_{max}, i.e., before nonlinear effects become negligible. Indeed, it is seen from Fig. 1 that the spectrum does not change significantly from 1 m to 3.7 m. The power transferred to the Stokes and anti-Stokes lines is in effect lost, i.e., the SC process is not very efficient. By increasing the peak power, it would be possible to achieve merging of the spectral parts around λ_{as}, λ_p, and λ_π. However, our aim is to keep the low peak power fixed and instead to achieve this merging only by engineering the dispersion profile. Thus we modify the dispersion profile to adjust Eq. (3) to be fulfilled for wavelengths λ_π and λ_{as} closer to the pump $\lambda_p = 647$ nm. We do so by modifying β_2, β_4, and β_6 as listed in Table 1. The phase-matching condition $\Delta\beta = 0$ then gives $\lambda_\pi \approx 850$ nm and $\lambda_{as} \approx 522$ nm for case d2 and d3. In case d4–d6, additional Stokes and anti-Stokes waves exist. The dispersion profiles and phase-

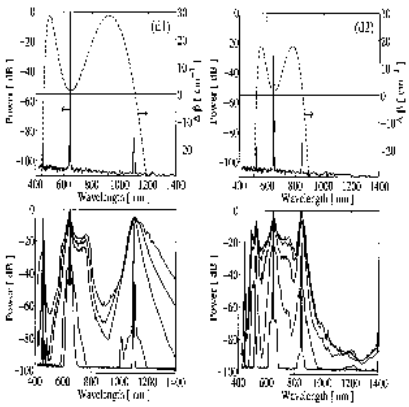

Fig. 1. Dispersion profiles d1 (left) and d2 (right). Top row: phase mismatch $\Delta\beta$ for direct degenerate FWM (dashed curve) and spectrum at $L = 10$ cm (solid curve). Bottom row: spectrum at $L = 20$ cm, 30 cm, 1 m, 2 m, and 3.7 m (down to up).

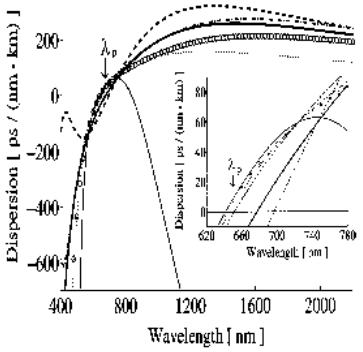

Fig. 2. Dispersion profile d1 (thick solid curve), d2 (dashed curve), d3 (dash-dotted curve), d4 (dotted curve), d5 (circles), and d6 (thin solid curve).

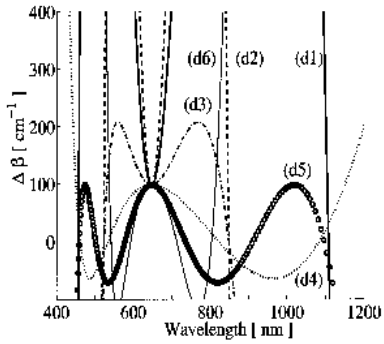

Fig. 3. Phase mismatch $\Delta\beta(\lambda)$ for dispersion profile d1 (thick solid curve), d2 (dashed curve), d3 (dash-dotted curve), d4 (dotted curve), d5 (circles), and d6 (thin solid curve).

mismatch curves corresponding to the cases in Table 1 are shown in Fig. 2 and Fig. 3, respectively. It is important to note that the curves $\Delta\beta(\lambda)$ have different slope around λ_s and λ_{as} (see Fig. 3).

We first consider only a shift of the Stokes and anti-Stokes lines closer to the pump and the effect it has on the improvement of the SC generation. Thus for the dispersion profile d2, the slope of the phase-mismatch curve around $\lambda_s \approx 850$ nm and $\lambda_{as} \approx 522$ nm is kept the same as for case d1. It is seen from Fig. 1 (right) that such a shift of the direct degenerate FWM Stokes and anti-Stokes lines closer to the pump is not enough for a complete merging to take place. This can be explained by considering the direct degenerate FWM gain $g(\lambda)$ shown in Fig. 4. The broadening of the Stokes and anti-Stokes lines is strongly influenced by the bandwidth of $g(\lambda)$, which is mainly determined by the slope around $\Delta\beta = 0$, i.e., around λ_s and λ_{as}. The slope and thus the gain bandwidth is the same in case d1 and d2, which explains why the broadening appears to be unchanged. One way to improve the SC spectrum is to shift the Stokes and anti-Stokes lines even closer to the pump, keeping the slope of the phase-mismatch curve around them constant. However, this will not significantly improve the width of the SC spectrum as compared with case d1, because the narrow direct degenerate FWM gain bands will then be in the region, where a SC is already generated by Raman and FWM processes. Moreover, this will lead to even more unusual dispersion profiles than that for case d2 (see Fig. 2), which does not seem to be experimentally realistic.

Instead, we fix λ_s and λ_{as} while reducing the slope and thus increasing the gain bandwidth. For dispersion profile d3, the direct degenerate FWM gain bandwidth is thus increased to 16.5 THz (see Fig. 4). This leads to broader Stokes and anti-Stokes lines in the initial stages of the SC generation and finally to their merging with the spectrum around the pump as seen from Fig. 5 (right). Thus a SC, which is flat within 10 dB and extending from around 500 nm to 900 nm, is formed after a propagation distance of $L = 2$ m despite use of low-power picosecond pulses. Moreover, the dispersion profile d3 is more realistic and may in fact be obtained in real PCF structures, such as the so-called cobweb PCF,[23] as we show in Section 4. The SC process is thus much more efficient with dispersion profile d3 than with d1, since the power in the Stokes and anti-Stokes lines is not lost. However, the SC may be further improved by designing the dispersion such that the phase mismatch $\Delta\beta(\lambda)$ has two or even three sets of Stokes and anti-Stokes lines, i.e., roots of the polynomial (3). The dispersion profiles d4 and d5 represent such cases with two and three sets of Stokes and anti-Stokes lines, respectively, around which the spectrum can broaden. From the corresponding gain curves in Fig. 4, we see that two gain bands actually overlap and form one broad gain band. The presence of extra Stokes and anti-

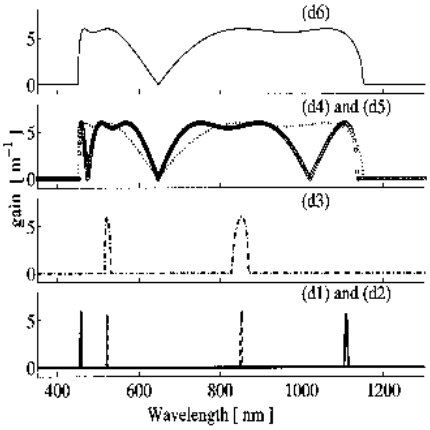

Fig. 4. Degenerate FWM gain $g(\lambda)$ for dispersion profile d1 (thick solid curve), d2 (dashed curve), d3 (dash-dotted curve), d4 (dotted curve), d5 (circles), and d6 (thin solid curve).

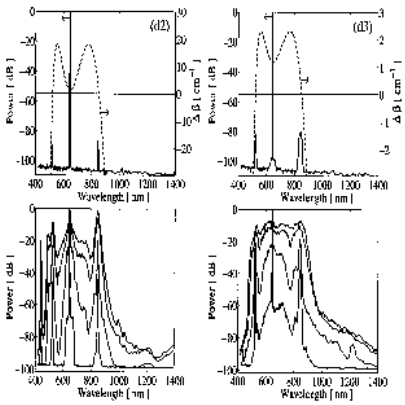

Fig. 5. Dispersion profiles d2 (left) and d3 (right). Top row: phase mismatch $\Delta\beta$ for direct degenerate FWM (dashed curve) and the spectrum at $L = 10$ cm (solid curve). Bottom row: spectrum at $L = 20$ cm, 30 cm, 1 m, and 2 m (down to up).

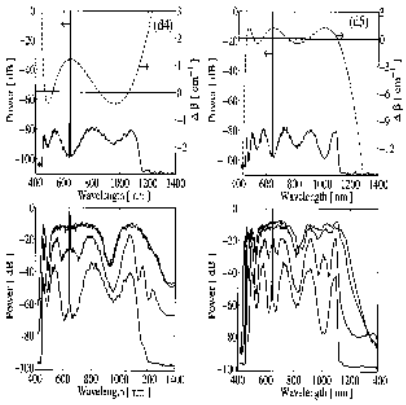

Fig. 6. Dispersion profiles d4 (left) and d5 (right). Top row: phase mismatch $\Delta\beta$ for direct degenerate FWM (dashed curve) and the spectrum at $L = 10$ cm (solid curve). Bottom row: spectrum at $L = 20$ cm, 30 cm, 1 m, and 2 m (down to up).

Stokes lines and the broad gain band could make the SC generation more efficient, provided they do not deplete the pump so much that the central SC spectrum around the pump deteriorates. From Fig. 6 (left) we see that, with the dispersion profile d4, the initial stage of the SC generation is indeed improved, the spectrum at $L = 10$ cm mainly reflecting the gain profile seen in Fig. 4. However, the small dip in the gain curve around 950 nm has a strong effect on the evolution of the spectrum, leaving a clear dip at 930 nm in the final SC spectrum. Optimizing the position of the two Stokes lines can remove this dip and lead to an even broader SC spectrum than observed in Fig. 5 for one set of Stokes and anti-Stokes lines.

Instead, we show in Fig. 6 (right) the evolution of the spectrum in a PCF with the dispersion profile d5, which has three sets of Stokes and anti-Stokes lines. The small dip in the gain curve around 800 nm (see Fig. 4) is still reflected in the spectrum, but it is now less pronounced, and we obtain a final ultrabroad SC spectrum ranging from 450 nm to 1250 nm within the 20-dB level. Of course the dispersion profile may be optimized further to remove the dip and make the SC spectrum more flat and even broader. So far, we have only considered the Stokes and anti-Stokes lines generated directly from the pump through degenerate FWM. However, so-called cascaded FWM processes also play an important role in the evolution of the spectrum, as discussed thoroughly in Ref. 6. In particular, one can use these processes to obtain a broader SC. The dispersion profile d6 is designed to clearly illustrate this effect. It still implies two sets of Stokes and anti-Stokes lines, but now these are very close to the pump, within the regime of wavelengths covered by the central SC generated by the pump. Nevertheless, we see in Fig. 7 (right) that additional lines are generated, around which the spectrum broadens, resulting in a final SC spectrum extending from 450 nm to 1 μm within 10 dB. The line at 1030 nm is generated by direct degenerate FWM from the Stokes wave at 720 nm, and the line at 1060 nm is generated by FWM between the Stokes wave at 720 nm and the pump. Thus these cascaded parametric processes result in a spectrum, which is broader than what was obtained with the direct degenerate FWM process in case d3.

Many investigations on designing the dispersion profile in PCFs have been made.[11–13,23] In Ref. 12, a well defined procedure to design specific predetermined dispersion profiles is established, and it is shown that it is pos-

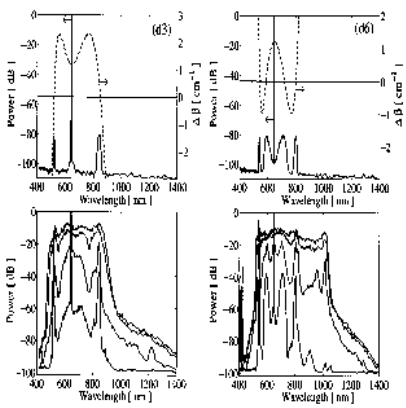

Fig. 7. Dispersion profiles d3 (left) and d6 (right). Top row: phase mismatch $\Delta\beta$ for direct degenerate FWM (dashed curve) and the spectrum at $L = 10$ cm (solid curve). Bottom row: spectrum at $L = 20$ cm, 30 cm, 1 m, and 2 m (down to up).

sible to obtain flattened dispersion profiles giving normal, anomalous, and zero dispersion in both the telecommunication window (around 1.55 μm) and the Ti–Za laser wavelength range (around 0.8 μm). This allows us to conclude that the dispersion profiles d3–d5 shown in Fig. 2 could indeed be fabricated. Thus we show in the next section how cobweb PCFs may be tailored to provide dispersion profile d3, as proposed and observed experimentally in Ref. 23.

4. PHOTONIC-CRYSTAL-FIBER STRUCTURE ANALYSIS

In Section 3 we show how a proper dispersion design can lead to a significant improvement of the SC. However, in our analysis, we manipulated the dispersion artificially by changing the values of $\beta_{2,4,8}$ while $\beta_{3,5,7}$ were kept constant. Thus we did not consider any practically realizable PCF structure that may be fabricated and provide the artificial dispersion profiles d2–d6. Here we consider PCFs with a cobweb transverse structure, because they have three design parameters—pitch, wall thickness, and core diameter—that all influence the fiber dispersion.[23] In contrast, the triangular PCF has only two design parameters, pitch and hole diameter. Using the MIT photonic-bands software,[34] we have therefore performed a full-vectorial plane-wave analysis of cobweb PCFs with different core diameters, keeping the pitch fixed at 8.5 μm and the wall thickness fixed at 130 nm. The resulting dispersion profiles are shown in Fig. 8. As seen from the phase-mismatch curves, the direct degenerate Stokes and anti-Stokes wavelengths shift closer to the pump wavelength when the core diameter is reduced. The cobweb PCF with core diameter 1450 nm has a dispersion profile (cob3) and a corresponding phase-mismatch curve, which is very similar to the case d3.

In Fig. 9, we show the SC generated in a PCF with dispersion profile d3 and cob3. As expected, the SC obtained with the cob3 profile is nearly identical to the SC obtained with the d3 dispersion profile. This allows us to conclude that the proposed method for improving the efficiency of the SC generation by a proper dispersion design can indeed be achieved in a real experiment. To provide further evidence of this, we investigate in the next section how fiber irregularities, modeled as random fluctuations of the dispersion coefficients, influence the SC generation.

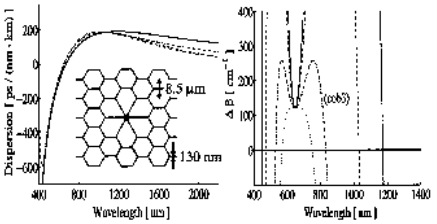

Fig. 8. Left: dispersion profiles for the cobweb PCF structures with pitch 8.5 μm, wall thickness 130 nm, and core diameter 1600 nm (solid curve), 1500 nm (dashed curve), 1450 nm (dash-dotted curve), and 1400 nm (dotted curve). Right: Corresponding phase-mismatch curves.

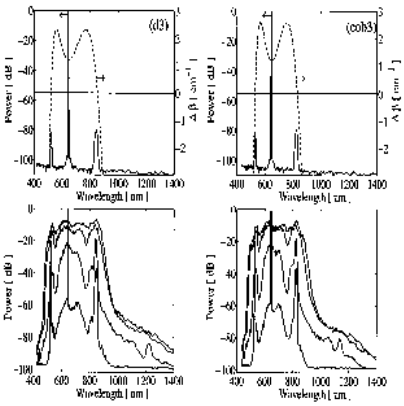

Fig. 9. Dispersion profiles d3 (left) and cob3 (right). Top row: phase mismatch $\Delta\beta$ for direct degenerate FWM (dashed curve) and spectrum at L = 10 cm (solid curve). Bottom row: spectrum at L = 20 cm, 30 cm, 1 m, 2 m, and 3.7 m (down to up).

5. ROBUSTNESS OF SUPERCONTINUUM GENERATION TO FIBER IRREGULARITIES

The SC generation process that we have considered here is mainly determined by parametric FWM, which requires phase matching. In the experiments with a PCF with dispersion profile d1,[6,7] Stokes and anti-Stokes lines due to direct degenerate FWM were generally not observed. This was explained to be due to irregularities along the PCF, leading to violation of the required phase-matching condition (3). Thus in order to conclude that parametric FWM can be used for broadband SC generation in real PCFs, we investigate the robustness of the process toward fluctuations of the dispersion coefficients along the fiber.

It has indeed been shown experimentally that a variation of the zero-dispersion wavelength λ_z of the order of 0.1 nm over the entire length of a dispersion-shifted fiber could significantly reduce the FWM efficiency.[26] This reduction in the FWM efficiency was later explained theoretically from expressions for the average parametric gain, phase-conjugation efficiency, and gain bandwidth.[27] It has also been shown that, in order to control the dispersion within ± 1 ps/(nm·km), the allowable deviation of the core radius in W-type dispersion-flattened fibers is 0.04 μm, while for other types of dispersion-flattened fibers, the allowable core radius deviation is 0.1 μm.[28] As PCFs have larger index steps and more complex structures, strong fluctuation of the fiber dispersion could be expected, too. However, to our knowledge, a thorough study of the influence of fluctuations of the PCF parameters (e.g., core size and pitch) on the variation of the dispersion profile (i.e., the dispersion coefficients β_{2-7}) is not

available. For a newly developed highly nonlinear PCF with $\lambda_z = 1.55\,\mu$m, it was recently shown that the variation of λ_z is only 6 nm, and the variation of the dispersion slope at λ_z, $D_z' = dD(\lambda_z)/d\lambda$, varies between -0.25 and -0.27 ps/(nm^2·km) over a 150-m span.[13] Expanding the propagation constant to third order around the pump wavelength $\lambda_p = 647$ nm, the dispersion has the form

$$D(\lambda) = -\frac{2\pi c}{\lambda^2}\left[\beta_2 + 2\pi c\beta_3\left(\frac{1}{\lambda} - \frac{1}{\lambda_p}\right)\right]. \tag{5}$$

From this expression, we find the dispersion coefficients

$$\beta_2 = \frac{\lambda_z^4 D_z'}{2\pi c}\left(\frac{1}{\lambda_p} - \frac{1}{\lambda_z}\right), \qquad \beta_3 = \frac{\lambda_z^4 D_z'}{4\pi^2 c^2}, \tag{6}$$

which give the extrema $\beta_2^{\max} = 7.51$ ps^2/km, $\beta_2^{\min} = 6.83$ ps^2/km, $\beta_3^{\max} = 0.44$ ps^3/km, and $\beta_3^{\min} = 0.40$ ps^3/km and thus the relative variations $\langle\beta_2\rangle = \langle\beta_3\rangle = 9.5\%$, where

$$\langle\beta_k\rangle = \frac{\beta_k^{\max} - \beta_k^{\min}}{(\beta_k^{\max} + \beta_k^{\min})/2}, \qquad k = 1,\ 2. \tag{7}$$

Note that the relative variations of β_2 and β_3 are equal.

We model the effect of a fluctuating dispersion profile by imposing that $\delta\beta$, Δ, and all the dispersion coefficients β_{z-7} [see Eq. (1)] vary randomly along the fiber,

$$\delta\beta(z) = \delta\beta + w_0(z), \qquad \beta_{k,x}(z) = \beta_k + w_{k,x}(z),$$

$$\Delta(z) = \Delta + w_1(z), \qquad \beta_{k,y}(z) = \beta_k + w_{k,y}(z),$$

where $k = 2,\ldots,7$. The random fluctuation of the coefficients, represented by the w terms, is modeled as Gaussian-distributed white noise with zero mean. To achieve the most severe case, we use different seeds for all terms. We have thus assumed that the fluctuations affect the dispersion in the two birefringent axis independently. With the results from Ref. 13 in mind, we assume that the strength (or variance) of the fluctuations is the same in all coefficients,

$$\frac{\langle w_0^2(z)\rangle}{\delta\beta} = \frac{\langle w_1^2(z)\rangle}{\Delta} = \frac{\langle w_{k,x}^2(z)\rangle}{\beta_k} = \frac{\langle w_{k,y}^2(z)\rangle}{\beta_k} = \rho, \tag{8}$$

and use the strength $\rho = 10\%$.

Random fluctuations of the whole dispersion profile will randomly vary not only the zero-dispersion wavelength λ_z, but more importantly, the phase-mismatch curve $\Delta\beta(\lambda)$, given by Eq. (3). This in turn implies that the FWM gain spectrum $g(\Delta\beta)$, given by Eq. (4), will vary randomly along the fiber, even in the undepleted pump approximation (constant peak power I_p).

In Fig. 10, we depict the fluctuation of the FWM Stokes gain band in the undepleted pump approximation over the first $L = 1$ mm of a PCF with dispersion profiles d1 ($\lambda_z = 1108$ nm) and cob3 ($\lambda_z = 800$ nm). As expected, the broader gain band of fiber cob3 is reflected in a suppression of the oscillations, as compared with the fiber d1 used in the experiments in Ref. 6. The variation of the direct degenerate FWM Stokes gain band gives an impression of the influence of the dispersion fluctuations on the effectiveness of the FWM process. The important factor is the average FWM gain over the fiber length L, defined as

$$g_{\mathrm{av}} = \frac{1}{L}\int_0^L g[\Delta\beta(z)]\,dz, \tag{9}$$

where we have indicated the z dependence of the phase mismatch as a result of the fluctuations. In Fig. 11, we show the average FWM Stokes gain calculated over the first $L = 2$ cm using the undepleted pump approximation. The reduction of the average gain for increasing strength of the fluctuations can be clearly observed. Theoretically we thus predict that, in fiber d1, realistic fluctuations would significantly suppress the Stokes and anti-Stokes lines generated from the pump by direct degenerate FWM, as also stated by Coen *et al.*[6] The corresponding simulations, presented in Fig. 12 (left), confirms

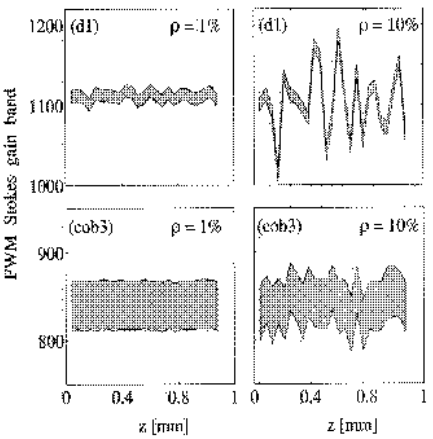

Fig. 10. Random fluctuations of the FWM Stokes gain band $g(\Delta\beta)$ (gray region), given by Eq. (4), for constant pump I_p and $\rho = 1\%$ (left) and $\rho = 10\%$ (right). The upper row is for case d1 and the bottom row for case cob3.

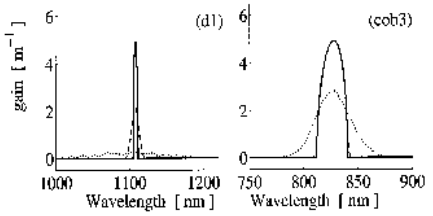

Fig. 11. Average FWM Stokes gain g_{av} over $L = 20$ cm, as given by Eq. (9) in the undepleted pump approximation. Shown is case d1 (left) and cob3 (right) for $\rho = 0$ (solid), $\rho = 1\%$ (dashed), and $\rho = 10\%$ (dotted).

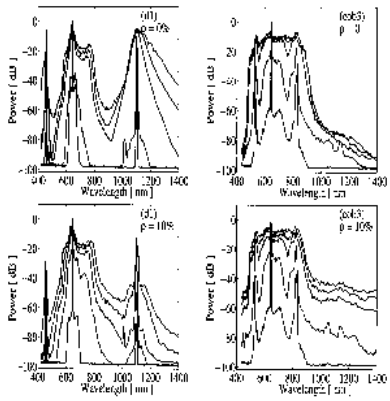

Fig. 12. Dispersion profiles d1 (left) and cob3 (right). Spectrum under influence of fluctuations with strength $\rho = 0$ (top row) and $\rho = 10\%$ (bottom row) at $L = 20$ cm, 30 cm, 1 m, 2 m, and 3.7 m (down to up).

this prediction. Using direct degenerate FWM to generate an ultrabroad SC in the particular fiber d1 is therefore not realistic.

In contrast, with our proposed cobweb fiber cob3 with a broad gain band, even fluctuations with $\rho = 10\%$ should not significantly reduce the FWM effectiveness, which is also confirmed by our simulations shown in Fig. 12 (right). In our proposed fibers d4 and d5, the FWM gain band is even broader, indicating that fluctuations will have even less effect. Thus our numerical results show that using direct degenerate FWM to generate an ultrabroad SC is a realistic option.

6. CONCLUSION

We have numerically investigated SC generation in birefringent PCFs using low-power 30-ps pulses with 400-W peak power. Our results show that by properly designing the dispersion profile and using the generation, broadening, and final merging of widely separated pump and FWM Stokes and anti-Stokes lines, the SC generation efficiency can be significantly improved, resulting in a broader SC spectrum and a reduced loss of power to frequencies outside the SC. Thus by optimizing the dispersion profile, we have generated an ultrabroad SC ranging from 450 nm to 1250 nm within the 20-dB level.

We have shown that the key issue is to make sure that the Stokes and anti-Stokes lines are generated close enough to the pump to be able to broaden and merge with the central (pump) part of the SC before nonlinear processes are suppressed due to fiber loss and temporal walk-off. We have also shown that this in turn requires the FWM gain band to be sufficiently broad, which is an essential property of our designed dispersion profiles.

We have found that the cobweb PCF structure is suitable for experimental realization of the proposed fiber dispersions leading to effective SC generation.

Finally, we have investigated the robustness of the SC generation process in our proposed PCFs toward fluctuations in the parameters along the fiber. Such fluctuation could be detrimental to the phase-sensitive FWM process, which depends on the degree of phase matching. Simulations including random fluctuations of the dispersion profile along the fiber show that the broad FWM gain band of our proposed fibers improve the robustness and that the process of efficient SC generation survives random fluctuations of a realistic strength.

ACKNOWLEDGMENTS

We acknowledge support from the Danish Center for Scientific Computing under contract CPU-1101-27. This work was supported by the Danish Technical Research Council (grant 26-00-0355) and the Graduate School in Nonlinear Science (The Danish Research Agency).

REFERENCES

1. R. R. Alfano and S. L. Shapiro, "Emission in the region 4000 to 7000 Å via four-photon coupling in glass," Phys. Rev. Lett. **24**, 584–587 (1970).
2. R. R. Alfano and S. L. Shapiro, "Observation of self-phase modulation and small-scale filaments in crystals and glasses," Phys. Rev. Lett. **24**, 592–594 (1970).
3. R. R. Alfano, ed., *The Supercontinuum Laser Source* (Springer-Verlag, New York, 1989).
4. C. Lin and R. H. Stolen, "New nanosecond continuum for excited-state spectroscopy," Appl. Phys. Lett. **28**, 216–218 (1976).
5. P. L. Baldeck and R. R. Alfano, "Intensity effects on the stimulated four photon spectra generated by picosecond pulses in optical fibers," J. Lightwave Technol. **5**, 1712–1715 (1987).
6. S. Coen, A. Chau, R. Leonardt, J. Harvey, J. C. Knight, W. J. Wadsworth, and P. S. J. Russell, "Supercontinuum generation via stimulated Raman scattering and parametric four-wave mixing in photonic crystal fibers," J. Opt. Soc. Am. B **19**, 753–764 (2002).
7. S. Coen, A. H. L. Chau, R. Leonardt, J. D. Harvey, J. C. Knight, W. J. Wadsworth, and P. S. J. Russell, "White-light supercontinuum generation with 60-ps pulse in a photonic crystal fiber," Opt. Lett. **26**, 1356–1358 (2001).
8. K. Mori, H. Takara, S. Kawanishi, and T. Morioka, "Flatly broadened supercontinuum spectrum generated in a dispersion decreasing fiber with convex dispersion profile," Electron. Lett. **33**, 1806–1808 (1997).
9. K. Mori, H. Takara, and S. Kawanishi, "Analysis and design of supercontinuum pulse generation in a single-mode optical fiber," J. Opt. Soc. Am. B **18**, 1780–1790 (2001).
10. K. Tamura, H. Kubota, and M. Nakazawa, "Fundamentals of stable continuum generation at high repetition rates," IEEE J. Quantum Electron. **36**, 773–779 (2000).
11. A. Ferrando, E. Silvestre, J. J. Miret, and P. Andres, "Nearly zero ultraflattened dispersion in photonic crystal fibers," Opt. Lett. **25**, 790–792 (2000).
12. A. Ferrando, E. Silvestre, P. Andres, J. J. Miret, and M. V. Andres, "Designing the properties of dispersion-flattened photonic crystal fibers," Opt. Express **9**, 687–697 (2001).
13. K. P. Hansen, J. R. Jensen, C. Jacobsen, H. R. Simonsen, J. Broeng, P. M. W. Skovgaard, A. Petersson, and A. Bjarklev, "Highly nonlinear photonic crystal fiber with zero-dispersion at 1.55 m," *Optical Fiber Communication Conference*, Vol. 70 of OSA Trends in Optical Technology Series (Optical Society of America, Washington, D.C., 2002), paper FA9.
14. J. K. Ranka, R. S. Windler, and A. J. Stentz, "Visible continuum generation in air–silica microstructure optical fi-

bers with anomalous dispersion at 800 nm," Opt. Lett. **25**, 25–27 (2000).
15. T. A. Birks, W. J. Wadsworth, and P. St. J. Russell, "Supercontinuum generation in tapered fibers," Opt. Lett. **25**, 1415–1417 (2000).
16. A. V. Gusakov, V. P. Kalosha, and J. Herrmann, "Ultrawide spectral broadening and pulse compression in tapered and photonic fibers," *Quantum Electronics and Laser Science*, Vol. 57 of OSA Trends in Optical Technology Series (Optical Society of America, Washington, D.C., 2001), p. 29.
17. W. J. Wadsworth, A. Ortigosa-Blanch, J. C. Knight, T. A. Birks, T. P. M. Man, and P. St. J. Russell, "Supercontinuum generation in photonic crystal fibers and optical fiber tapers: a novel light source," J. Opt. Soc. Am. B **19**, 2148–2155 (2002).
18. A. V. Husakou and J. Herrmann, "Supercontinuum generation, four-wave mixing, and fission of higher-order solitons in photonic-crystal fibers," J. Opt. Soc. Am. B **19**, 2171–2182 (2002).
19. J. Herrmann, U. Griebner, N. Zhavoronkov, A. Husakou, D. Nickel, J. C. Knight, W. J. Wadsworth, P. St. J. Russell, and G. Korn, "Experimental evidence for supercontinuum generation by fission of higher-order solitons in photonic fibers," Phys. Rev. Lett. **88**, 173901 (2002).
20. J. M. Dudley, L. Provino, N. Grossard, H. Maillotte, R. S. Windler, B. J. Eggleton, and S. Coen, "Supercontinuum generation in air–silica microstructured fibers with nanosecond and femtosecond pulse pumping," J. Opt. Soc. Am. B **19**, 765–771 (2002).
21. W. H. Reeves, J. C. Knight, and P. St. J. Russell, "Demonstration of ultra-flattened dispersion in photonic crystal fibers," Opt. Express **10**, 609–613 (2002).
22. K. P. Hansen, "Dispersion flattened hybrid-core nonlinear photonic crystal fiber," Opt. Express **11**, 1503–1509 (2003).
23. J. C. Knight, J. Arriaga, T. A. Birks, A. Ortigosa-Blanch, W. J. Wadworth, and P. St. J. Russell, "Anomalous dispersion in photonic crystal fiber," IEEE Photon. Technol. Lett. **12**, 807–809 (2000).
24. C. D. Pole, J. H. Winters, and J. A. Nagel, "Dynamical equations for polarization dispersion," Opt. Lett. **16**, 372–374 (1991).
25. P. K. A. Wai, C. R. Menyuk, and H. H. Chen, "Effects of randomly varying birefringence on soliton interactions in optical fibers," Opt. Lett. **16**, 1735–1737 (1991).
26. P. O. Hedekvist, M. Karlsson, and P. A. Andrekson, "Polarization dependence and efficiency in a fiber four-wave mixing phase conjugator with orthogonal pump waves," IEEE Photon. Technol. Lett. **8**, 776–778 (1996).
27. M. Karlsson, "Four-wave mixing in fibers with randomly varying zero-dispersion wavelength," J. Opt. Soc. Am. B **15**, 2269–2275 (1998).
28. N. Kuwaki and M. Ohashi, "Evaluation of longitudinal chromatic dispersion," J. Lightwave Technol. **8**, 1476–1481 (1990).
29. J. Garnier and F. Kh. Abdullaev, "Modulational instability by random varying coefficients for the nonlinear Schrödinger equation," Physica D **145**, 65–83 (2000).
30. R. Knapp, "Transmission of solitons through random media," Physica D **65**, 496–508 (1993).
31. K. J. Blow and D. Wood, "Theoretical description of transient stimulated Raman scattering in optical fibers," Proc. IEEE **25**, 2665–2673 (1989).
32. P. T. Dinda, G. Millot, and S. Wabnitz, "Polarization switching and suppression of stimulated Raman scattering in birefringent optical fibers," J. Opt. Soc. Am. B **15**, 1433–1441 (1998).
33. G. P. Agrawal, *Nonlinear Fiber Optics*, 2nd ed. (Academic, San Diego, Calif., 2000).
34. S. G. Johnson and J. D. Joannopoulos, "Block-iterative frequency-domain methods for Maxwell's equations in a plane-wave basis," Opt. Express **8**, 173–190 (2001).

Bibliography

[1] A. C. Newell, J. V. Moloney, *Nonlinear Optics*, (Addison-Wesley, 1991).

[2] G. P. Agrawal, *Nonlinear Fiber Optics*, (Academic Press, 2001).

[3] E. Infeld, G. Rowlands, *Nonlinear Waves Solitons Chaos*, (Cambridge University Press, 1990).

[4] A. Scott, *Nonlinear Science*, (Oxford University Press, 2003).

[5] K. B. Dysthe, H. L. Pecseli, "Non-liear langmuir wave modulation in collisionless plasmas," Plsama Phys. **19** 931-943 (1977).

[6] H. L. Pecseli, J. J. Rasmussen, "Nonlinear electron waves in strongly magnetized plasmas," Plsama Phys. **22** 421-438 (1980).

[7] K. Trulsen, and K. B. Dysthe, "A modified nonlinear Schrodinger equation for broader bandwidth gravity waves on deep water," **24** 281-289 (1996).

[8] O. Bang, J. J. Rasmussen, and P. L. Christiansen, "Subctitical localization in the discrete nonlinear Schrø" dinger equation with arbitrary power nonlinearity," Nonlinearity **7** 205-218 (1994).

[9] F. D. Dalfovo, S. Giorgini, L. P. Pitaevskii, S. Stringari, "Theory of Bose-Einstein condensation in trapped gases," Rev. Mod. Phys. **71** 463-512 (1999).

[10] C. J. Pethick, H. Smith, "Bose-Einstein condensation in dilute gases," Cambridge University Press (2002).

[11] O. Bang, W. Krolikowski, J. Wyller, and J. J. Rasmussen, "Collapse arrest and soliton stabilization in nonlocal nonlinear media," Phys. Rev. E **66** 466191-466195 (2002).

[12] D. Suter, T. Blasberg, "Stabilization of trasverse solitary waves by a nonlocal response of the nonlinear medium," Phys. Rev. A **48** 4583-4587 (1993).

[13] S. Tzortzakis, L. Berge, A. Couairon, M. Franco, B. Prade, and A. Mysyrowicz, "Breakup and fusion of self-guided femtosecond light pulses in air," Phys. Rev. Lett. **86** 5470-5473 (2001).

[14] A. Couairon and L. Bergé, "Modeling the filamentation of ultra-short pulses in ionizing media," Phys. Plasmas **7** 193-209 (2000).

[15] M. Mlejnek, E. M. Wright, J. V. Moloney, "Dynamic spatial replenishment of femtosecond pulses propagating in air," Opt. Lett. **23** 382-384 (1998).

[16] D. I. Kovsh, D. J. Hagan, and E. W. V. Stryland, "Numerical modeling of thermal refraction in liquids in the transient regime", Opt. Express **4** 315-327 (1999).

[17] P. Brochard, V. Grolier-Mazza, and R. Cabanel, "Temporal nonlinear refraction in dye solutions: a study of the transient regime", J. Opt. Soc. Am. B **14** 405-414 (1997).

[18] S. Gatz and J. Hermann, "Anisotropy, nonlocality, and space-charge field displacement in (2+1)-dimensional self-trapping in biased photorefractive crystals," Opt. Lett. **23** 1176-1178 (1998).

[19] A. A. Zozulya, D. Z. Anderson, A. V. Mamaev, amd M. Saffman,

"Solitary attractors and low-order filamentation in anisotropic self-focusing media," Phys. Rev. A **57** 522-534 (1998).

[20] W. Krolikowski, C. Denz, A. Stepken, M. Saffman, and B. Lither-Davies, "Interaction of spatial photorefractive solitons," Quantum Semiclass. Opt. **10** 823-837 (1998).

[21] P. M. Johansen, "Photorefractive space-charge field formation: linear and nonlinear effects," J. Opt. A: Pure Appl. Opt. **5** 398-415 (2003).

[22] *The physics and applications of photorefractive materials*, L. Solymar, D. J. Webb, and A. Grunnet-Jepsen ed. (Clarendon Press-Oxford, 1996).

[23] D. Suter and T. Blasberg, "Stabilization of transverse solitary waves by a nonlocal response of the nonlinear medidium," Phys. Rev. A **48** 4583-4587 (1993).

[24] Yu. B. Gaididei, S. F. Mingaleev, P. L. Christiansen, "Effect of nonlocal dispersion on self-interacting excitations," Phys. Lett. A **222** 152-156 (1996).

[25] I.C. Khoo, "Liquid crystals and nonlinear optical phenomena," (Wiley, New York, 1995).

[26] M. Peccianti, K. A. Brzdakiewicz, and G. Assanto, "Nonlocal spatial soliton interactions in nematic liquid crystals," Opt. Lett. **27** 1460-1462 (2002).

[27] G. Assanto, M. Peccianti and C. Conti, "Optical spatial solitons in nematic liquid crystals," Optics Photonics News **14**, 45-48 (2003).

[28] J. D. Joannopoulos, R. D. Meade, J. N. Winn, *Photonic Crystals: Molding the Flow of Light*, (Princeton University Press, 1991).

[29] K. Sakoda, *Optical Properties of Photonic Crystals*, (Springer-Verlag Berlin Heidelberg, 2001).

[30] T. A. Birks, J. C. Knight, and P. St. J. Russell, "Endlessly single-mode photonic crystal fiber," Opt. Lett. **22**, 961-963 (1997).

[31] J. C. Knight, T. A. Birks, P. St. J. Russell, and D. M. Atkin, "All-silica single-mode optical fiber with photonic crystal cladding," Opt. Lett. **21**, 1547-1549 (1996); **22**, 484-485 (1997).

[32] J. C. Knight, J. Broeng, T. A. Birks, and P. St. J. Russell, "Photonic band gap guidance in optical fibers," *Science* **282**, 1476-1478 (1998).

[33] J. Broeng, S. E. Barkou, T. Søndergaard, and A. Bjarklev, "Analysis of air-guiding photonic bandgap fibers," Opt. Lett. **25**, 96-98 (2000).

[34] J. C. Knight, "Photonic crystal fibers," Nature **424**, 847-851 (2003).

[35] P. Russell, "Photonic Crystal Fibers", Science **17** 358-362 (2003).

[36] *Nonlinear Photonic Crystals* R. E. Slusher, B. J. Eggeleton(eds.) (Springer-Verlag Berlin Heidelberg, 2003).

[37] M. Nakazawa *Nonlinear Guided Waves and their Applications, OSA Technical Digest* (Washington 2001) paper NLTuC1-3

[38] Snyder A. and Ladouceur F. 1999 *Optics & Photonics News* **10** 35.

[39] Kivshar Y. S. and Agrawal G. P. *Optical Solitons: From Fibers to Photonic Crystals* (Academic Press, San Diego, 2003) 560 pp.

[40] Stegeman G. I. and Segev M. 1999 *Science* **286**, 1518.

[41] Litvak A. G. *et al.* 1975 *Sov. J. Plasma Phys.* **1** 31.

[42] Litvak A. G. and Sergeev A. M. 1978 *JETP Lett.* **27** 517.

[43] Davydova T. A. and Fishchuk A. I. 1995 *Ukr. J. Phys.* **40** 487.

[44] Snyder A. and Mitchell J. 1997 *Science* **276** 1538.

[45] Snyder A. and Mitchell J. 1999 *J. Opt. Soc. Am. B* **16** 236.

[46] Suter D. and Blasberg T. 1993 *Phys. Rev. A* **48** 4583.

[47] Gordon J. P. *et al.* 1965 *J. Appl. Phys.* **36** 3.

[48] Akhmanov S. *et al.* 1968 *IEEE J. Quant. Electron.* **QE-4** 568.

[49] Gatz S. and Herrmann J. 1998 *Opt. Lett.* **23** 1176.

[50] McLaughlin D W *et al.* 1995 Physica D **88** 55; Karpierz M. 2002 *Phys. Rev. E* **66** 036603.

[51] Conti C., Peccianti M. and Assanto G. "Spatial solitons in nematic liquid crystals: a new model", in *Nonlinear Guided Waves and Their Applications*, OSA Technical Digest, pp. NLMD32:1-3. (Optical Society of America, Washington DC, 2002).

[52] W. Krolikowski and O. Bang, "Solitons in nonlocal nonlinear media: Exact solutions," Phys. Rev. E **63** 016610 (2001)

[53] Kivshar Y. S., 1993 *IEEE J. Quantum Electron.* **29** 250.

[54] Swartzlander G. A. Jr. and Law C. T. 1992 *Phys. Rev. Lett.* **69** 2503.

[55] Dreischuh A. *et al.* 1999 *Phys. Rev. E* **60** 6111.

[56] Abe S. and Ogura A. 1998 *Phys. Rev. E* **57** 6066.

[57] Benjamin T. B. and Feir J. E. 1967 *J. Fluid. Mech.* **27** 417.

[58] Hasegawa A. *Plasma Instabilities and Nonlinear Effects* (Springer-Verlag, Heidelberg, 1975).

[59] Ostrovskii L. A. 1967 *Sov. Phys. JETP* **24** 797.

[60] Bespalov V. I. and Talanov V. I. 1966 *JETP Lett.* **3** 307; Karpman V. I. 1967 *JETP Lett.* **6** 277.

[61] Kivshar Y. S. and Peyrard M. 1992 *Phys. Rev. A* **46** 3198.

[62] Potasek M. J. 1987 *Opt. Lett.* **12** 921.

[63] Kivshar Y. S., Anderson D and Lisak M 1993 *Phys. Scripta* **48** 679.

[64] Soljacic M. *et al.* 2000 *Phys. Rev. Lett.* **84** 467.

[65] Krolikowski W. *et al.* 2001 *Phys. Rev. E* **64** 016612.

[66] Wyller J. *et al.* 2003 *Phys. Rev E* **66** 066615.

[67] M. Peccianti, C. Conti, and G. Assanto, "Optical modulational instability in a nonlocal medium," *Phys. Rev. E* **68** 25602-1-4 (2003).

[68] Rasmussen J. J. and Rypdal K. 1986 *Physica Scripta* **33** 481-497.

[69] Bergé L. 1998 *Phys. Rep.* **303** 259.

[70] C. Sulem and P. L. Sulem, "The Nonlinear Schrödinger Equation, Self-Focusing and Wave Collapse," Springer Verlag 1999.

[71] Kivshar Y. S. and Pelinovsky D. E. 2000 *Phys. Rep.* **331** 117.

[72] Wong A. Y. and Cheung P. Y. 1984 *Phys. Rev. Lett.* **52** 1222.

[73] Garmire E., Chiao R. Y. and Towns C. H. 1966 *Phys. Rev. Lett.* **16** 347.

[74] Sackett C. A. *et al.* 1999 *Phys. Rev. Lett.* **82** 876.

[75] Banerjee P. P., Korpel A. and Lonngren K. E. 1983 *Phys. Fluids* **26**, 2393.

[76] Shapiro S. L. and Teukolsky S. A. *Black Holes, White Dwars, and Neutron Stars - The Physics of Compact Objects* (John Wiley & Sons, New York 1983).

[77] Houbiers M. and Stoof H. T. 1996 *Phys. Rev. A* **54** 5055.

[78] Gerton J. M. *et al.* R G 2000 *Nature* **408** 692.

[79] Donley E. A. *et al.* 2001 *Nature* **412** 295.

[80] Turitsyn S. K. 1985 *Teor. Mat. Fiz.* **64** 226.

[81] Pérez-García V. M., Konotop V. V. and García-Ripoll J J 2000 *Phys. Rev. E* **62** 4300-4308.

[82] Parola A., Salasnich L. and Reatto L. 1998 *Phys. Rev. A* **57** R3180.

[83] Anderson *Phys. Rev. A* **27** 3135 (1983).

[84] N. G. Vakhitov, A. A. Kolokolov, *Radiophys. and Quantum Electronics* **16** 783 (1975); Kolokolov A. A. 1976 *Radiophys. and Quantum Electronics* **17** 1016.

[85] Z. H. Mussliman, and J. Yang, "Transverse instability of strongly coupled dark-bright Manakov vector solitons," **26**, 1981-1983 (2001).

[86] M. Ahles, K. Motzek, A. Stepken, F. Kaiser, C. Weilnau, C. Denz, "Stabilization and breakup of coupled dipole-mode beams in an anisotropic nonlinear medium," J. Opt. Soc. Am. B **19**, 557-562 (2002).

[87] Buryak A. V. *et al.* 2002 *Phys. Reports.* **370** 63–235.

[88] Assanto G. and Stegeman G. I. 2002 *Opt. Express* **10** 388.

[89] Shadrivov I. V. and Zharov A. A. 2002, J. Opt. Soc. Am. B **19** 596.

[90] Conti C., Peccianti M. and Assanto G. 2003 *Phys. Rev. Lett.* **91** 073901.

[91] Nikolov N. I., Neshev D., Bang O., Królikowski W. Z., 2003 *Phys. Rev. E* **68** 036614.

[92] Shadrivov I. V., Zharov A. A., 2001 *ICTON* TuD5 159.

[93] Nikolov N. I., Neshev D., Królikowski W. Z., Bang O., Rasmussen J. J., and Cristiansen P. L., 2004 *Opt. Lett.* **29** 286.

[94] Królikowski W. Z., Bang O., Nikolov N. I., Neshev D., Rasmussen J. J., and Edmundson D., "Modulational instability, solitons and beam propagation in nonlocal nonlinear media" *Journal of Optics B (accepted)*..

[95] Menyuk C. R., Schiek R. and Torner L. 1994 *J. Opt. Soc. Am. B* **11** 2434; Bang O. *J. Opt. Soc. Am. B* **14** 51.

[96] Buryak A. V. and Kivshar Y. S. 1996 *Phys. Rev. Lett.* **51** R41.

[97] Hayata K. and Koshiba M. 1994 *Phys. Rev. A* **50** 675.

[98] Buryak A. V. and Kivshar Y. S. 1995 *Phys. Lett. A* **197** 407.

[99] Kivshar Y. S. and Luther-Davies B. 1998 *Phys. Rep.* **298** 81, and reference therein.

[100] Blow K. J. and Doran N. 1985 *Phys. Rev. Lett.* **107A** 55.

[101] Zhao W. and Bourkoff E. 1989 *Opt. Lett.* **14** 1371.

[102] Foursa D. and Emplit P. 1996 *Phys. Rev. Lett.* **77** 4011.

[103] Swartzlander G. *et al.* 1991 *Phys. Rev. Lett.* **66** 1583; Skinner S. R. *et al. 1991 IEEE J. Quantum Electron.* **27**, 2211; Allan G. R. *et al.* 1991 *Opt. Lett.* **16** 156.

[104] Afanasjev V. V., Chu P. L., and Malomed B. A. 1998 *Phys. Rev. A* **57** 1088.

[105] Ostrovskaya E. A., Kivshar Y. S. and Chen Z., and Segev M. 1999 *Opt. Lett.* **24** 327.

[106] Luther-Davies B. and Xiaoping Yang 1992 *Opt. Lett.* **17**, 1755.

[107] T. Morioka et al., "1 Tbit/s (100 Gbit/s X 10 channel) OTDM/WDM transmission using a single supercontinuum WDM source," Electron. Lett. **32**, 906-907 (1996).

[108] H. Takara et al., "More than 1000 channel optical frequency chain generation from single supercontinuum source with 12.5 GHz channel spacing," Electron. Lett., 36, 2089-2090, (2000).

[109] S. T. Cundiff, J. Ye, and J. L. Hall, "Optical frequency synthesis based on mode-locked lasers," Rev. Sci. Instrum., **72**, 3749-3771 (2001).

[110] K. Mori, T. Morioka, and M. Saruwatari, "Ultrawide spectral range groupvelocity dispersion measurement utilizing supercontinuum in an optical fiber pumped by a 1.5 μm compact laser source," IEEE Trans. Instrum. Meas., **44**, 712-715 (1995).

[111] Scott A. Diddams, David J. Jones, Jun Ye, Steven T. Cundiff, John L. Hall, Jinendra K. Ranka, Robert S. Windeler, Ronald Holzwarth, Thomas Udem, and T.W. H ansch, "Direct link between microwave and optical frequencies with a 300 THz femtosecond laser comb," **84**, 5102-5105 (2000).

[112] Th. Udem, S. A. Diddams, K. R. Vogel, C.W. Oates, E. A. Curtis, W. D. Lee, W. M. Itano, R. E. Drullinger, J.C. Bergquist, and L. Hollberg, "Absolute frequency measurements of the Hg^+ and Ca optical clock transitions with a femtosecond laser," Phys. Rev. Lett. **86**, 4996-4999 (2001).

[113] *The Supercontinuum Laser Source*, R. R. Alfano, ed. (Springer-Verlag, New-York, 1989).

[114] R. R. Alfano and S. L. Shapiro, "Emmision in the region 4000 to 7000Å via four-photon coupling in glass," Phys. Rev. Lett. **24**, 584-587 (1970).

[115] R. R. Alfano and S. L. Shapiro, "Observation of self-phase modulation and small-scale filaments in crystals and glasses," Phys. Rev. Lett. **24**, 592-594 (1970).

[116] C. Lin and R. H. Stolen, "New nanosecond continuum for excited-state spectroscopy," Appl. Phys. Lett. **28**, 216-218 (1976).

[117] S. Coen, A. H. L. Chau, R. Leonardt, J. D. Harvey, J. C. Knight, W. J. Wadsworth, and P. St. J. Russell, "White-light supercontinuum generation with 60-ps pulse in a photonic crystal fiber," Opt. Lett. **26**, 1356-1358 (2001).

[118] P. L. Baldeck and R. R. Alfano, "Intensity effects on the stimulated four photon spectra generated by picosecond pulses in optical fibers," IEEE J.Lightwave Technol. **5**, 1712-1715 (1987).

[119] S. Coen, A. Chao, R. Leonardt, J. Harvey, J. C. Knight, W. J. Wadsworth, and P. St. J. Russell, "Supercontinuum generation via stimulated Raman scattering and parametric four-wave-mixing in photonic crystal fibers," J. Opt. Soc. Am. B **19**, 753-764 (2002).

[120] K. Mori, H. Takara, S. Kawanishi and T. Morioka, "Flatly broadened supercontinuum spectrum generated in a dispersion decreasing fiber with convex dispersion profile," Electron. Lett. **33**, 1806-1808 (1997).

[121] K. Mori, H. Takara, and S. Kawanishi, "Analysis and design of supercontinuum pulse generation in a single-mode optical fiber," J. Opt. Soc. Am. B **18**, 1780-1792 (2001).

[122] K. Tamura, H. Kubota, and M. Nakazawa, "Fundamentals of stable continuum generation at high repetition rates," IEEE J. Quantum Electron. **36**, 773-779 (2000).

[123] A. Ferrando, E. Silvestre, J. J. Miret, and P. Andres, "Nearly zero ultraflattened dispersion in photonic crystal fibers," Opt. Lett. **25**, 790-792 (2000).

[124] A. Ferrando, E. Silvestre, P. Andres, J. J. Miret, and M. V. Andres, "Designing the properties of dispersion-flattened photonic crystal fibers," Opt. Express **9**, 687-697 (2001).

[125] K. P. Hansen, J. R. Jensen, C. Jacobsen, H. R. Simonsen, J. Broeng, P. M. W. Skovgaard, A. Petersson, A. Bjarklev, "Highly Nonlinear Photonic Crystal Fiber with Zero-Dispersion at 1.55 μm" OFC '02 Post Deadline FA 9, (2002).

[126] T. A. Birks, W. J. Wadsworth, and P. St. J. Russell, "Supercontinuum generation in tapered fibers," Opt. Lett. **25**, 1415-1417 (2000).

[127] J. K. Ranka, R. S. Windler, and A. J. Stentz, "Visible continuum generation in air-silica microstructure optical fibers with anomalous dispersion at 800 nm," Opt. Lett. **25**, 25-27 (2000).

[128] A. V. Gusakov, V. P. Kalosha, and J. Herrmann, "Ultrawide spectral broadening and pulse compression in tapered and photonic fibers," *Quantum Electronics and Laser Science*, Vol. **57** of OSA Trends in optical Technology Series (Optical Society of America, Wasington, D.C., 2001) p. 29.

[129] W. J. Wadsworth, A. Ortigosa-Blanch, J. C. Knight, T. A. Birks, T. P. M. Man, and P. St. J. Russell, "Supercontinuum generation in photonic crystal fibers and optical fiber tapers: a novel light source," J. Opt. Soc. Am. B **19**, 2148-2155 (2002).

[130] A. V. Husakou and J. Herrmann, "Supercontinuum generation, four-wave mixing, and fission of higher-order solitons in photonic-crystal fibers," J. Opt. Soc. Am. B **19**, 2171-2182 (2002).

[131] J. Herrmann, U. Griebner, N. Zhavoronkov, A. Husakou, D. Nickel, J. C. Knight, W. J. Wadsworth, P. St. J. Russell, and G. Korn, "Experimental Evidence for Supercontinuum Generation by Fission of Higher-Order Solitons in Photonic Fibers," Phys. Rev. Lett. **88**, 1739011-1739014 (2002).

[132] J.M. Dudley, L. Provino, N. Grossard, H. Maillotte, R. S. Windler, B. J. Eggleton and S. Coen, "Supercontinuum generation in air-silica microstructured fibers with nanosecond and femtosecond pulse pumping," J. Opt. Soc. Am. B **19**, 765-771 (2002).

[133] K. M. Hilligsøe, H. N. Paulsen, Jan Thøgersen, S. R. Keiding, and J. J. Larsen, "Initial steps of supercontinuum generation in photonic crystal fibers," J. Opt. Soc. Am. B **20**, 1887-1893 (2003).

[134] N. I. Nikolov, O. Bang, T. Sørensen, and A. Bjarklev, "Improving efficiency of supercontinuum generation in photonic crystal fibers by direct degenerate four-wave-mixing," J. Opt. Soc. Am. B **20**, 2329-2337 (2003).

[135] T. Sørensen, N. I. Nikolov, O. Bang, A. Bjarklev, K. G. Hougaard, K. P. Hansen, and J. J. Rasmussen, "Cob-web microstructured fibers optimized for supercontinuum generation with picosecond pulses" Nonlinear Guided Waves and Their Applications Topical Meeting WC4, March 28-31, 2004, Westin Harbour Castle, Toronto, Canada.

[136] W.H. Reeves, J.C. Knight, and P.St.J. Russell, "Demonstration of ultra-flattened dispersion in photonic crystal fibers", Opt. Express **10**, 609-613 (2002).

[137] K. P. Hansen, "Dispersion flattened hybrid-core nonlinear photonic crystal fiber", Opt. Express **11**, 1503-1509 (2003).

[138] J.C. Knight, J. Arriaga, T.A. Birks, A. Ortigosa-Blanch, W.J. Wadworth, and P.St.J. Russell, "Anomalous dispersion in photonic crystal fiber", IEEE Phot. Tech. Lett. **12**, 807-809 (2000).

[139] C.D. Pole, J.H. Winters and J.A. Nagel, "Dynamical equations for polarization dispersion," Opt. Lett. **16**, 372-374 (1991).

[140] P.K.A. Wai, C.R. Menyuk, and H. H. Chen, "Effects of randomly varying birefringence on soliton interactions in optical fibers," Opt. Lett. **16**, 1735-1737 (1991).

[141] P. O. Hedekvist, M. Karlsson, and P. A. Andrekson, "Polarization dependence and efficiency in a fiber four-wave mixing phase conjugator with orthogonal pump waves," Photonics Technol. Lett. **8**, 776-778 (1996).

[142] M. Karlsson, "Four-wave mixing in fibers with randomly varying zero-dispersion wavelength," J. Opt. Soc. Am. B **15**, 2269-2275 (1998).

[143] N. Kuwaki and M. Ohashi, "Evaluation of longitudinal chromatic dispersion," J. Lightwave Technol. **8**, 1476-1481 (1990).

[144] J. Garnier and F. Kh. Abdullaev, "Modulational instability by random varying coefficients for the nonlinear Schrödinger equation," Physica D **145**, 65-83 (2000).

[145] R. Knapp, "Transmission of solitons through random media," Physica D **85**, 496-508 (1995).

[146] K.J. Blow, and D. Wood, "Theoretical description of transient stimulated Raman scattering in optical fibers," IEEE J. Quantum Electron. **25**, 2665-2673 (1989).

[147] P. T. Dinda, G. Millot, and S. Wabnitz, "Polarization switching and suppression of stimulated Raman scattering in birefringent optical fibers," J. Opt. Soc. Am. B **15**, 1433-1441 (1998).

[148] R. H. Stolen, J. P. Gordon, and W. J. Tomlinson, H. A. Haus, "Raman responcse function of silica-core fibers," J. Opt. Soc. Am. B **6**, 1159-1166 (1989).

[149] P. L. Francois, "Nonlinear propagation of ultrashort pulses in optical fibers: total field formulation in the frequency domain," J. Opt. Soc. Am. B **8**, 276-293 (1991).

[150] S. Tzortzakis, L. Sudrie, M. Franco, B. Prade, A. Mysyrowicz, A. Couairon, and L. Berge, "Self-guided propagation of ultrashort IR laser pulses in fused silica" Phys. Rev. Lett. **87**, 2139021-2139024 (2001).

[151] Editorial "Supercontinuum generation," Appl. Phys. B **77** 143-147 (2003).

[152] G. Mejean, J. Kasparian, E. Salmon, J. Yu, J.-P. Wolf, R. Bourayou, R. Sauerbrey, M. Rodriguez, L. Woste, H. Lehmann, B. Stecklum, U. Laux, J. Eisloffel, A. Scholz, A. P. Hatzes, "Towards a supercontinuum-based infrared lidar," Appl. Phys. B **77** 357 (2003).

[153] S. Skupin, U. Peschel, C. Etrich, L. Leine, F. Lederer, and D. Michaelis, "Simulation of femtosecond pulse propagation in air," Opt. Quantum Electr. **35** 573-582 (2003).

[154] S. Tzortzakis, L. Berge, A. Couairon, M. Franco, B. Prade, and A. Mysyrowicz, "Breakup and fusion of self-guided femtosecond light pulses in air," **86** 5470-5473 (2001).

[155] A.V. Husakou, V.P. Kalosha, and J. Herrmann, "Supercontinuum generation and pulse compression in hollow waveguides," Opt. Lett. **26** 1022 (2001). ; V. P. Kalosha, J. Herrmann, "Self-phase modulation and compression of few-optical-cycle pulses," Phys. Rev. A **62** 011804 (2000).

[156] A. Baltuska, Z. Wei, M. S. Pshenichnikov, and D. A. Wiersma, "Optical pulse compression to 5 fs at a 1-MHz repetition rate," Opt. Lett. **22** 102 (1997).

[157] M. Nisoli, S. De Silvestri, O. Svelto, R. Szipcs, K. Ferencz, C. Spielmann, S. Sartania, and F. Krausz, "Compression of high-energy laser pulses below 5 fs," Opt. Lett. **22** 522 (1997).

[158] P. Antonie, A. L'Huillier, and M. Lewenstein, "Attosecond Pulse Trains Using High-Order Harmonics," Phys. Rev. Lett. **77** 1234 (1996). K. J. Schafer and K. C. Kulander, "High Harmonic Generation from Ultrafast Pump Laser," Phys. Rev. Lett. **78** 638 (1997).

[159] V. P. Kalosha and J. Herrmann, "Formation of Optical Subcycle Pulses and Full Maxwell-Bloch Solitary Waves by Coherent Propagation Effect," Phys. rev. Lett. **83** 544 (1999).

[160] V. P. Kalosha, J. Herrmann, "Phase relations, quasicontinuous spectra and subfemtosecond pulses in high-order stimulated Raman scattering with short-pulse excitation," Phys. Rev. Lett. **85** 1226-1229 (2000).

[161] G. Chang, T. B. Norris, and H. G. Winful, "Optimization of supercontinuum generation in photonic crystal fibers for pulse compression," Opt. Lett. **28** 546-548 (2003).

[162] A. F. Fercher, W. Drexler, C. K. Hitzenberger and T. Lasser, "Optical coherence tomography - principles and applications," Rep. Prog. Phys. **66** 239-303 (2003).

[163] I. Hartl, X. D. Li, C. Chudoba, R. K. Ghanta, T. H. Ko, and J. G. Fujimoto, J. K. Ranka and R. S. Windeler, "Ultrahigh-resolution optical coherence tomography using continuum generation in an air-silica microstructure optical fiber," Opt. Lett. **26** 608-610 (2001).

[164] B. Povazay, K. Bizheva, A. Unterhuber, B. Hermann, H. Sattmann, A. F. Fercher, and W. Drexler, A. Apolonski, W. J. Wadsworth, J. C. Knight, and P. St. J. Russell, M. Vetterlein and E. Scherzer, "Submicrometer axial resolution optical coherence tomography," Opt. Lett. **27** 1800-1802 (2002).

[165] A. Mussot, L. Provino, T. Sylvestre, H. Mailotte, "Single-mode supercontinuum generation in a standard dispersion-shifted fiber using a nanosecond microchip laser," NLGW (2002).

[166] M. Tsang, D. Psaltis, F. G. Omenetto, "," Opt.. Lett. **28**, 1873-1875 (2003).